# Green syntheses of Silicalite-1 using hydroxyl free radicals and cellulose nanocrystals

Li LYU

Student ID:20615487

Department of Chemical and Environmental Engineering

University of Nottingham Ningbo China

Submitted June 2024, in partial fulfilment of

the conditions of the award of the degree MRes. in

Chemical Engineering and Technology

I hereby declare that this dissertation is all my own work,

except as indicated in the text:

Signature: _____

Date: _____/_____/____

# Abstract

Zeolites play a crucial role in the various fields, but their synthesis rely on expensive organic templates and the subsequent removal of these templates through calcination generates environmentally detrimental gases. Therefore, research efforts are needed to enhance the efficiency and cost-effectiveness of zeolites synthesis.

As hydroxyl free radicals (•OH) are able to accelerate the crystallisation process of zeolites and cellulose nanocrystals (CNCs) can be green templates for zeolites syntheses, this dissertation developed a novel method for Silicalite-1 zeolites synthesis with less organic template usage through the incorporation of •OH generated by sodium persulfate (SPS) and CNCs. The effects of the organic template usage, •OH and CNCs on the yield, crystalline structure, pore structure and morphology of the produced Silicalite-1 zeolites were investigated. The presence of •OH could increase the yield of Silicalite-1 zeolites but reduce the specific surface area significantly, and the presence of CNCs was able to mitigate the loss of specific surface area. It was found that the presence of •OH and CNCs promoted the synthesis of Silicalite-1 with only 50% usage of the organic template, achieving higher Silicaclite-1 yield of 74% and higher relative crystallinity of 85% compared to the conventional Silicalite-1 synthesis with 100% usage of the organic template (the yield was 44% and the relative crystallinity was 72%). In addition, the optimal surface area of using 50% TPAOH with the synergy effect of •OH and CNCs was higher than the case that synthesized with 100% TPAOH (460 $m^2/g$ *vs.* 401$m^2/g$). Si-O-Si bond-breaking and bond-remaking were identified in the Silicalite-1 synthesis process and no significant difference was observed in the absence and presence of •OH and CNCs. The developed Silicalite-1 zeolites were used as the supports for making Ni supported catalysts for carbon dioxide ($CO_2$) hydrogenation to methane ($CH_4$). And comparable $CO_2$ conversion (i.e., 80% *vs*. 82%) were achieved for both catalysts (supported with Silicalite-1 zeolites synthesised using 50% of the organic template in the presence of •OH and CNCs and synthesised using 100% of the organic template in the absence of •OH and CNCs, respectively).

**Keywords**: Silicalite-1 synthesis; hydroxyl free radicals; cellulose nanocrystals; $CO_2$ hydrogenation; methanation

# Acknowledgements

I would like to express my deepest gratitude to my supervisors, Prof. Xiaolei Fan and Dr. Xiaoxia Ou, whose invaluable guidance has steered me throughout my MRes studies. During my research, they have provided patient guidance and valuable suggestions from the design of the technical route to the analysis of the experimental outcomes.

Moreover, I wish to thank all my colleagues and friends, including Jintao Zhu, Jiaqi Yang, Cong Li, Rui Hu, Run Pan for their assistance. In addition, I would also like to express my gratitude to the China Beacon Institute. Lastly, I am deeply grateful for the unwavering support of my parents. Without their constant encouragement, I would not have been able to make significant strides and overcome various challenges in successfully completing my studies.

# Table of Contents

Abstract ..... I

Acknowledgements ..... III

Table of Contents ..... IV

List of Figures ..... VII

List of Tables ..... VII

1. Introduction ..... 1

1.1 Introduction of zeolites ..... 1

1.1 Research objectives ..... 6

2. Literature review ..... 9

2.1 Synthesis methods for zeolites ..... 9

2.1.1 Solvothermal method ..... 10

2.1.2 Solvent-free method ..... 14

2.2 Green strategies for zeolites synthesis ..... 16

2.2.1 Zeolites synthesis with sustainable materials ..... 16

2.2.2 Zeolites synthesis with less organic templates ..... 19

2.2.3 Zeolites synthesis with •OH ..... 20

2.3 Catalytic hydrogenation of $CO_2$ by zeolites ..... 24

2.3.1 $CO_2$ hydrogenation to valuable products ..... 24

2.3.2 Zeolites for direct $CO_2$ hydrogenation to $CH_4$ ..... 27

3. Experimental ..... 33

3.1 Materials and reagents ..... 33

3.2 Synthesis of Silicalite-1 materials .....33

3.2.1 Synthesis of Sililcalite-1 via conventional route .....33

3.2.2 Syntheses of Silicalite-1 in the presence of •OH .....34

3.2.2 Synthesis of Silicalite-1 in the presence of •OH and CNCs .....34

3.2.3 Synthesis of Ni/Silicalite-1 catalysts .....35

3.3 Characterisations .....36

3.3.1 X-ray Diffraction (XRD) .....36

3.3.2 $N_2$ adsorption-desorption .....36

3.3.3 Scanning Electron Microscope (SEM) .....37

3.3.4 Transmission Electron Microscopy (TEM) .....38

3.3.5 Inductively Coupled Plasma Optical Emission Spectrometry (ICP-OES) .....38

3.4 Mechanism study .....39

3.5 Catalytic tests .....41

4. Results and discussions .....44

4.1 Effect of TPAOH usage on conventional Silicalite-1 synthesis .....44

4.2 Effect of •OH on Silicalite-1 synthesis .....47

4.3 Effect of CNCs and •OH on Silicalite-1 synthesis .....51

4.3.1 100% TPAOH .....51

4.3.2 75% TPAOH .....54

4.3.3 50% TPAOH .....57

5. Mechanism study for Silicalite-1 synthesis .....69

6. $CO_2$ hydrogenation to $CH_4$ over Ni/Silicalite-1 catalysts .....74

6.1 Structural and morphological properties ..... 74

6.2 Catalytic performance ..... 76

7. Conclusion and future work ..... 78

References ..... 80

Appendix ..... 89

# List of Figures

Figure 1.1 Classification of porous materials by IUPAC [4].....1

Figure 1.2 Primary and secondary building units of zeolites.....2

Figure 1.3 SBU in zeolite framework structure and their symbols [2]. .....3

Figure 1.4 The 255 zeolites topologies currently included [8].....4

Figure 1.5 Application of zeolites in many fields [17].....5

Figure 2.1 General solvothermal methods for zeolite synthesis [34].....10

Figure 2.2 Steps in zeolite synthesis. .....12

Figure 2.3 Microwave methods for synthesis of zeolites [34]. .....13

Figure 2.4 Schematic diagram of DGC synthesis method. A: VPT method, B: SAC method [45]. .....15

Figure 2.5 Solvent-free synthesis of zeolites [21].....16

Figure 2.6 The basic structural formula of a cellulose chain. .....18

Figure 2.7 Methods to generate of •OH. .....22

Figure 2.8 The structures of zeolites and their corresponding preferences for products [83]. .....27

Figure 2.9 Illustration of metals and zeolites employed for hydrogenation of $CO_2$ to selectively product [88].....27

Figure 2.10 Potential routes for the reaction of $CO_2$ hydrogenation to $CH_4$ [89]...28

Figure 3.1 The image of XRD (Bruker D8 advance).....36

Figure 3.2 $N_2$ adsorption-desorption equipment and degas equipment (3 Flex). .37

Figure 3.3 The image of SEM-EDS equipment (Gemini SEM 360). .....38

Figure 3.4 The image of ICP-OES equipment (SPECTROBLUE). .....39

Figure 3.5 The image of FT-IR (BRUKER INVENIO S). .....40

Figure 3.6 The image of TGA equipment and the loading position for samples (SDTQ600). .....41

Figure 3.7 The fixed-bed reactor for catalytic tests. .....42

Figure 3.8 The image of GC equipment (FULI INSTRUMENTS GC9720PLUS). .....43

Figure 4.1 (a) XRD patterns and (b) yield and relative crystallinity of the products synthesised with different usage of TPAOH (The error of yield and crystallinity was 5.6% and 3.5%).....45

Figure 4.2 SEM images of (a) 100%S1-0M-0;(b) 75%S1-0M-0;(c) 50%S1-0M-0. .....46

Figure 4.3 (a) $N_2$ adsorption-desorption isotherms and (b) micropore size distributions of the solid products synthesised with different usage of TPAOH. .....46

Figure 4.4 (a) XRD patterns and (b) yield and relative crystallinity of the solid products synthesised in the absence and presence of •OH with different usage of TPAOH (The error of yield and crystallinity was 5.6% and 3.5%).....49

Figure 4.5 (a) $N_2$ adsorption-desorption isotherms and (b) micropore size distributions of the solid products synthesised in the absence and presence of •OH with different usage of TPAOH. .....50

Figure 4.6 (a) XRD patterns and (b) yield and relative crystallinity of Silicalite-1 synthesised in the absence and presence of CNCs and •OH when100% TPAOH was present (The errors of yield and relative crystallinity were 5.6% and 3.5%). .....52

Figure 4.7 $N_2$ adsorption-desorption isotherms of the solid product with the presence of CNCs and •OH when 100% TPAOH was present. .....53

Figure 4.8 (a) XRD patterns and (b) yields and crystallinities of the solid products synthesised with the presence of •OH and CNCs when 75% TPAOH was present (The errors of the yields and crystallinities were 5.6% and 3.5%). ..55

Figure 4.9 (a) $N_2$ adsorption-desorption isotherms and (b) micropore size distributions of the solid products synthesised with the presence of •OH and CNCs when 75%TPAOH was present. .....56

Figure 4.10 (a) XRD patterns and (b) yields and crystallinities of the solid products synthesised with the presence of CNCs when no •OH was present (The errors of the yields and crystallinities were 5.6% and 3.5%). ..... 59

Figure 4.11 (a) $N_2$ adsorption-desorption isotherms and (b) micropore size distributions of the solid products synthesised with the presence of CNCs when no •OH was present. ..... 59

Figure 4.12 (a) XRD patterns and (b) yield and relative crystallinity of the solid products synthesised with the presence of 0.01 M SPS and CNCs when 50% TPAOH was present. (The errors of yield and relative crystallinity were 5.6% and 3.5%). ..... 61

Figure 4.13 (a) $N_2$ adsorption-desorption isotherms and (b) micropore size distributions of the solid products synthesised with the presence of 0.01 M SPS and CNCs when 50% TPAOH was present. ..... 62

Figure 4.14 (a) XRD patterns and (b) yields and crystallinities of the solid products synthesised with the presence of 0.02 M SPS and CNCs when 50% TPAOH was present (The errors of the yields and crystallinities were 5.6% and 3.5%). ..... 64

Figure 4.15 (a) $N_2$ adsorption-desorption isotherms and (b) micropore size distributions of the solid products synthesised with the presence of 0.02 M SPS and CNCs when 50% TPAOH was present. ..... 65

Figure 4.16 SEM images of (a) 50%S1-0M-0;(b) 50%S1-0M-0.825;(c) 50%S1-0.02M-0;(d) 50%S1-0.02M-0.825. ..... 67

Figure 4.17 TEM images of (a) 50%S1-0M-0;(b) 50%S1-0M-0.825;(c) 50%S1-0.02M-0;(d) 50%S1-0.02M-0.825. ..... 68

Figure 5.1 FT-IR spectra for synthesised products with different crystallisation time. ..... 70

Figure 5.2 (a) TG and (b) DTG curves of Silicalite-1 gels with different crystallisation time. ..... 72

Figure 5.3 Synthesis route for Silicalite-1 with the presence of CNCs and •OH. 73

Figure 6.1 XRD patterns of the Silicalite-1 supports and prepared catalysts. ..... 75

Figure 6.2 $N_2$ adsorption–desorption isotherms of (a) Silicalite-1supports and (b) as-prepared catalysts. ..... 75

Figure 6.3 Catalytic tests over the catalyst for $CO_2$ conversion and $CH_4$ selectivity. ..... 77

## List of Tables

Table 2.1 Summary of Ni-based catalyst with various supports. ..... 32

Table 3.1 Materials and chemical reagents used in this experiment. ..... 33

Table 3.2 Table of Silicalite-1 zeolites. ..... 35

Table 4.1 Textural properties of Silicalite-1 synthesised with different usage of TPAOH. ..... 47

Table 4.2 Textural properties of Silicalite-1 synthesised with different usage of TPAOH. ..... 51

Table 4.3 Textural properties of Silicalite-1 synthesised when 100% TPAOH was present. ..... 54

Table 4.4 Textural properties of Silicalite-1 synthesised with the presence of •OH and CNCs when 75%TPAOH was present. ..... 57

Table 4.5 Textural properties of Silicalite-1 synthesised under 50%TPAOH with the presence of CNCs. ..... 60

Table 4.6 Textural properties of Silicalite-1 synthesised with the presence of 0.01 M SPS and CNCs when 50% TPAOH was present.. ..... 63

Table 4.7 Textural properties of Silicalite-1 synthesised with the presence of 0.02 M SPS and CNCs when 50% TPAOH was present. ..... 66

Table 6.1 Textural properties of Silicalite-1 supports and Ni/Silicalite-1 catalysts. ..... 75

# List of Abbreviations

| | |
|---|---|
| •OH | hydroxyl free radicals |
| CNCs | cellulose nanocrystals |
| SPS | sodium persulfate |
| TPAOH | tetrapropylammonium hydroxide |
| TEOS | tetraethyl orthosilicate |
| MOFs | metal organic frameworks |
| COFs | covalent organic framework |
| PBUs | Primary Build Units |
| SBUs | Secondary Building Units |
| S-1 | Silicalite-1 |
| $H_2$ | hydrogen |
| $CH_4$ | methane |
| SDA | organic structure-directing agent |
| $CO_2$ | carbon dioxide |
| DGC | dry gel conversion |
| VPT | vapor-phase transport |
| SAC | steam-assisted conversion |
| CMC | carboxymethyl cellulose |
| HDPE | high-Density Polyethylene (HDPE) |
| PP | Polypropylene |
| MCC | microcrystal cellulose |
| MTP | methanol-to-propylene |
| WHSV | weight hourly space velocities |
| SAR | $SiO_2/Al_2O_3$ ratio |
| CCS | carbon capture and storage |
| CCU | carbon capture and utilisation |
| NG | natural gas |
| DME | dimethyl ether |
| SEM | scanning electron microscopy |
| TEM | transmission electron microscopy |

| | |
|---|---|
| XRD | X-ray diffraction |
| FT-IR | Fourier-transform infrared spectroscopy |
| ICP-OES | Inductively Coupled Plasma Optical Emission Spectrometry |
| TCD | Thermal Conductivity Detector |
| FID | Flame Ionization Detector |

# 1. Introduction

## 1.1 Introduction of zeolites

Porous materials have attracted much attention in various fields owing to their regular pore structures, large specific surface areas and diverse versatility (regarding functionalities and applications). The International Union of Pure and Applied Chemistry (IUPAC) has classified porous materials into three categories based on pore size [1] (Figure 1.1): materials with pore sizes less than 2 nm are referred to as microporous materials, with zeolites and Metal Organic Frameworks (MOFs) being the most representative examples in this category. Materials with pore sizes of 2-50 nm are called mesoporous materials, and materials with pore sizes bigger than 50 nm are known as macroporous materials [2]. The performance of porous materials in a particular application is directly influenced by the distribution of void spaces in terms of sizes, shapes, and volumes [3].

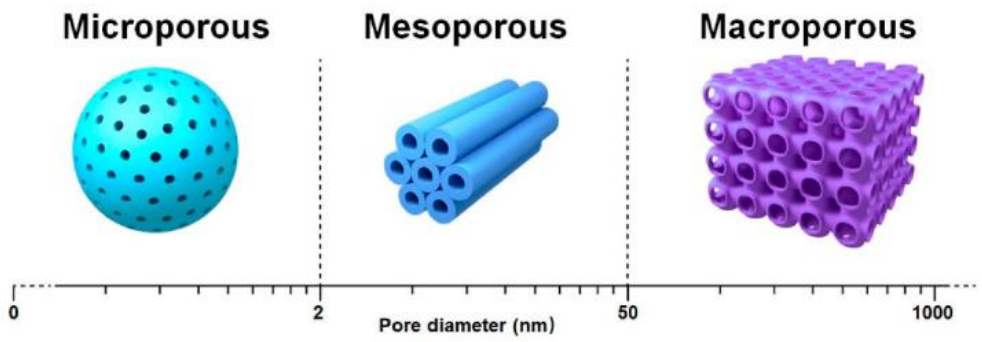


Figure 1.1 Classification of porous materials by IUPAC [4].

So far, a wide range of porous materials such as zeolites, ordered mesoporous materials, MOFs, covalent organic framework (COFs) and polymers of intrinsic microporosity (PIMs) have found extensive applications in various fields such as catalysis, adsorption, separation, purification, and energy storage. Among them, zeolites are among the most extensively investigated and topical of inorganic materials.

Zeolites are highly crystalline aluminosilicates with complex three-dimensionally extended framework structures. These frameworks are typically constructed by corner-sharing of $TO_4$ (T = Si, Al, P) tetrahedra [5]. These tetrahedra form the fundamental building blocks in the framework of zeolite, referred to as the Primary Build Units (PBUs, as indicated in the left side of Figure 1.2). However, in the connection between PBUs, Lowenstein's rule is imperative: two Al atoms in tetrahedral positions cannot be adjacent [6].

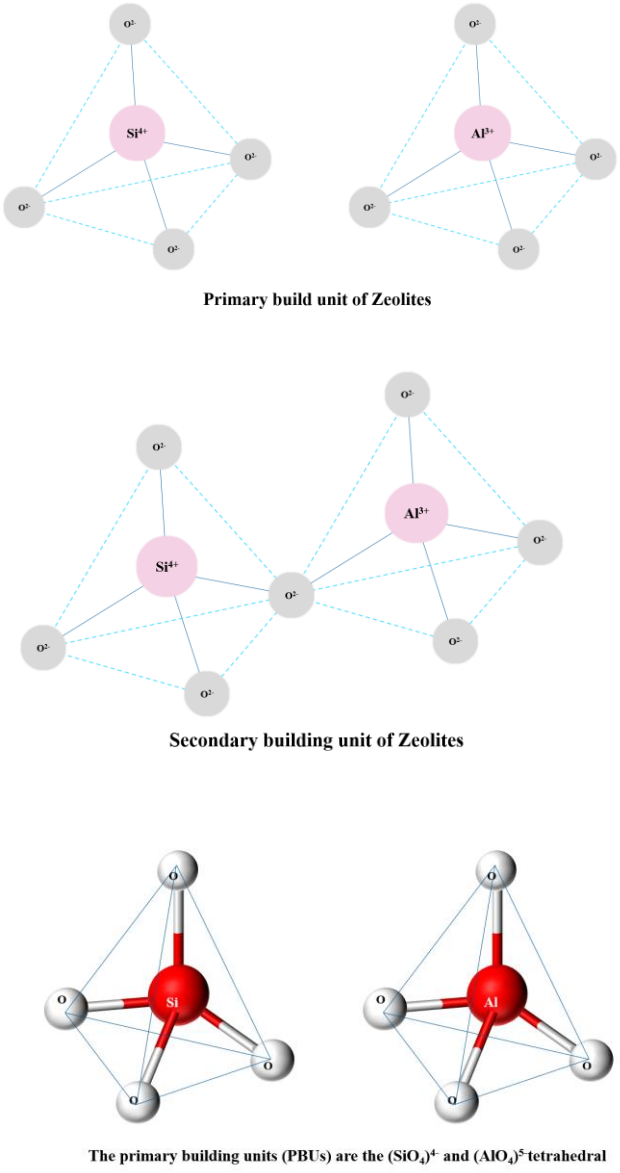


Figure 1.2 Primary and secondary building units of zeolites.

These tetrahedra can also form Secondary Building Units (SBUs, as shown in Figure 1.2) through the interlinkage of oxygen atoms to generate rings, prisms, and various sizes [7]. The commonly observed ring structures encompass four-membered, five-membered and six-membered rings, as well as double four-membered and double six-membered rings. Currently, a total of 18 distinct types of SBUs have been identified (Figure 1.3) [7].

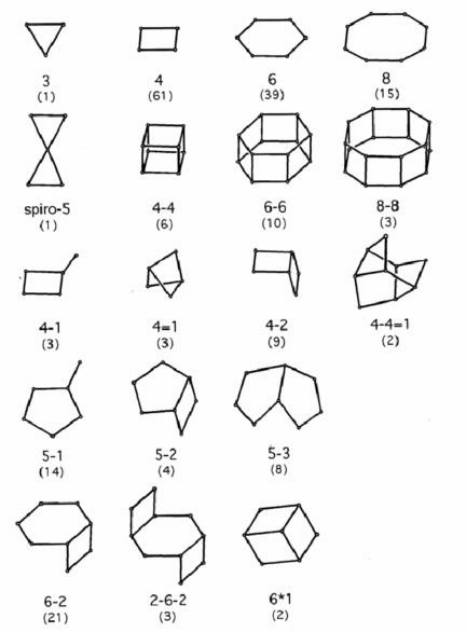


Figure 1.3 SBU in zeolite framework structure and their symbols [2].

Furthermore, these tetrahedra can also be interconnected in various manners to form zeolites with different topologies. Currently, the International Zeolite Association (IZA) has identified over 250 distinct zeolite framework types, each designated by a three-letter code [8].


Figure 1.4 The 255 zeolites topologies currently included [8].

Porous zeolites have made significant contributions to society so far, which play a crucial role in traditional domains such as adsorption, separation and catalysis due to their regular and abundant pore structure, diverse element composition of the framework, tuneable acidity and high thermal/hydrothermal stability [9-11]. The utilisation of zeolites as catalysts began in the 1960s, when they were initially utilized as solid acid catalysts in the procedure of breaking down and refining raw petroleum to produce fuels for transportation [12]. Subsequently, value-added chemicals can be produced through the use of shape-selective catalysis [13]. The invention of the initial titanosilicate (TS-1) broadened the scope of application in selective oxidation [14,15]. The subsequent applications of zeolites include their utilisation in mitigating environmental pollution, including the reduction of $NO_x$ through selective catalytic reaction and the elimination of organic sulfuric compounds via catalysts [15]. At the same time, zeolites have been employed as catalysts in fuel production, including hydrogen ($H_2$) and $CH_4$ [16]. Moreover, they exhibit significant contribution in emerging areas including carbon dioxide conversion, oil-water separation, energy storage, nuclear waste treatment and biomass conversion [17]. (As shown in Figure 1.5)


Figure 1.5 Application of zeolites in many fields [17].

In spite of the various benefits and valuable contributions to chemical processes, zeolites also have limitations. The preparation of zeolites mostly needs to be carried out under strong alkali conditions, alongside high temperatures and prolonged crystallisation periods, resulting in substantial energy consumption [18]. The utilisation of expensive organic templates, which guide the assembly pathway and ultimately occupy the pore space, is another crucial factor that demands significant attention. Which not only escalates the expense of zeolite but also leads to the generation of hazardous ($NO_x$) as well as greenhouse gases ($CO_2$) during the high-temperature combustion process employed for removing these organic templates [19]. Additionally, the associated energy released, in combination with the formed water ($H_2O$), can cause damage to the inorganic structure of zeolites [20].

Moreover, the mass production of zeolite catalysts also give rise to significant environmental challenges due to the release of wastewater during hydrothermal synthesis [21]. This contradicts the concept of green chemistry, which aims to mitigate adverse environmental impacts, minimize waste emissions and enhance efficiency in chemical manufacturing [22]. Therefore, due to the gradual increase in the demand for

zeolite in both the chemical industry and daily life, there is a pressing need to explore rapid and environmentally friendly approaches for synthesising zeolites, making it an ongoing focal point of scientific research and practical production applications within this field.

## 1.1 Research objectives

To alleviate the aforementioned limitations of conventional methods for zeolite synthesis, such as prolonged reaction time, alternative approaches have been proposed and explored to enable zeolite synthesis in an environmentally friendly, rapid and sustainable manner. These are exemplified by microwave-assisted synthesis, seeded synthesis, template-free synthesis (e.g., without organic structure-directing agent, SDA) and solvent-free synthesis [23]. Additionally, the introduction of •OH into the crystallisation process has been confirmed to significantly enhancing the rate of crystallisation and consequently reduce the synthesis time. Simultaneously, the presence of •OH in the crystallisation process can effectively reduce the reaction temperature [24]. Such discovery paves the way for more advanced and environmentally friendly approaches to synthesising zeolites.

Moreover, due to the cost, safety and environmental issues associated with the utilisation of organic templates, many researchers have directed their attention towards employing inexpensive materials/templates for zeolite synthesis as well. For example, using multi-organic amines, sugar cane biomass, sucrose and cellulose [25-28]. Among them, cellulose has gained significant attention for its potential applications in the fields of energy, chemicals, and materials, which is the most abundant inedible biomass in nature. In specific, nanosized cellulose has high aspect ratios (length *vs.* diameter), and abundant surface hydroxyl groups, is expected to be compatible with the conventional zeolite synthesis system, being the potential primary or secondary template for preparing zeolites with different porous structured.

Inspired by the previous research efforts, this project aims to develop an efficient

synthesis strategy for synthesising Silicalite-1 zeolite. The proposed approach involves the introduction of •OH for accelerating the cleavage and reformation of Si-O-Si bonds, thereby facilitating the crystallisation process. Simultaneously, cellulose will be employed as the hard template to modulate the porous structure of Silicalite-1 zeolite in the hydrothermal method. In addition, the developed zeolites were used as the carrier to prepare $CH_4$ synthesis catalysts to be applied in carbon dioxide ($CO_2$) hydrogenation for $CH_4$ synthesis, as the demonstration of the potential application, which is of great significance for valorisation of the carbon emissions. The specific objectives of this project are detailed as below:

**1.** Synthesis of Silicalite-1 zeolites using the proposed method. Parametric studies will be carried out by systematically varying key process parameters such as (i) crystallisation time, (ii) amount of Tetrapropylammonium hydroxide (TPAOH), •OH and CNCs, (iii) ratios between them.

**2.** Characterisation of the prepared zeolitic materials. The physical and chemical properties of the obtained materials will be characterized using various techniques, including (i) morphology by emission scanning electron microscopy (SEM); (ii) porosity by transmission electron microscopy (TEM); (iii) crystallinity by X-ray diffraction (XRD); (iv) porosity nitrogen ($N_2$) adsorption-desorption analysis; and (v) structural information by Fourier-transform infrared spectroscopy (FT-IR).

**3.** Establishment of the synthesis-property correlation. Information/data from (1) and (2) will be systematically investigated to establish the relevant synthesis-property relationships, which can be used for further optimization of the synthesis conditions for controlling the quality of the resulting zeolitic materials.

**4.** Catalyst preparation and catalysis. The selected zeolites will be used as the catalyst carriers for making supported Ni catalysts via impregnation. The resulting catalysts will be characterized using relevant techniques and assessed

in a packed bed catalytic reactor for their activity in $CO_2$ hydrogenation for $CH_4$ synthesis.

# 2. Literature review

The concept of zeolites was proposed by McBain in 1932 [29]. As a member of the family of inorganic porous materials, zeolites are solid materials with nanoscale pores or cavities that enable selective molecules separation based on their pore sizes. Zeolites are highly crystalline silicates with well-defined pores, tuneable acidities (i.e., concentration and strength), as well as high thermal and hydrothermal stabilities. Owing to these remarkable attributes, they have found extensive applications in the fields of catalysis (i.e., catalytic cracking, alkylation, and isomerization), separation, ion-exchange, gas storage and sensing [30].

## 2.1 Synthesis methods for zeolites

Zeolites are commonly divided into two categories: natural zeolites and synthetic zeolites [31]. The main sources of natural zeolites are volcanic and sedimentary rocks like chabazite and mordenite. Conversely, synthetic zeolites are synthesised by calcining materials such as China clay, feldspar, soda ash, and other sources [32].

The formation process of natural zeolite takes from a few days to decades, whereas synthetic zeolites can be synthesised in the laboratory within a timeframe ranging from several hours to a few days. The laboratory synthesis of zeolites provides the benefits of controllable pore size and surface properties for the zeolites, while also exhibiting exceptional thermal stability. Up to now, different approaches have been employed for the development of zeolites, including solvothermal synthesis, fluoride synthesis, dry gel conversion synthesis, ionic thermal synthesis, microwave-assisted synthesis, co-template synthesis, green synthesis and other approaches [20].The subsequent subsections delineate distinct synthetic pathways for zeolites production using diverse raw materials.

### 2.1.1 Solvothermal method

Solvothermal synthesis method refers to the utilisation of a solvent for zeolites synthesis, and the solvent used in this method can be nonpolar or hydrophobic. Till now, water has played a crucial role as the primary solvent, leading to a unique term "hydrothermal" to describe its application in zeolites synthesis. Ionothermal is designated when employing ionic solvents, also known as ionic liquids. Therefore, hydrothermal and ionothermal methods can be classified as subcategories of solvothermal method [33]. Nevertheless, the key difference is that solvents maintain their molecular structures throughout both solvothermal and hydrothermal synthesis methods, while solvents adopt their ionic states during ionothermal synthesis. The hydrothermal, solvothermal, and ionothermal methods share similarities except for utilizing different solvents. A general schematic illustration of solvothermal processes is depicted in Figure 2.1 [34].

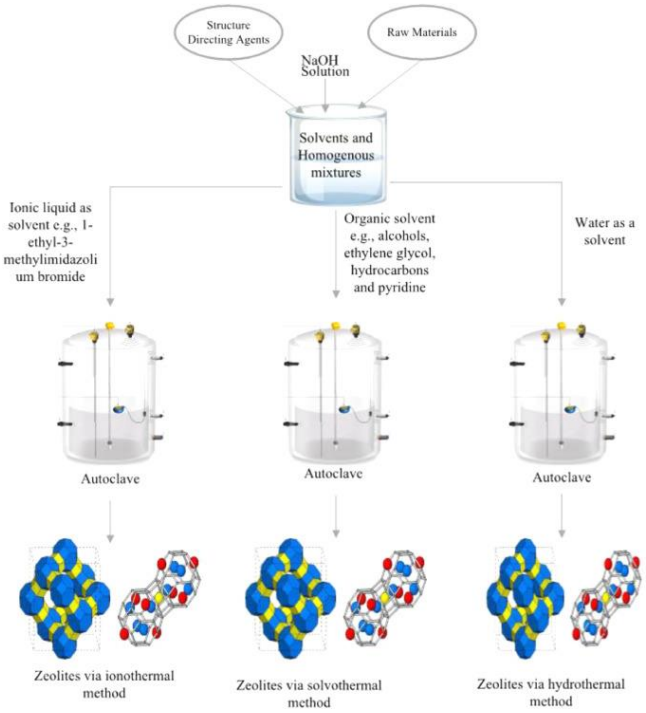


Figure 2.1 General solvothermal methods for zeolite synthesis [34].

In 1985, the pioneering work by Bibby et al. demonstrated the achievement of synthesising of SOD zeolites. This remarkable accomplishment was accomplished by employing glycol or propyl alcohol as solvents, without the addition of water, and

utilizing tripropylamine as a directing agent for structure formation [35]. This type of zeolite is difficult to be synthesised under conventional hydrothermal conditions. Subsequently, the solvothermal synthesis method was further developed. Huo et al. employed ethylene glycol, butanol and glycerol as solvents to synthesise Silicalite-1 (MFI), ZSM-39 (MTN) and ZSM-48 (*MRE) respectively [36]. However, the extensive reliance on organic solvents in the solvothermal synthesis method significantly restricts the industrial application of zeolites due to the safety risks associated with high autogenous pressures and potential toxicity resulting from large-scale usage of organic solvents. Despite the success achieved in certain aspects, the utilisation of various organic solvents in this method remains problematic due to their negative impact on the environment and their high energy and time requirements.

#### 2.1.1.1 Hydrothermal method

Notably, the majority of zeolites are typically synthesised via hydrothermal methods from silicate or aluminosilicate gel in alkaline media at temperatures ranging from around 60 to 200℃ for 1-20 days [20,37]. The groundbreaking synthesis method of zeolites was discovered by Union Carbide in the 1950s, thereby pioneering a new realm of technological advancements.

The hydrothermal synthesis method of zeolites consists of two stages: (i) the aging stage, wherein the mixture dissolves in water to form an aluminosilicate gel, and (ii) the crystallisation stage. The crystallisation stage also consists of three steps: (i) polymerisation, involving the condensation of poly-silicate and aluminate anions to generate an amorphous gel through the formation of Si,Al-O-Si,Al bonds; (ii) depolymerisation, where the amorphous gel dissolves to form aluminosilicates and silicates that are soluble via breaking Si,Al-O-Si,Al bonds; (iii) repolymerisation, where the Si,Al-O-Si,Al bonds surrounding the hydrated cation species are remade, commonly referred as structure directing agent. The nucleation and crystal growth stage of the are encompassed by crystallisation steps [24]. In short, the synthesis processes are shown in

Figure 2.2.

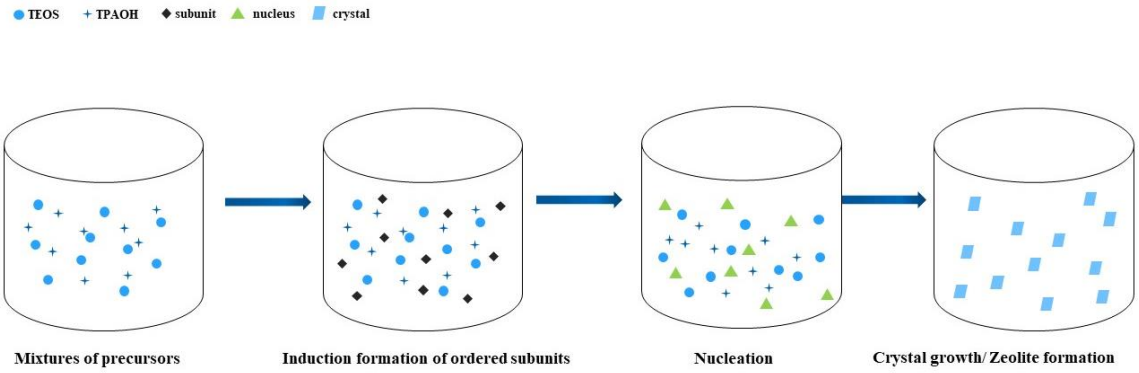


Figure 2.2 Steps in zeolite synthesis.

Although the hydrothermal synthesis of zeolites is a convenient one-step process, it poses significant environmental concerns due to its low yield of zeolite products, high energy consumption during calcination, and subsequent pollution. Additionally, the hydrothermal method relies on organic templates that are ultimately removed through high-temperature calcination or extraction with an organic solvent [37]. Therefore, alternative synthesis approaches are desirable to overcome these challenges.

### 2.1.1.2 Ionothermal method

Ionic liquids are non-molecular compounds primarily consisting of ions, characterised by their relatively low melting points (below 100°C) [38]. Therefore, ionic liquids possess the ability to simultaneously function as a solvent and a potential template or structure directing agent during the formation of solids. As an emerging synthesis method, the utilisation of ionic thermal synthesis has gained significant popularity in the formation of functional materials, including zeolites, MOFs and other inorganic/organic hybrid materials. In 2004, Cooper and colleagues made a noteworthy advancement in this field by successfully synthesising zeolites using an ionic thermal system. By employing the ionizing liquid of imidazole compounds (e.g. 1-ethyl-3-

methylimidazolium bromide, [EMIm]Br) as both the solvent and the template, zeolites structures (SIZ-n) with diverse phosphorus and aluminium compositions, as well as metallic phosphorus and aluminium frameworks, were successfully synthesised [39]. The ionic thermal synthesis system opens up a new pathway for zeolites synthesis.

### 2.1.1.3 Microwave-assisted method

The energy transfer of microwave radiation occurs due to the interaction between dielectric molecules, positioning it within the electromagnetic spectrum between infrared and radio waves. In contrast to the traditional hydrothermal method, microwave radiation is generated through intermolecular movement and friction, subsequently transforming into uniformly distributed heat energy [40]. Microwave-assisted synthesis of zeolites is commonly employed in conjunction with other methodologies, such as solvothermal, hydrothermal and ionothermal methods. Microwave-assisted synthesis method can shorten the crystallisation time, accelerate nucleation, obtain products with uniform particle sizes and different morphologies, and reduce the generation of impurity. The diagram illustrating the microwave method is shown in Figure 2.3 [41].

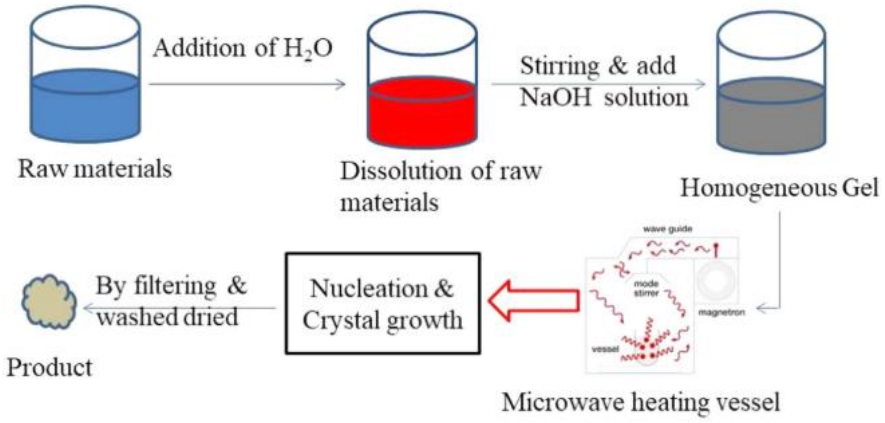


Figure 2.3 Microwave methods for synthesis of zeolites [34].

Le et al. employed microwave-assisted heating techniques to expedite the liquid-phase

synthesis of Y-type zeolites under high-temperature conditions [42]. The synthesis process of Y-type zeolites was thoroughly examined by analysing the effects of different temperatures used for microwave heating, durations of crystallisation, and the ratio between silica and alumina. The utilisation of microwave methods offers numerous advantages. For instance, it facilitates precise time control, resulting in the attainment of higher purity zeolites with smaller particle sizes [43].

### 2.1.2 Solvent-free method

The traditional synthesis of zeolites involves aqueous liquid and solid raw materials, which subsequently undergo gelation or suspension formation during the process. However, in the dry gel conversion (DGC) synthesis method, the solid raw material remains separated from the aqueous liquid and does not directly contact with water [44]. The DGC method consists of a vapor-phase transport (VPT) method and a steam-assisted conversion (SAC) method, as shown in Figure 2.4. The VPT method involves the required volatile structure directing agent for zeolites synthesis with water at the bottom of a kettle, and subsequently reacts it with dry gel present in the upper layer under high-temperature conditions. The SAC method involves initially blending of the structure directing agent with dry gel and subsequently placing the mixture in the upper layer of the kettle.

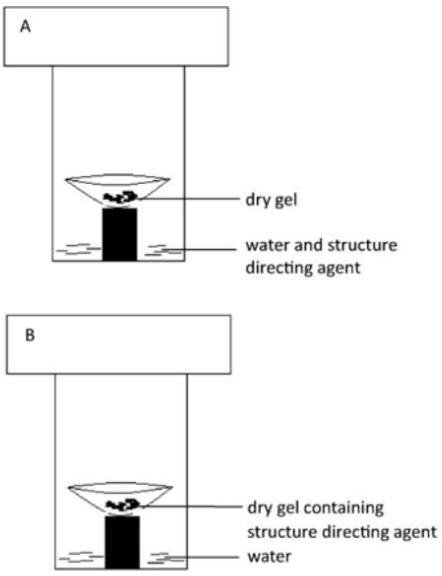

Figure 2.4 Schematic diagram of DGC synthesis method. A: VPT method, B: SAC method [45].

In 1990, Xu et al. employed VPT and SAC methods to synthesise zeolites for the first time. The silica-aluminium amorphous gel was obtained through evaporation of the prepared hydrated gel, then suspended in the mixed steam formed by water and organic amines. Subsequently, this gel transformed into ZSM-5 zeolites under high-temperature conditions [45]. However, the goal of achieving a completely solvent-free synthesis has not yet been achieved, as preparing xerogels still requires significant amounts of solvents.

In 2012, Xiao et al. developed a solvent-free method for zeolite synthesis through mechanical grinding and thermal treatment of raw materials without the addition of water or other solvents [46]. This is followed by direct heating in a sealed container to facilitate the crystallisation process of zeolite (as presented in Figure 2.5). In 2012, Ren et al. applied solvent-free method for the first time to synthesise a series of zeolites, including ZSM-5, ZSM-39, SOD, MOR, Beta, and FAU [46,47]. Compared to the hydrothermal method, the solvent-free approach offers distinct advantages, including higher yields of zeolites, enhanced utilisation of high-pressure reactors and a significant reduction in pollutants. Moreover, this process is characterised by simplicity, low energy consumption, and a substantial decrease in required reaction pressure [21]. The proposed methodology presents a novel avenue for the synthesis of zeolites, holding significant potential for their widespread industrial application. The solvent-free method offers a wider range of applications, shorter crystallisation time, reduced structure directing agent usage, and higher yield compared to the traditional hydrothermal synthesis method.

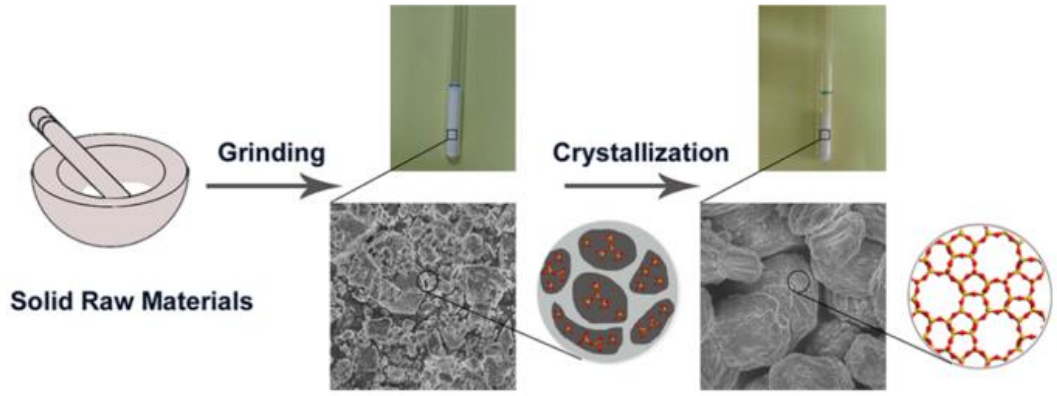


Figure 2.5 Solvent-free synthesis of zeolites [21].

## 2.2 Green strategies for zeolites synthesis

The conventional synthesis via hydrothermal method is not regarded as environmentally sustainable due to the requirement of a large amount of organic templates, which can play a role of structure directing or space filling in zeolites synthesis [2]. The removal of organic templates at high temperature is necessary during the application of zeolites, resulting in the generation of various nitrogen oxides and greenhouse gases. The removal of organic templates results in the release of energy, and this energy, along with its association with the formed water, causes damage to the inorganic structure [48]. In order to address the limitations of the traditional hydrothermal method for zeolites synthesis, it is crucial to choose an environmentally friendly and sustainable approach, including using sustainable materials, reducing reliance on organic templates, and using radicals.

### 2.2.1 Zeolites synthesis with sustainable materials

The recent attention towards the utilisation of natural minerals as sustainable sources for zeolites synthesis stems from their cost-effectiveness, presenting an economically viable substitute to traditional precursors. Li et al. employed attapulgite, a natural clay as an economical and environmentally friendly source of Si/Al to directly synthesised ZSM-5 zeolites via a vapor transformation method. Attapulgite is abundantly present in the zeolites crystallisation recipe, exhibiting a pristine crystal structure and resulting

in remarkable zeolites yield of 96%. The obtained zeolites demonstrate exceptional crystallinity and porosity, comparable to those synthesised using conventional chemical Si/Al sources in terms of their chemical properties [49]. In addition to natural minerals, the residues of silicon or aluminium-containing natural resources have also garnered significant attention. For example, Missengue et al. employed fused coal fly ash extracts as the silicon source to synthesis ZSM-5 zeolites with high purity [50].

The development of low-toxic or biodegradable organic templates derived from biomass materials also holds great potentials for zeolites synthesis. Biomass, defined as materials derived from plants or animals, has garnered tremendous scientific attentions due to its renewable attributes in addressing energy security [51]. Cellulose (as shown in Figure 2.6) is the most prevalent and abundant biopolymers found in nature. It serves as the principal component of plant cell walls and is primarily derived from diverse plant sources such as trees, cotton, bamboo, ramie, and flax [52]. Cellulose is a homopolymer composed of glucose units, which are arranged in a linear, unbranched structure with relatively high molecular weight [53]. Due to its widespread availability, cost-effectiveness, biodegradable and biocompatibility of polymers, as well as its interesting chemical and physical properties, cellulose represents a promising resource for the development of environmentally friendly products across various applications. For instance, cellulose is extensively used in its naturally purified state and also serves as a primary ingredient for the manufacturing of paper, food processing and as additives within the optical and pharmaceutical industries [54]. In addition, cellulose has high plasticity and can take a variety of material forms such as fibre, film, powder, aerogel, hydrogel and sphere. Its structure and performance are controllable, and it has the characteristics of high strength, good biocompatibility and stable chemical properties, making it suitable as the matrix material of nano-catalyst. It can meet the needs for different applications in production and life [55].

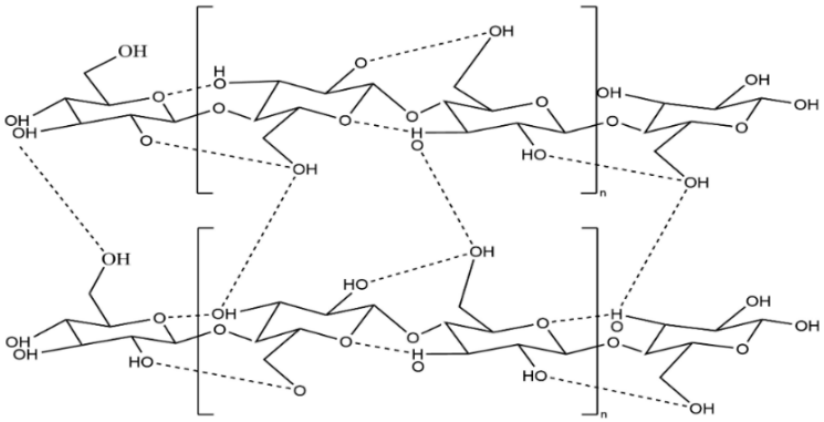

Figure 2.6 The basic structural formula of a cellulose chain.

The abundance of hydroxyl groups in cellulose results in the creation of robust hydrogen bonds, formed internally within the polymeric chains as well as externally between them. Due to the presence of many intramolecular and intermolecular hydrogen bonds in its network structure, cellulose molecules are tightly bound to each other. Additionally, the polyhydroxy structure imparts excellent hydrophilicity to cellulose, making it an outstanding material for providing structural guidance in the process of zeolites synthesis [26].

Tao et al. utilised a biodegradable and environmentally friendly mesoporous template consisting of soluble starch and sodium carboxymethyl cellulose (CMC) to synthesise single crystals with various types of mesopores zeolites (Silicalite-1, ZSM-5 and TS-1).The prepared zeolites exhibit large surface areas and possess mesopores within the zeolitic framework, making them highly advantageous for diverse applications such as catalysis and adsorption and so on [56]. Yu et al. incorporated microcrystalline cellulose (MCC) as a co-template during the hydrothermal synthesis of zeolites. These modified ZSM-5 catalysts were employed in the catalytic decomposition of High-Density Polyethylene (HDPE)and Polypropylene (PP). The incorporation of MCC in ZSM-5 results in an increase in mesopore volume and acid sites, resulting in the maximum oil yields: 21.5% for HDPE and 32.1% for PP. Furthermore, a significant enhancement in light aromatics selectivity was observed, with values reaching 87.6% [57]. Nie et al.

added quaternary ammonium cationic hydroxyethyl cellulose into the synthesis gel of zeolites. This modification resulted in the formation of ZSM-5 nanoparticles (20-80 nm) with hollow structure. These modified nanoparticles were utilised as the catalyst in the process of benzene alkylation with ethanol. The obtained ZSM-5 demonstrated improved catalytic efficiency, exceptional selectivity and remarkable stability (deactivation rate constant of -0.06%/h) in the alkylation process of benzene with ethanol [58]. Zhang et al. employed CNCs and microcrystal cellulose (MCC) as the hard templates to synthesise mesoporous ZSM-5 zeolites, which were then used as the support to prepare the supported nickel (Ni) catalysts for catalytic cellulose conversion. The relevant Ni on mesoporous ZSM-5 catalysts were used for cellulose conversion to hexitols, and the good catalytic activity of the catalysts was ascribed to the presence of mesopores and strong acidity, which was tuned by the addition of CNCs [25].

### 2.2.2 Zeolites synthesis with less organic templates

Numerous efforts have been undertaken to decrease organic templates for zeolites synthesis. Alternative approaches, such as the template-free method, have also been developed, including adjusting the initial ratios of aluminosilicate gel, incorporating structure directing agents and introducing seeds for crystallisation [37]. Awala et al. successfully synthesised the nanosized FAU-type zeolites without any organic structure-directing agents (namely through the template-free method), achieving exceptional high yields of 80%. The obtained zeolites exhibited extremely small crystallites with a narrow distribution of particle sizes (10-15 nm) and possessed micropore volumes of 0.30 $cm^3g^{-1}$, comparable to their conventional counterparts (micrometre-sized crystals). Additionally, they demonstrated excellent colloidal stability [59].

Xie et al. achieved a significant breakthrough in the field of utilizing calcined Beta zeolites seeds as the template without any organic compounds in the initial aluminosilicate gel for Beta zeolites synthesis [60]. The seeds not only facilitated the

growth of Beta zeolites but also significantly decreased the crystallisation time. Liu et al. used nanoscale amorphous protozeolites seeds possessing zeolite-like embryo structures, employed a minimal quantity of structure directing agents and conducted the synthesis of single-crystalline ZSM-5 zeolites at mild temperatures. The presence of amorphous nanosized seeds facilitated the formation of numerous nucleation sites, effectively accelerating the crystallisation process of surrounding nutrients. Subsequently, oriented assembly and merging of crystallites occurred, ultimately leading to the formation of a hierarchical ZSM-5 structure (mesopore volume of 0.51 $cm^3g^{-1}$).The obtained ZSM-5 zeolites exhibited a highly completed framework, demonstrating an exceptionally extended lifespan of 443.9 hours and a remarkable selectivity to propylene at a weight hourly space velocities (WHSV) of $2h^{-1}$ during the methanol-to-propylene (MTP) reaction [61].

### 2.2.3 Zeolites synthesis with •OH

#### 2.2.3.1 Introduction of •OH

Radicals refer to atoms or molecules that can possess one or more unpaired electrons, such as superoxide radicals, hydroperoxides, hydroxyl free radicals, alkoxy radicals. •OH, one of the most powerful oxidizing agents, is widely distributed in natural environments, including water, the atmosphere, biological system, and interstellar space [62]. •OH has garnered significant attention due to its important role in advanced oxidation technology for wastewater treatment: (i) degradation of man-made, toxic and non-biodegradable aromatic compounds (phenols, chlorophenols, nitrophenols) [63]; (ii) degradation of dyes that are toxic to microorganisms, aquatic organisms and humans [64]; (iii) degradation of wastewater containing drugs (antipyretics, antibiotics, anti-depressants) [65]; (iv) degradation of common residues of pesticides (herbicides, insecticides, fungicide) in surface and groundwater [66]. Treatment of •OH has also been applied to some other pollutants, such as carboxylic acids, pathogens and industrial effluents.

•OH consists of an oxygen atom bonded with a hydrogen atom, making them highly reactive and prone to snatching hydrogen atoms from other molecules in order to form water. Feng et al. made an observation that •OH was detected during the hydrothermal synthesis of zeolites and also found that the introduction of •OH in the synthesis system significantly expedited the crystallisation process [24]. This achievement provides a novel perspective in the application of •OH in the synthesis of porous materials.

### 2.2.3.2 Methods of producing •OH

The Fenton technique is a widely recognized chemical approach for generating •OH. In this method, ferrous ions serve as a catalyst to break down hydrogen peroxide, and •OH are generated through the reaction described in chemical equation 2.1:

$$Fe^{2+} + H_2O_2 \rightarrow Fe^{3+} + \bullet OH + OH^- \qquad \text{(eq.2.1)}$$

The Fenton method is usually combined with some physical methods such as ultraviolet irradiation, ultrasonication and electrochemical methods to generate •OH with higher efficiency and lower cost [67].

In addition to hydrogen peroxide, persulfate can also be used as an initiator to generate •OH. Persulfates can be catalysed to produce sulphate radicals by transition metals, ultraviolet irradiation and heating. The sulphate radicals are a strong oxidizing agent that can generate •OH through the chemical reactions described in equations 2.2 to 2.4 [68].

$$S_2O_8^{2-} + \text{Heat/UV} \rightarrow 2SO_4^- \bullet \qquad \text{(eq.2.2)}$$

$$\text{All pH: } 2SO_4^- \bullet + H_2O \rightarrow SO_4^{2-} + \bullet OH + H^+ \qquad \text{(eq.2.3)}$$

Alkaline pH: $2SO_4^{-}\bullet + OH^{-} \rightarrow SO_4^{2-} + \bullet OH$ (eq.2.4)

In short, in the synthesis systems of zeolites and other porous materials, •OH are mainly generated through physical methods such as radiation, ultrasonication and photolysis, as well as chemical method like Fenton method, ozone method. The methods are shown in Figure 2.7.

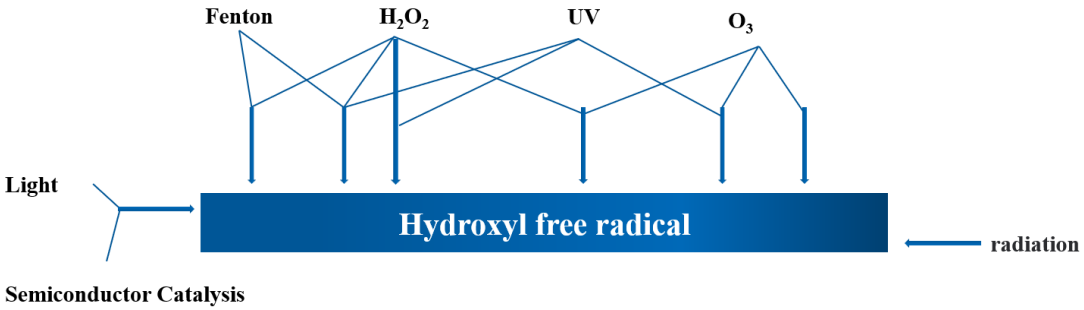


Figure 2.7 Methods to generate of •OH.

### 2.2.3.3 •OH assisted synthesis

In the process of hydrothermal crystallisation of zeolites in alkaline conditions, the presence of hydroxide ions ($OH^{-}$) facilitates the depolymerisation of aluminosilicate gel by breaking Si,Al–O–Si,Al bonds. At the meantime, •OH also facilitates the formation of polymerized aluminosilicate anions surrounding the hydrated cation species by reestablishing the Si,Al–O–Si,Al bonds. According to this, Feng et al. introduced •OH to replace part of $OH^{-}$ in the zeolites hydrothermal process for the first time [24]. The presence of •OH, generated by ultraviolet irradiation or Fenton's reagent, has been reported to play a significant role in the crystallisation process of various zeolites (e.g., Na–A, Na–X, NaZ–21, and Silicalite-1), effectively accelerating the crystallisation process by promoting the nucleation. According to Density Functional Theory (DFT), it was observed that the presence of •OH in alkaline media resulted in lower activation energies. This observation further supports the notion that •OH exhibits

higher catalytic activity compared to $OH^-$, facilitating the breaking of Si,Al−O−Si,Al bonds and formation of new Si,Al–O–Si,Al bonds [24].

Since the discovery of the role of •OH in zeolites synthesis, •OH assisted synthesis has attracted extensive attention. Chen et al. introduced •OH into zeolite synthesis process through Gamma rays (γ-rays) irradiation for the first time [69]. The γ-ray irradiation significantly enhanced the crystallisation process of zeolite NaA, NaY, Silicalite-1, and ZSM-5. Remarkably, at room temperature, the crystallisation time of NaA zeolites was reduced to 18 hours compared to the conventional method which required 102 hours. Furthermore, more mesopores and higher surface area were generated during this process, leading to an unexpected 6-fold and 4-fold increase in the adsorption capacity of $CO_2$ compared to the NaA and ZSM-5 zeolites prepared without γ-rays irradiation, respectively [69].

Cheng et al. employed sodium persulfate as a radical promoter to generate high activate •OH in the crystallisation process of zeolites. The presence of sodium persulphate as a catalyst in the hydrothermal synthesis process resulted in a reduction of the crystallisation time for highly crystalline Silicalite-1 from 24 hours to 16 hours. This catalyst facilitated the depolymerisation and repolymerisation of Si-O-Si bonds. Furthermore, the employment of sodium persulfate as a catalyst can also effectively produce Silicalite-1 with significantly reduced usage of organic structure-directing agents while maintaining its high crystallinity [23].

Apart from the methods mentioned above, •OH can be produced in the synthetic system through the utilisation of crystals that have undergone radicalization. The zeolite crystals can be milled and heated to form the surface non-bridging oxygen hole centre (≡Si–O•). Cheng et al. employed the active ≡Si–O• radicals to react with water, resulting in the generation of •OH, thereby accelerating the crystallisation process of Na-A and nanosized Silicalite-1 compared to the non-radicalized seeds. The utilisation

of radicalized seeds facilitated the crystallisation and production of solid products compared to non-radicalized seeds [70].

The synthesis routes assisted by •OH can also be combined with other synthetic pathways. Han et al. proposed a unique strategy that involves the integration of a solvent-free technique with Fenton's reagent to produce Fe-ZSM-5 zeolite. This innovative approach resulted in remarkable improvements in crystallinity, while also reducing the duration of high-temperature crystallisation. The Fe-ZSM-5 zeolite obtained was utilised as a catalyst for phenol hydroxylation, exhibiting considerably improved catalytic efficiency compared to the reference catalyst prepared through traditional solvent-free techniques. The improved performance of the Fe-ZSM-5 catalyst was ascribed to its large surface area, increased mesoporous volume, as well as its enrichment towards phenol [71]. Wang et al. employed a combination of the hydroxyl free radical-assisted route and post-synthesis treatment to form the Y zeolites with a high $SiO_2/Al_2O_3$ ratio (SAR), which was extensively utilised in the fluidized catalytic cracking process. The utilisation of DFT calculations demonstrated that the presence of •OH selectively promoted the formation of Si-O-Si bonds, leading to an improved SAR value of 6.35 [72].

## 2.3 Catalytic hydrogenation of $CO_2$ by zeolites

### 2.3.1 $CO_2$ hydrogenation to valuable products

$CO_2$ is the primary component of greenhouse gases, posing a significant threat to the world due to its contribution to irreversible changes of the world's climate. Currently, annual $CO_2$ emission approach approximately 230 million tons, but the utilisation of $CO_2$ is less than 1% of the its emissions [73]. Undoubtedly, the reduction of $CO_2$ emission has emerged as an imperative concern, with carbon capture and storage (CCS) widely regarded as the most effective technology in addressing this challenge [74]. However, the process of capturing and storing $CO_2$ faces numerous technical and economic challenges, such as the need for liquefaction, transportation, and burial of

$CO_2$, which significantly increases the cost of CCS [75]. Hence, a related alternative concept of carbon capture and utilisation (CCU) has gained significant interest for its ability to convert the waste $CO_2$ into valuable products. Considering the high levels of fuels consumption, producing fuels such as $CH_4$, methanol or dimethyl ether should be regarded as the optimal approach for mitigating their usage. The methanation of carbon dioxide following the Sabatier reaction is considered as the most thermodynamically advantageous reaction among various hydrogenation reactions. In addition, the transportation of $CH_4$, being the primary constituent of natural gas (NG), can be safely facilitated through existing NG infrastructures [76].

The recent advancements in the conversion of $CO_2$ into $C_{2+}$ products through hydrogenation have also demonstrated remarkable improvements in energy densities and economic values. For example, the production of dimethyl ether (DME) through the hydrogenation of $CO_2$ has witnessed significant advancements through the integration of methanol synthesis catalysts with methanol coupling catalysts [77]. Bonura et al. utilised a combination of CuZnZr methanol catalyst and two different zeolites, specifically ferrierite (FER) and mordenite (MOR), to examine the catalytic performance in the "one-step" hydrogenation reaction to convert $CO_2$ into DME. The hybrid FER-based catalyst exhibited excellent $CO_2$ conversion, achieving a maximum conversion of 29% at 280℃. Moreover, it also demonstrated remarkable DME productivity (more than 62%), without any coke formation under the conducted experimental conditions [78]. Bansode et al. also successfully enhanced the selectivity to DME (89%) in a one-step conversion of $CO_2$ into DME by utilizing a mixed bed consisting of $Cu/ZnO/Al_2O_3$ and H-ZSM-5 catalysts and maintained a high level of $CO_2$ conversion (over 30%) [79]. Singh et al. employed a $Cu\text{-}ZnO\text{-}ZrO_2$/hierarchical ZSM-5 catalyst for the one-step production of DME through $CO_2$ hydrogenation. The DME selectivity achieved a remarkable value to 60% with $CO_2$ conversion of 14% at 260℃ [80].

Gao et al. employed a bifunctional catalyst, comprising of partially reduced $In_2O_3$ and

HZSM-5, which demonstrate remarkable selectivity towards value-added products. The selectivity of hydrocarbons in the gasoline range reached 78.6% while containing only 1% $CH_4$, and the $CO_2$ conversion rate was 13.1%. The activation of $CO_2$ and $H_2$ was facilitated by the existence of oxygen vacancies on the surface of $In_2O_3$, resulting in the production of methanol. Subsequently, zeolite pores facilitated C−C coupling reactions to generate high-octane number gasoline-range hydrocarbons [81].

In addition to the production of gasoline, $CO_2$ hydrogenation has been utilised for the formation of aromatic compounds including benzene, toluene, and xylene. Ni et al. have achieved an impressive aromatic selectivity of 73.9% while maintaining a remarkably low $CH_4$ selectivity of 0.4% and achieving a $CO_2$ conversion rate of 9.1% in the absence of CO during the process of $CO_2$ hydrogenation over $ZnAlO_x$/H-ZSM-5 catalysts [82].

The production of olefin products typically involves the utilisation of zeolites with smaller pore sizes, as opposed to the commonly used ZSM-5, HY, and HBeta zeolites in gasoline and aromatic production [83]. The SAPO-34 zeolites, which has a pore opening size of 0.38 nm, exhibited a remarkable selectivity to $C_2$-$C_4$ olefins (about 90%) [84]. Tong et al. employed different metals (Zn, Zr, or Mn) to finely tune the acidity of zeolites in the composite catalyst ZnO-ZrO/M-SAPO-34, where M represented the metal used for acidity modification. The modified zeolites with Mn metal achieved the highest $CO_2$ conversion rate of 21.3%, effectively suppressing the selectivity of CO and $CH_4$ to below 43% and 4%, respectively. The light olefin selectivity was 61.7% and the $CH_4$ selectivity remained below 4% [85].

Metal–zeolite catalysts present numerous benefits for $CO_2$ conversion, showing promising outcomes in terms of both efficiency and selectivity owing to their distinctive properties including large surface area, unique pore size and tuneable acidity. The framework topology of zeolites is also a significant factor affecting the distribution of production by regulating the access and diffuse of molecules in the pores. In addition to the zeolite topology, the selectivity of products is significantly affected by the acidity

type (Brønsted or Lewis), density, and strength of acid sites in zeolites [86,87].

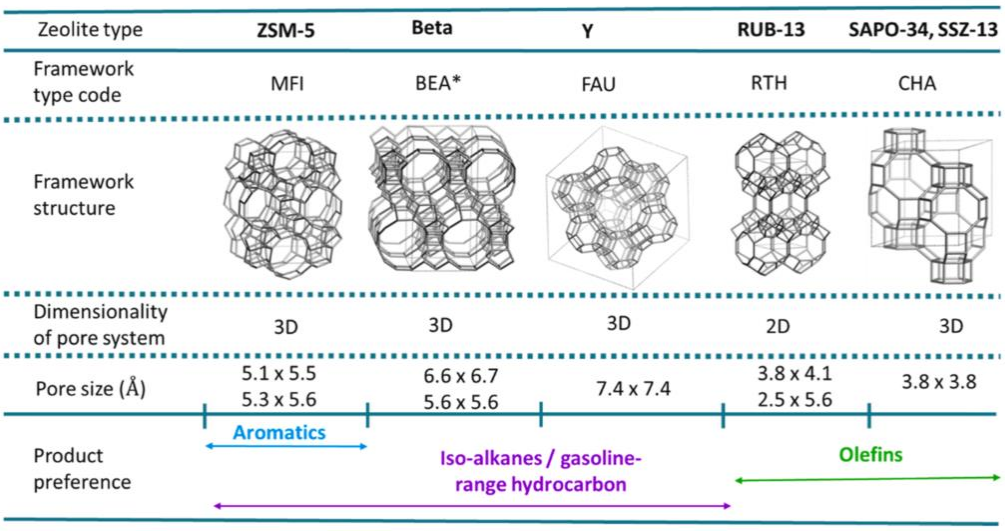


Figure 2.8 The structures of zeolites and their corresponding preferences for products [83].

The conversion of $CO_2$ into various products, such as methanol, dimethyl ether, ethanol, olefins, aromatics, and long-chain pathways is summarized in Figure 2.9.

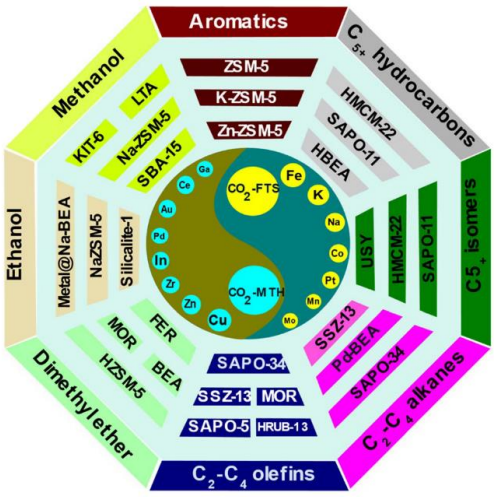


Figure 2.9 Illustration of metals and zeolites employed for hydrogenation of $CO_2$ to selectively product [88].

### 2.3.2 Zeolites for direct $CO_2$ hydrogenation to $CH_4$

The production of $CH_4$, also known as the Sabatier reaction, is the catalytically

hydrogenation of $CO_2$ and by $H_2$ to produce $CH_4$. The process of methanation can also utilise alternative reactions, such as the CO methanation reaction and reverse dry reforming reaction, to synthesise $CH_4$ [89]. The methanation of $CO_2$ can occur via two distinct pathways, as shown in Figure 2.10.

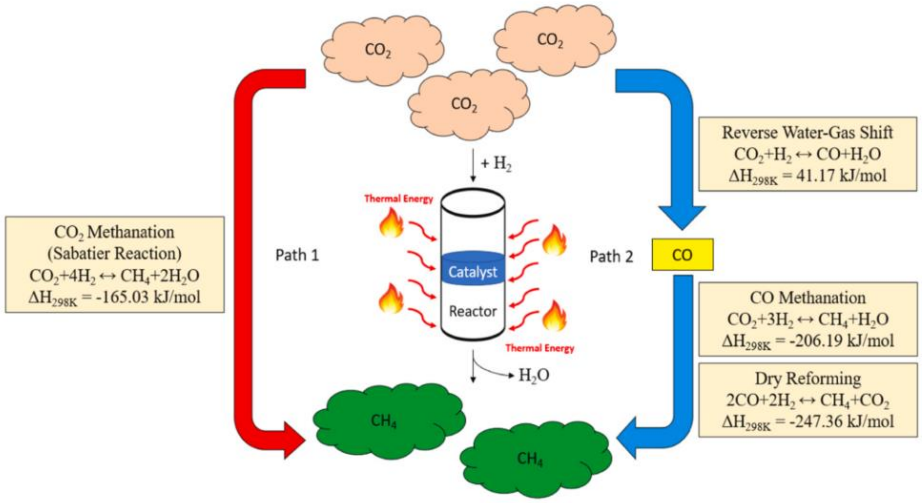


Figure 2.10 Potential routes for the reaction of $CO_2$ hydrogenation to $CH_4$ [89].

One possible approach is the direct hydrogenation of $CO_2$, resulting in the formation of $CH_4$ and $H_2O$ (as shown in eq. 2.5). Another pathway involves converting $CO_2$ into CO firstly through eq. 2.6, followed by hydrogenation of CO to produce $CH_4$ using either eq. 2.7 or eq. 2.8. The RWGS reaction (eq. 2.6), which generates CO as by-products at high temperatures. Additionally, the coke formation is also observed under elevated temperatures. Therefore, to optimize $CH_4$ yield and reduce coking, it is essential to conduct the methanation reaction at lower temperatures.

$$CO_2 + 4H_2 \leftrightarrow CH_4 + 2H_2O \qquad \Delta H_{298\,K} = -165.03\ \text{kJ/mol} \qquad \text{(eq.2.5)}$$

$$CO_2 + H_2 \leftrightarrow CO + H_2O \qquad \Delta H_{298\,K} = 41.17\ \text{kJ/mol} \qquad \text{(eq.2.6)}$$

$$CO + 3H_2 \leftrightarrow CH_4 + H_2O \qquad \Delta H_{298\,K} = -206.19\ \text{kJ/mol} \qquad \text{(eq.2.7)}$$

$$2CO + 2H_2 \leftrightarrow CH_4 + CO_2 \qquad \Delta H_{298\,K} = -247.36\ kJ/mol \qquad \text{(eq.2.8)}$$

In order to optimize the efficiency and precision of $CO_2$ conversion into $CH_4$ (e.g., achieving elevated $CO_2$ conversion, selectivity towards $CH_4$ and space time yield, etc.), significant efforts have been devoted to the development of innovative catalysts [90].

Various metals have exhibited activity in the process of $CO_2$ methanation, including nickel (Ni), ruthenium (Ru), rhodium (Rh), platinum (Pt), palladium (Pd), cobalt (Co) and iron (Fe) [89]. According to Fischer et al., the catalytic activity of unsupported metal catalysts under methanation conditions was ranked as follows: Ru > Ir > Rh > Ni > Co > Os > Pt > Fe > Mo > Pd > Ag [91]. However, when evaluating the catalyst's activity, it is crucial to consider the accessible metal surface area. According to the findings, the trend in activity was ranked as follows: Ru > Fe > Ni > Co > Rh > Pd > Pt > Ir [92]. Furthermore, Mills et al. summarized the activity and selectivity of supported metal catalysts as follows: Ru > Fe > Ni > Co > Mo for activity, and Ni > Co > Fe > Ru for selectivity [93]. Among them, Ni-based catalysts have garnered significant attention for industrial applications because of their remarkable selectivity, good activity, low cost and ease of availability.

Additionally, the performance of catalysts was influenced by several factors, including the dispersion of metals, alkalinity, and the interaction between metals and their support. Therefore, various supports such as $Al_2O_3$, $TiO_2$, $ZrO_2$ and $CeO_2$ have been utilised for the purpose of $CO_2$ methanation. Presently, there has been a growing interest in utilizing various innovative catalysts like mesoporous materials, carbons, hydrotalcite-derived materials, and zeolites for $CO_2$ methanation [94].

Among them, MFI-type zeolites (e.g., ZSM-5, Silicalite-1) are commonly used for $CO_2$ methanation due to their potential environmental and economic benefits compared to commercial $Ni/Al_2O_3$ catalysts, such as high surface area, improved metal dispersion, unique acid-base properties, tailored pore structure, good resistance to coke formation

and enhanced selectivity. [95]. Specifically, the high surface area of MFI-type zeolites plays a crucial role in improving the dispersion of metallic nanoparticles, thereby reducing their susceptibility to high-temperature sintering [96]. The porosity of MFI-type zeolites facilitates the diffusion of $CO_2$ and promotes the conversion of $CO_2$. In addition, the high alkalinity of MFI-type zeolites enhances the adsorption and hydrogenation of $CO_2$ while the surface hydrophobicity suppresses deactivation due to the lower affinity to $H_2O$ generated during $CO_2$ methanation [97]. These advantages make MFI-type zeolites promising catalytic supports for $CO_2$ methanation and Silicalite-1 can be a good candidate as it possesses highest alkalinity and hydrophobicity among MFI-type zeolites.

According to the findings of Guo et al., among all the support materials tested, including SBA-15, $Al_2O_3$, $SiO_2$ and MCM-41, the catalytic activity of Ni supported on ZSM-5 was found to be the highest. Remarkably, Ni/ZSM-5 exhibited high stability without any deactivation for up to 100h. The excellent ability to convert $CO_2$ and selectivity to $CH_4$ can be attributed to the finely dispersed Ni particles present on the highly porous structure with an ordered arrangement in ZSM-5. Additionally, the methanation reaction is further enhanced by the presence of abundant weak and medium basic sites in Ni/ZSM-5 [98].

Scirè et al. investigated the effect of supports on the performance of Ru-supported catalysts for $CO_2$ methanation using FT-IR analysis. The researchers loaded 2 wt% Ru onto two different types of silica materials and H-ZSM-5 zeolites. They proposed that the process of $CO_2$ methanation is a consecutive reaction, starting with the dissociation of $CO_2$ into adsorbed CO, followed by the hydrogenation of CO. The scientists noted improved outcomes when utilizing the catalysts based on zeolites, which they attributed to the enhanced interactions between Ru and ZSM-5 materials. These interactions were found to have an influence on the selectivity of $CH_4$ [99].

Delmelle et al. employed impregnation method to improve the water uptake capacity of

5 wt.% Ni-based 13X and 5A zeolites. The two catalysts exhibited comparable $CO_2$ conversion rates and selectivity towards $CH_4$ [100]. Furthermore, Borgschulte et al. conducted an ion-exchange method to prepare Ni-5A catalysts containing less than 6 wt.% of Ni. Doubling the stoichiometric ratio of $H_2$ to $CO_2$ to 8:1 led to approximately complete conversion of $CO_2$ into $CH_4$ [101]. Additionally, Walspurger et al. discovered that incorporating hydrophilic 4A zeolites into a Ni-based commercial catalyst, the sorption-enhanced methanation process was successfully demonstrated under atmospheric pressure, achieving nearly 100% conversion at temperatures ranging from 250 to 350°C [102]. The significant performance of these catalysts was attributed to the water-absorbing properties of the zeolites used, which facilitated the shift towards $CH_4$ formation during reaction.

In conclusion, Ni is a highly effective catalyst for the hydrogenation of $CO_2$ to $CH_4$. However, Ni-based catalysts can potentially undergo oxidation to form NiO in $CO_2$ methanation, leading to the catalyst deactivation (*i.e.*, reduced $CO_2$ conversion and methane selectivity). Using appropriate catalytic supports, such as zeolites, can optimise the physical and chemical properties of catalysts and suppress the formation of NiO, improving the catalytic performance of Ni-based catalysts. Zeolites serve as exceptional support materials for metal active sites, characterised by their uniform pore structures, high specific surface areas, and remarkable hydrothermal stability. Ni-zeolites have been extensively utilised as the catalysts in the research field of $CO_2$ conversion to $CH_4$. The combination of the Ni and zeolites can significantly enhance the efficiency and precision of $CO_2$ conversion into $CH_4$.

Table 2.1 Summary of Ni-based catalyst with various supports.

| Catalyst | $H_2$: $CO_2$ ratio | temperature (°C) | pressure (MPa) | $X_{CO_2}$(%) | $S_{CH_4}$(%) | Ref. |
|---|---|---|---|---|---|---|
| Ni/$ZrO_2$ | 12.5 | 377 | 0.1 | ~100 | ~100 | [103] |
| Ni/$CeO_2$ | 5 | 450 | 0.1 | ~80 | ~100 | [104] |
| Ni/$CeO_2$-$ZrO_2$ | 4 | 275 | 0.1 | 55 | 99.8 | [105] |
| Ni/$TiO_2$ | 4 | 450 | 0.1 | ~70 | ~99 | [104] |
| Ni/$Al_2O_3$ | 4 | 250 | 0.1 | 39 | 97 | [106] |
| Ni/γ–$Al_2O_3$ | 3 | 210 | 2 | 80 | 99.5 | [107] |
| Ni/$Al_2O_3$-$ZrO_2$ | 4 | 300 | 0.1 | 77 | ~100 | [108] |
| Ni/$SiO_2$ | 4 | 450 | 0.1 | 36.8 | 81.8 | [109] |
| Ni/NaY | 4 | 500 | 0.1 | 67 | 94 | [110] |
| Ni/MCM-41 | 4 | 400 | 0.1 | ~63 | ~63 | [98] |
| Ni/SBA-15 | 4 | 400 | 0.1 | ~70 | ~65 | [98] |
| Ni/USY | 4 | 450 | 0.1 | 72.66 | 95 | [111] |
| Ni/ZSM-5 | 4 | 400 | 0.1 | 76 | 99 | [98] |
| Ni/$CeO_2$/ MCM-41 | 4 | 380 | 0.1 | 85.6 | 99.8 | [112] |

# 3. Experimental

## 3.1 Materials and reagents

Table 3.1 Materials and chemical reagents used in this experiment.

| Name | Grade | Chemical formula | Manufacturer |
|---|---|---|---|
| Tetrapropylammonium hydroxide solution (TPAOH) | 25% in water | $C_{12}H_{29}NO$ | Shanghai Macklin Biochemical Co. Ltd.,China |
| Tetraethyl orthosilicate (TEOS) | 99.99% metals basis | $(C_2H_5O)_4Si$ | Aladdin Reagent Co. Ltd., Shanghai, China |
| Sodium persulfate | AR Chemical Reagent | $Na_2S_2O_8$ | Shanghai Macklin Biochemical Co. Ltd.,China |
| Nickel nitrate | AR, 99% | $Ni(NO_3)_2 \cdot 6H_2O$ | Shanghai Macklin Biochemical Co. Ltd.,China |

## 3.2 Synthesis of Silicalite-1 materials

### 3.2.1 Synthesis of Sililcalite-1 via conventional route

Different amounts of tetrapropyl ammonium hydroxide (TPAOH) aqueous solution (10.047, 7.5353 and 5.0235 g) were first mixed with deionized water (22.66, 20.15 and 17.64 g) for 10 minutes. Subsequently, under continuous stirring, 8.03 g of tetraethyl orthosilicate (TEOS) was added dropwise into the solution and stirred for 5 hours. The resulting solution was transferred to a Teflon-lined stainless-steel autoclave with a capacity of 100 mL and heated in an oven at 90℃ for crystallisation. After hydrothermal crystallisation for 24h, the product was separated by centrifugation at 10506 rpm and washed with water till the pH reached neutral, and subsequently dried overnight at 70℃.

The dry product was calcined at 550℃ in a muffle furnace for 5h to remove the template. The TPAOH usage is defined as 100% when it weighed 10.047 g, 75% when it weighed 7.5353 g, and 50% when it weighed 5.0235 g. The corresponding samples were named as 100%S1-0M-0 when the TPAOH concentration was 100%, while they are labelled as 75%S1-0M-0 and 50%S1-0M-0 for concentrations of 75% and 50% respectively.

### 3.2.2 Syntheses of Silicalite-1 in the presence of •OH

Different amounts of TPAOH aqueous solution (10.047, 7.5353 and 5.0235 g) were first mixed with deionized water (22.66, 20.15 and 17.64 g) for 10 minutes. Subsequently, under continuous stirring, 8.03 g of tetraethyl orthosilicate (TEOS) was added dropwise into the solution and stirred for 5 hours. The resulting solution was transferred to a Teflon-lined stainless-steel autoclave with a capacity of 100 mL. Various volumes of SPS solution (0, 0.5 and1mL) were added into the resulting solution to make the final concentrations of SPS 0 M, 0.01 M and 0.02 M. The mixture was then heated in an oven at 90℃ for crystallisation, The subsequent procedures were identical as described in section 3.2.1. The zeolites with SPS were correspondingly denoted as XS1-Y-0, where X represented the TPAOH usage (50%, 75% and 100%) and Y represented the SPS concentration (0, 0.01 and 0.02).

### 3.2.2 Synthesis of Silicalite-1 in the presence of •OH and CNCs

Different amounts of TPAOH aqueous solution (10.047, 7.5353 and 5.0235 g) were first mixed with deionized water (22.66, 20.15 and 17.64 g) for 10 minutes. Subsequently, under continuous stirring, 8.03 g of tetraethyl orthosilicate (TEOS) was added dropwise into the solution and stirred for 4.5 hours. The amount of CNCs (0, 0.33, 0.65, 0.825, 1, 1.15, 1.3) were added into the Silicalite-1 precursor and kept stirring for additional 0.5 hours in order to facilitate the separation of CNCs. The resulting solution was transferred to a Teflon-lined stainless-steel autoclave with a capacity of 100 mL. t arious volumes of SPS solution (0, 0.5 and1mL) were added into the resulting solution to make the final concentrations of SPS 0 M, 0.01 M and 0.02 M. The subsequent procedures

were identical as described in section 3.2.1. Silicalite-1 zeolites containing only CNCs were designated as XS1-0M-Z, containing both CNCs and SPS were designated as XS1-Y-Z, X represented the TPAOH usage (50%, 75% and 100%), Y represented the SPS concentration (0, 0.01 and 0.02) and Z represented the CNCs contents (0, 0.33, 0.65, 0.825, 1, 1.15, and 1.3). The designated names for all the samples in this study are summarised in Table 3.2.

Table 3.2 Table of Silicalite-1 zeolites.

| Sample name (XS1-Y-Z) | X= TPAOH usage | Y=SPS usage (mol/L) | Z=CNCs usage (wt%) |
|---|---|---|---|
| 100%S1-0.02M-0 | 100% | 0.02 | 0 |
| 100%S1-0.02M-0.65 | 100% | 0.02 | 0.65 |
| 100%S1-0M-0.65 | 100% | 0 | 0.65 |
| 100%S1-0M-0 | 100% | 0 | 0 |
| 75%S1-0.02M-Z | 75% | 0.02 | 0, 0.33, 0.65, 0.825, 1, 1.15, 1.3 |
| 75%S1-0M-0.65 | 75% | 0 | 0.65 |
| 50%S1-0.02M-Z | 50% | 0.02 | 0, 0.33, 0.65, 0.825, 1, 1.15, 1.3 |
| 50%S1-0.01M-Z | 50% | 0.01 | 0, 0.33, 0.65, 0.825, 1, 1.15, 1.3 |
| 50%S1-0M-Z | 50% | 0 | 0, 0.33, 0.65, 0.825, 1, 1.15, 1.3 |

### 3.2.3 Synthesis of Ni/Silicalite-1 catalysts

The wet impregnation method was employed to prepare the Ni/Silicalite-1 catalyst. A solution containing 0.07 5g of Ni $(NO_3)_2 \cdot 6H_2O$ dissolved in 10 mL of deionized water was prepared, followed by the addition of 0.1 g of Silicalite-1 powders into the solution. Subsequently, the dry product was calcined in a muffle furnace at 550℃ for 5h at a heating rate of 1℃/min. The Ni/Silicalite-1 catalyst was in-situ reduced at 500°C for 3h in an $H_2/N_2$ environment (with a flow rate of 10.0/10.0 mL/min) before use for $CO_2$

hydrogenation. The theoretical Ni content in the catalyst was 15 wt%.

## 3.3 Characterisations

### 3.3.1 X-ray Diffraction (XRD)

XRD technique is extensively employed as a characterisation method to examine the physical attributes of various samples, encompassing powder, solid, and liquid materials. It enables the analysis of phase composition, crystal structure, and sample orientation. In this study, XRD tests were undertaken by a Bruker D8 advance, as presented in Figure 3.1. This instrument consists of three crucial elements: an X-ray generator, a specimen holder, and a detector for XRD. For each XRD test, 0.02 g of sample was weighed and placed in the sample holder. The specific conditions for XRD tests were as follows: 2θ: 5─90°, 0.02°/step, 0.58 s/step.


Figure 3.1 The image of XRD (Bruker D8 advance).

### 3.3.2 $N_2$ adsorption-desorption

The specific surface area and the pore size distribution were characterised by $N_2$ adsorption at 77K, based on the physical adsorption phenomenon of gases on the inner and outer surfaces of the porous material. The $N_2$ adsorption-desorption equipment and degas equipment are depicted in Figure 3.3. The procedure for sample preparation in

this measurement is as follows: Firstly, an empty tube was weighed and referred to as M1, then 0.2~0.3 g of a dried sample was placed into the tube, and the total weight of the sample and the tube was measured and referred to as M2; finally, the sample was degassed overnight at 350℃. After degassing, the tube and the sample were weighed and referred to as M3. The values of M1 and M3 were inputted into the software, followed by selecting the micropore method to initiate the test. The correct degassing process is indicated when M3≤M2, signifying the successful removal of moisture or absorbed pollutants from the sample. These tests were conducted on micromeritics 3FLEX equipment.

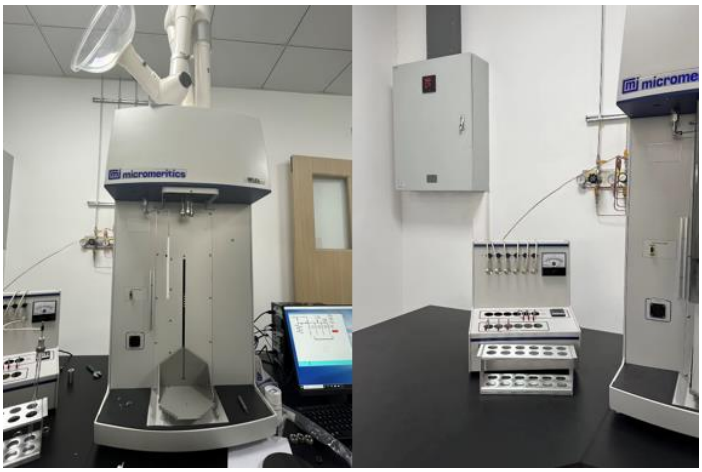


Figure 3.2 $N_2$ adsorption-desorption equipment and degas equipment (3 FLEX).

### 3.3.3 Scanning Electron Microscope (SEM)

SEM (as shown in Figure 3.6) is a technique that involves raster scanning the surface of a sample by focusing an electron beam emitted from an electron gun. The composition, morphology, and structure of the sample surface can be analysed through the detection of signals generated from electron-sample interactions. It comprises three primary components: an electro-optical column, a sample chamber, and a computer/electronic controller for SEM. SEM and EDS were undertaken by a Gemini SEM 360 using a work distance of 10-15 mm and an accelerating voltage of 20 kV. The specific operational procedures were as follows: firstly, samples were dispersed using

ethanol; secondly, a droplet was extracted using an eyedropper onto the sample table coated with conductive glue; thirdly, the sample was gold-coated to achieve a thickness of approximately 10 nm.


Figure 3.3 The image of SEM-EDS equipment (Gemini SEM 360).

### 3.3.4 Transmission Electron Microscopy (TEM)

TEM is a method of analysis used to observe the tiniest structures in substances. Unlike optical microscopes that utilise visible light, TEM has the capability to reveal remarkable atomic-level intricacies by enlarging nanometre structures up to 50 million-fold. It comprised by an electron optical system, a vacuum system, and a power supply and control system. The TEM micrographs were acquired using a FEI Tecnai G2 F20 electron microscope operated at 200 kV in this study, which was tested at Shenyang National Laboratory for Materials Science.

### 3.3.5 Inductively Coupled Plasma Optical Emission Spectrometry (ICP-OES)

The ICP-OES technique is a highly robust, versatile, and cutting-edge analytical method that is widely recognized for its exceptional detection capabilities. It enables the determination of all metallic elements as well as some non-metallic elements. ICP-

OES was undertaken by a SPECTROBLUE equipment.


Figure 3.4 The image of ICP-OES equipment (SPECTROBLUE).

## 3.4 Mechanism study

In this study, Fourier Transform Infrared Spectroscopy (FT-IR) spectroscopy was employed to identify changes in functional groups in molecules for Silicalite-1 synthesis in the presence of •OH and CNCs. Additionally, Thermogravimetric Analysis (TGA) tests were conducted to infer the decomposition of CNCs in the reaction system.

FT-IR analysis is a method used to explore the molecular composition and chemical bonding of materials. The detection principle of FTIR is theoretically based on the Lambert-Beer law. The main components of the system include an infrared light emitter, a diaphragm, an interferometer (comprising a beam splitter, a mirror in motion, and a stationary mirror), a sample enclosure, a sensor, different infrared mirrors, lasers, control circuitry boards, and power sources. Figure 3.3 illustrates the FTIR equipment. The sample preparation procedure for FTIR measurement was as follows: 0.002 g of the sample and 0.2 g of KBr were accurately weigh, then the mixture was transferred into a mortar for thorough blending. Subsequently, the mixture was transferred into the designated mould and firmly insert it into the tablet press under a pressure of 10 MPa

for a duration of 1 minute. Upon removal, the resulting specimen manifests as a translucent sheet, facilitating unhindered transmission of diverse infrared wavelengths to generate distinct peak curves for subsequent analysis. These tests were conducted on BRUKER INVENIO S equipment.

Figure 3.5 The image of FT-IR (BRUKER INVENIO S).

TGA works by measuring the change in mass of a sample as a function of temperature (or time) under controlled conditions. The equipment typically consists of a thermobalance, a heating furnace, a programmed temperature control system, and an atmosphere control system. These components work together to create a controlled environment in which the sample's mass changes can be precisely monitored as the temperature increases. The TGA equipment and the loading position for samples are depicted in Figure 3.6. TGA measurement sample preparation was as follows: the desiccated samples were accurately weighed at a dosage range of 5 to 10 mg before being transferred into the crucible. The temperature was then gradually increased at a controlled rate of 1°C/min until it reaches 550°C, with an airflow rate of 10 mL/min. These tests were conducted on SDTQ600 equipment.

Figure 3.6 The image of TGA equipment and the loading position for samples (SDTQ600).

## 3.5 Catalytic tests

The catalytic test for $CO_2$ hydrogenation was performed in a fixed-bed reactor, as presented in Figure 3.7. In a typical experiment, 0.1 g of pelletized Ni-Silicalite-1 catalyst (pellets size of 208~354 μm) was packed in the reactor. The operational procedure was as follows. Firstly, the reactor was purged with argon gas to remove the air in the reactor, while the outlet tubing was placed in a beaker filled with water to observe the bubble generation for checking the pipeline connectivity. Secondly, the gas flowrates for the reaction were set with a molar ratio of $H_2$: $CO_2$: $N_2$ as 16:4:2, once the gas flow was stabilized, the reactor temperature was increased at a rate of 10℃/min. Thirdly, when the temperature reached 400℃, the catalytic activity of the $CO_2$ methanation was performed and monitored by online GC gas analysis.


Figure 3.7 The fixed-bed reactor for catalytic tests.

GC technique is commonly employed in the field of analytical chemistry for the separation and analysis of compounds that can be vaporized without undergoing decomposition. GC relies on the separation of compounds based on their vaporization and interaction with a stationary phase inside a separation column. The sample is injected into the instrument and introduced into a gas stream (commonly helium), which serves as the carrier gas. The sample components travel through the column at different rates, depending on their interaction with the stationary phase, resulting in separation. The GC instrument typically includes detectors such as the Flame Ionization Detector (FID) and Thermal Conductivity Detector (TCD). FID is sensitive to organic compounds and its response is proportional to their molecular weight. TCD, on the other hand, detects both organic and inorganic samples based on variations in thermal conductivity between components and the carrier gas.

GC test process is described as follows: Connect the air bag to the [Inlet] port, gradually apply pressure to the air bag, and observe a steady bubbling of the air outlet tube in the beaker. Then, initiate [Start] on the chromatograph, maintain a constant speed while pressing the air bag, listen for an audible indication of sample injection, and continue pressing the air bag at a consistent rate for 3-5 seconds. After the completion of sample

injection, remove the air bag and await the generation of the gas analysis report. Figure 3.5 shows the GC equipment used in this study. These tests were conducted on FULI INSTRUMENTS GC9720PLUS.


Figure 3.8 The image of GC equipment (FULI INSTRUMENTS GC9720PLUS).

These equations represent the calculation of $CO_2$ conversion ($X_{CO2}$) and methane selectivity ($S_{CH4}$) in a reaction system:

$$X_{CO_2} = \frac{V_{in} \times F_{in,CO_2} - V_{out} \times F_{out,CO_2}}{V_{in} \times F_{in,CO_2}} \times 100\% \quad \text{(eq.3.1)}$$

$$S_{CH_4} = \frac{V_{out} \times F_{out,CH_4}}{V_{in} \times F_{in,CO_2} - V_{out} \times F_{out,CO_2}} \times 100\% \quad \text{(eq.3.2)}$$

Where $V_{in}$ (mL/min) represents the volumetric flow rate at the inlet, $F_{in,\ CO2}$ (%) represents the $CO_2$ fraction in inlet, $V_{out}$ (mL/min) represents the outlet flowrate, $F_{out,\ CO2}$ (%) represents the $CO_2$ fraction in outlet.

# 4. Results and discussions

## 4.1 Effect of TPAOH usage on conventional Silicalite-1 synthesis

As TPAOH is expensive and not environmentally friendly, efforts have been made to reduce the usage of TPAOH as the template for Silicalite-1 synthesis. In this study, a typical Silicalite-1 synthesis recipe was used as the reference (considering as 100% TPAOH) and effects of reduced amounts of TPAOH (75% TPAOH and 50% TPAOH) on Silicalite-1 synthesis were investigated. The XRD patterns of the products synthesised with various amounts of TPAOH are shown in Figure 4.1 (a), showing the characteristic peaks of the MFI structure at $2\theta \approx 8.1$, 8.9, 23.1, 24, and 24.5°. These peaks indicate the successful synthesis of Silicalite-1 with both the referenced and reduced usage of TPAOH [113].

Figure 4.1 (b) illustrates the effect of TPAOH usage on the yield and crystallinity of synthesised Silicalite-1 zeolites. Relative crystallinity was determined based on the characteristic peaks at 23.1, 24 and 24.5° [114]. The sample with the highest peak area was considered as the reference for crystallinity comparison, and its relative crystallinity was set at 100%. Notably, compared to the case of 100% TPAOH usage, a significant enhancement was observed in both yield (44% for 100% TPAOH usage and 78% for 75% TPAOH usage) and relative crystallinity (72% for 100% TPAOH usage and 81% for 75% TPAOH usage) when the TPAOH usage was reduced to 75%. This observation suggests the overdose of TPAOH can hinder the synthesis of Silicalite-1. The synthesis of Silicalite-1 mainly consist of two processes: nucleation and crystallisation. The excessive amount of TPAOH promoted the formation of nucleus due to supersaturation and increased the usage of silicon source for nucleation, which led to less silicon source available for the further crystallisation [115]. Meanwhile, the high TPAOH content may partially dissolve the formed Silicalite-1 zeolites due to its high alkalinity, which may also hinder the formation of zeolites.

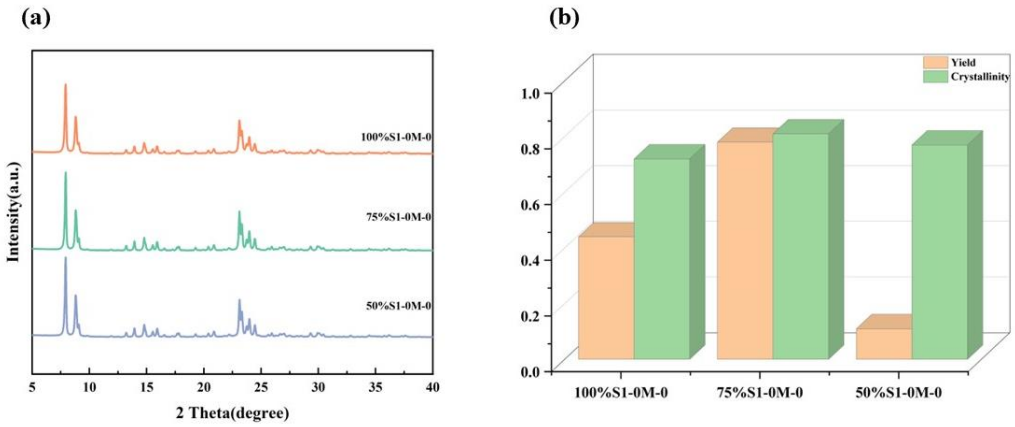


Figure 4.1 (a) XRD patterns and (b) yield and relative crystallinity of the products synthesised with different usage of TPAOH (The error of yield and crystallinity was 5.6% and 3.5%).

However, further reduction of TPAOH usage from 100% to 50% resulted in the decreased yield from 44% to 11%, while the relative crystallinity slightly increased from 72% to 77%. When the amount of TPAOH was reduced to 50%, the low concentrations of $TPA^+$ weakened the guiding effect of TPAOH and resulted in less formation of zeolite crystal nucleus, resulting in a lower yield of Silicalite-1.

Figure 4.2 shows the SEM images of the obtained Silicalite-1 zeolites, which exhibited spherical morphology with loose aggregations. The average crystal sizes of 75%S1-0M-0 and 50%S1-0M-0 samples were about 149 and 146 nm respectively, while the average crystal size of 100%S1-0M-0 sample was approximately 115 nm. The overuse of TPAOH led to the decrease in crystal size, further confirming that large amount of crystal nucleus was produced when excessive TPAOH was present, which consumed high quantity of silicon source and leaded to the hindered growth of the crystals as less silicon source was left in the synthesis solution.

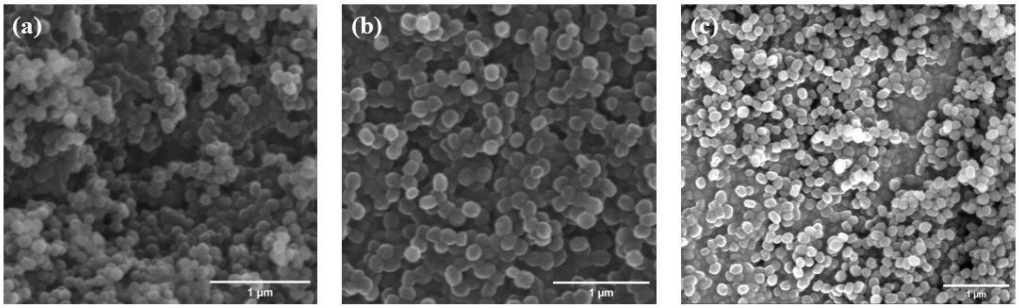


Figure 4.2 SEM images of (a) 100%S1-0M-0;(b) 75%S1-0M-0;(c) 50%S1-0M-0.

The $N_2$ adsorption-desorption isotherms and the micropore pore size distributions of these samples are depicted in Figure 4.3. All samples presented the type IV isotherms with associated H2-type hysteresis loops occurring at a relative pressure around 0.9, implying the existence of mesoporous structures [87]. The micropore distributions using the DFT model demonstrated that micropores (pore sizes were around 0.6 nm) were predominantly in these samples.

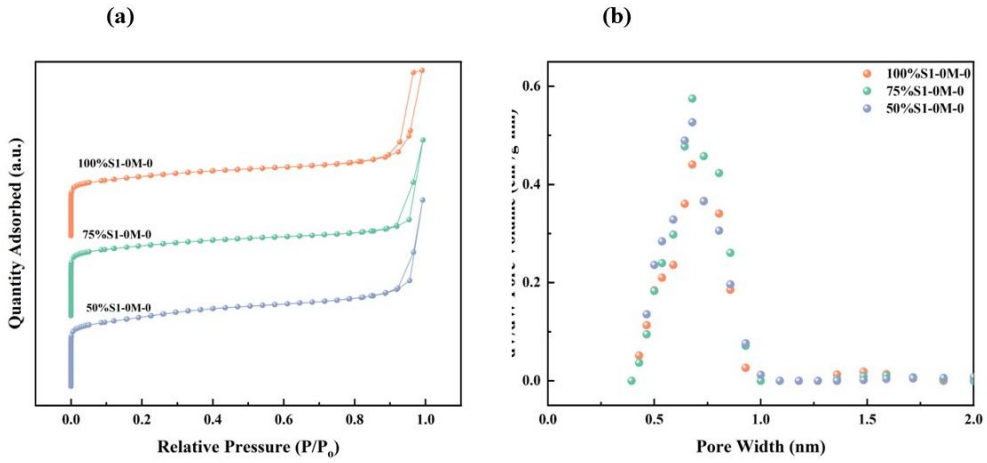


Figure 4.3 (a) $N_2$ adsorption-desorption isotherms and (b) micropore size distributions of the solid products synthesised with different usage of TPAOH.

The textural properties of the aforementioned samples are summarized in Table 4.1. When 75% and 50% TPAOH were used, both specific surface areas (463 $m^2/g$ for

75%S1-0M-0 and 475 $m^2/g$ for 50%S1-0M-0) and pore volumes (0.58 $cm^3/g$ for 75%S1-0M-0 and 0.61 $cm^3/g$ for 50%S1-0M-0) increased compared to the case with 100% TPAOH ($S_{BET}$=401 $m^2/g$ and $V_{total}$=0.543 $cm^3/g$), indicating the hindering effect of excessive TPAOH in the synthesis solution, which was consistent with the results in terms of yield, crystal structure and morphology.

Table 4.1 Textural properties of Silicalite-1 synthesised with different usage of TPAOH.

| Sample | Surface Area ($m^2/g$) | | Pore Volume ($cm^3/g$) | |
|---|---|---|---|---|
| | $S_{total}$ | $S_{micro}$ | $V_{total}$ | $V_{micro}$ |
| 100%S1-0M-0 | 401 | 232 | 0.54 | 0.12 |
| 75%S1-0M-0 | 463 | 302 | 0.58 | 0.17 |
| 50%S1-0M-0 | 475 | 234 | 0.61 | 0.13 |

### 4.2 Effect of •OH on Silicalite-1 synthesis

Recently, Yu's group has found that •OH can participate in the depolymerisation and condensation of silicate during the crystallisation process, accelerating the synthesis of Silicalite-1. The catalysis of SPS can be achieved through heating, exposure to ultraviolet radiation, and the presence of transition metals, ultimately resulting in the generation of •OH. In the depolymerisation and condensation of silicate during the crystallisation process and accelerate the synthesis of Silicalite-1 synthesis [23]. Given the ability of •OH to substitute a portion of $OH^-$ in the zeolites synthesis without increasing alkalinity, whether the usage of organic template could be reduced with the addition of •OH was investigated in this study.

Figure 4.4 (a) shows the XRD patterns of the obtained solid products synthesised with various amounts of TPAOH in the presence of •OH and the characteristic peaks of MFI-type structure were observed in all samples. Figure 4.4 (b) illustrates the effect of TPAOH usage in the Silicalite-1 synthesised with the presence of •OH on the yield and crystallinity of the obtained Silicalite-1 zeolites. When 100% TPAOH was used, the Silicalite-1 yield remarkably increased from 44% to 69%, while maintaining

comparable relative crystallinity (72% *vs.* 75%) in the presence of 0.02 M of SPS. When the TPAOH usage was reduced to 75%, the enhancement in the yield with the presence of •OH was insignificant (78% *vs.* 82%) as well as the relative crystallinity (78% *vs.* 74%). When the TPAOH usage was further reduced to 50%, the presence of •OH leaded to a twofold increase in the yield (11% *vs.* 23%), while significant increase on the crystallinity was observed as well (77% *vs*. 87%).

Silicalite-1 zeolites are usually hydrothermally synthesised in basic media, where $OH^-$ can catalyse the Si-O-Si bonds cleavage to depolymerize the silicate gel as well as catalyse the Si-O-Si bonds reassembly to polymerize the silicate anions around the hydrated cation. Compared to $OH^-$, •OH species are more effective to catalyse Si-O-Si bonds dissociation and re-formation [24]. In this study, when insufficient TPAOH (50% TPAOH) was used for the synthesis of Silicalite-1, the presence of •OH promoted the breakage and re-formation of Si-O-Si bonds, thus increasing the utility of TPAOH and resulting in a higher yield of Silicalite-1. When excessive TPAOH (100% TPAOH) was in the synthesis solution, the presence of •OH increased the yield of Silicalite-1 due to the lower selectivity in Si-O-Si breaking and remaking via •OH for Silicalite-1 nucleation. Namely when excessive TPAOH was presented in the synthesis solution, though more Si-O-Si bonds were broken in the presence of •OH and $OH^-$ species, some of them were unable to attached to $TPA^+$ cations for nucleation. As a consequence, there were more silicon species available for the crystallisation process, resulting in a higher yield of Silicalite-1 compared to the case with excessive $OH^-$ species alone. In conclusion, the presence of •OH in the synthesis solution was able to enhance the yield of Silicalite-1 with comparable crystallinity, especially when the TPAOH content was insufficient or excessive.

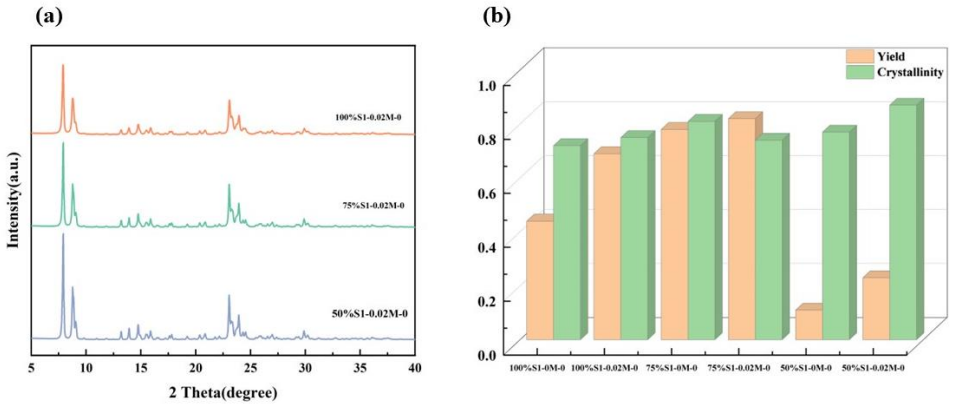


Figure 4.4 (a) XRD patterns and (b) yield and relative crystallinity of the solid products synthesised in the absence and presence of •OH with different usage of TPAOH (The error of yield and crystallinity was 5.6% and 3.5%).

The $N_2$ adsorption-desorption isotherms and micropore pore size distributions of these samples are depicted in Figure 4.5, and all the samples showed that the predominant size of micropores was around 0.6 nm, which was comparable to the pore size of typical Silicalite-1 zeolites (~0.55 nm). 75%S1-0.02M-0 and 50%S1-0.02M-0 presented the type IV isotherms with H4-type hysteresis loops occurring at relative pressure around 0.2. This type of hysteresis loops is linked to the transition of $N_2$ from a localized fluid-like phase to a crystalline-like solid phase, which is specific to MFI-type zeolites and often results in apparent mesopores with a size of 2 nm due to the interaction between $N_2$ quadrupolar moment and the MFI framework, thus cannot indicate any real mesopority [116-118]. From another perspective, hysteresis loops occurring at relative pressure around 0.2 are usually observed in high-quality crystals, suggesting that Silicalite-1 zeolites with high crystallinity were successfully synthesised with the presence of •OH, which was consistent with the XRD results [118]. All samples presented H2 type hysteresis loops- occurring at relative pressure around 0.9 (less significant for 75%S1-0.02M-0 and 50%S1-0.02M-0) and this type of hysteresis loops is typical for capillary condensation in mesopores [119]. The presence of a significant uptake of $N_2$ observed in adsorption, combined with the occurrence of hysteresis, unequivocally

confirmed the existence of a certain amount of mesopores in these samples.

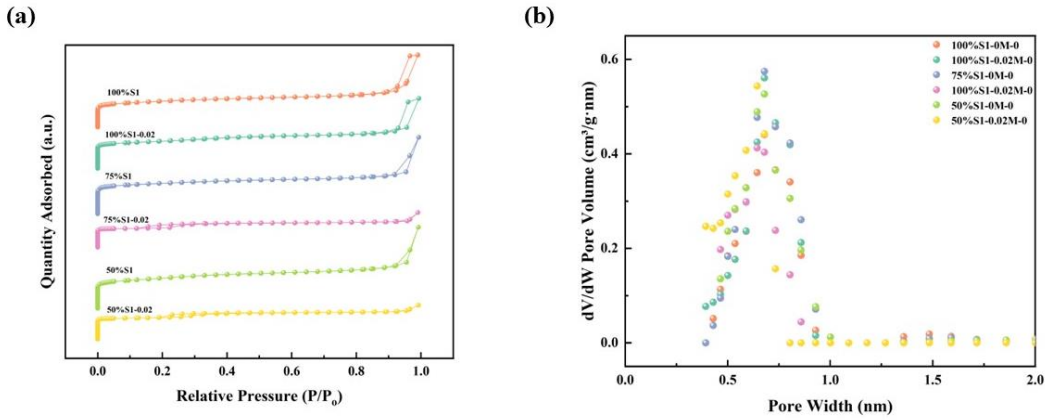


Figure 4.5 (a) $N_2$ adsorption-desorption isotherms and (b) micropore size distributions of the solid products synthesised in the absence and presence of •OH with different usage of TPAOH.

The textural properties of the aforementioned samples are summarized in Table 4.2. When 75% or 50% TPAOH was used for synthesis, the produced Silicalite-1 zeolites had lower specific surface areas (347 $m^2/g$ for 75% TPAOH and 343 $m^2/g$ for 50% TPAOH) and pore volumes (0.27 $cm^3/g$ for 75% TPAOH and 0.26 $cm^3/g$ for 50% TPAOH) compared to the case with 100% TPAOH (specific surface area of 401 $m^2/g$ and pore volume of 0.54 $cm^3/g$). In the case of 100%TPAOH usage, the presence of •OH insignificantly affected both specific surface area and pore volume. Therefore, the specific surface areas and pore volumes of Silicalite-1 zeolites mainly depended on the usage of TPAOH. Though the presence of •OH was able to increase the yield of Silicalite-1 zeolites when less TPAOH was present, it was less effective on creating pores compared to TPAOH.

Table 4.2 Textural properties of Silicalite-1 synthesised with different usage of TPAOH.

| Sample | Surface Area ($m^2/g$) | | Pore Volume ($cm^3/g$) | |
|---|---|---|---|---|
| | $S_{total}$ | $S_{micro}$ | $V_{total}$ | $V_{micro}$ |
| 100%S1-0M-0 | 401 | 232 | 0.54 | 0.12 |
| 100% S1-0.02M-0 | 422 | 249 | 0.53 | 0.14 |
| 75% S1-0.02M-0 | 347 | 121 | 0.27 | 0.06 |
| 50% S1-0.02M-0 | 343 | 231 | 0.26 | 0.12 |

## 4.3 Effect of CNCs and •OH on Silicalite-1 synthesis

CNCs can serve as suitable auxiliary species or secondary templates in zeolites synthesis, while the presence of $OH^-$ in the aluminosilicate gel can accelerate the cleavage of hydrogen bonds in CNCs and intensity the nucleation process [25,26,120,121]. As highly active •OH species can act as $OH^-$ in the depolymerisation and condensation of silicate and accelerate the synthesis of Silicalite-1 [23], whether •OH can also act as $OH^-$ to break hydrogen bonding in CNCs to further promote Silicalite-1 synthesis with different amounts of TPAOH was investigated in this study.

### 4.3.1 100% TPAOH

Figure 4.6 (a) shows the XRD patterns of the resultant Silicalite-1 zeolites synthesised with 100% TPAOH and the characteristic peaks of MFI-type structure were observed in all samples. When CNCs alone were added in the synthesis solution, the yield and relative crystallinity of Silicalite-1 were 62% and 77%, which were higher than the case when CNCs and •OH were absence (44% for yield and 72% for crystallinity). The promoting effect was related to the abundance of hydroxyl groups in CNCs, which can interact with silicon species, serving as the favourite sites for zeolite nucleation [26]. The incorporation of •OH and CNCs further improved the yield to 71% with a high relative crystallinity (79%) of Silicalite-1 zeolites, as presented in Figure 4.6 (b). However, when only •OH was present, the yield and crystallinity were comparable with the case that both •OH and CNCs were present, which indicated that the promoting effect of

CNCs on the synthesis of Silicalite-1 was insignificant when •OH was present with 100% TPAOH.

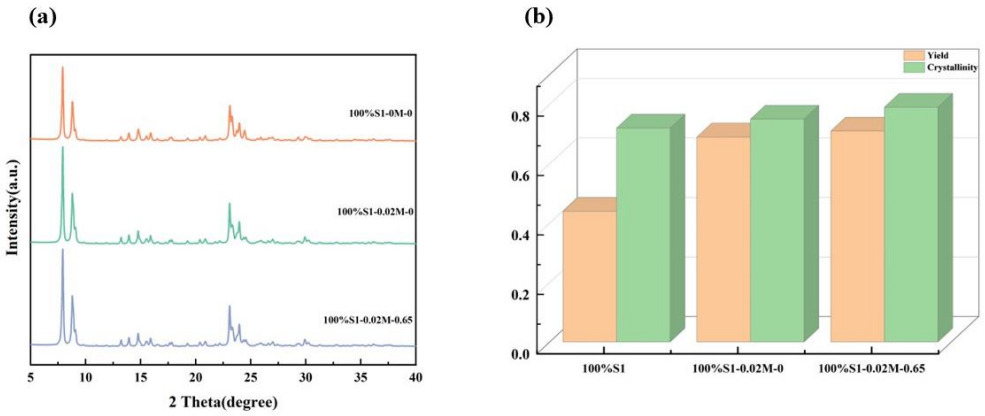


Figure 4.6 (a) XRD patterns and (b) yield and relative crystallinity of Silicalite-1 synthesised in the absence and presence of CNCs and •OH when100% TPAOH was present (The errors of yield and relative crystallinity were 5.6% and 3.5%).

The $N_2$ adsorption-desorption isotherm of sample 100%S1-0.02M-0.65 is shown in Figure 4.7. Silicalite-1 synthesised in the presence of •OH and CNCs with 100% TPAOH exhibited a H2-type hysteresis loop at a relative pressure of approximately 0.9, along with the presence of hysteresis loops at a relative pressure around 0.2. This sample exhibited a steep uptake of $N_2$ at relatively low pressure, which was associated with the filling of $N_2$ within the narrow micropores [113]. This indicates that the original micropore structure remained after the utilisation of •OH and CNCs. The hysteresis between adsorption and desorption is typical for capillary condensation in mesopores [119].

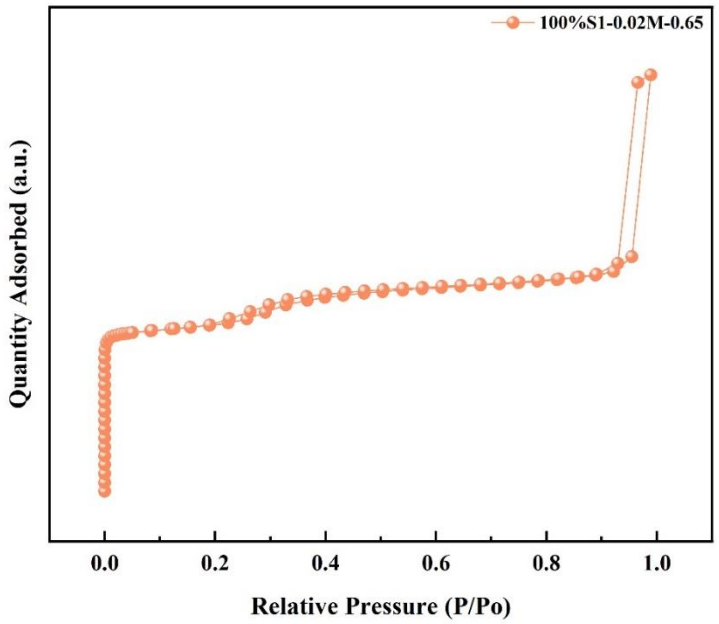


Figure 4.7 $N_2$ adsorption-desorption isotherms of the solid product with the presence of CNCs and •OH when 100% TPAOH was present.

More textural properties of the obtained Silicalite-1 zeolites are presented in Table 4.3 and Table S1. The addition of CNCs alone had insignificant effect on specific surface area compared to the case in the absence of •OH and CNCs (422 $cm^2/g$ for 100%S1-0.02M-0 and 401 $m^2/g$ for 100%S1-0M-0), while the presence of •OH alone slightly increased the specific surface area (456 $cm^2/g$ for 0.65-CNCs-100%S1-0M-0). However, the presence of both CNCs and •OH with 100% TPAOH led to the remarkable decrease in surface area (303 $cm^2/g$ for 0.65-CNCs-100%S1-0.02M-0). Similar rules were observed regarding pore volume.

This can be speculated as follows: When sufficient TPAOH was present in the synthesis solution, 1) the presence of •OH alone stimulated the cleavage of Si-O-Si bonds and promoted the utilisation of $TPA^+$ template, resulting in the increased yield of Silicalite-1. As there were no other templates in the synthesis solution, the pore structure changed insignificantly; 2) the presence of CNCs alone acted as another template and provided more nucleation sites for synthesis, leading to the increase in yield and slight

enhancement in surface areas; 3) the presence of both •OH and CNCs stimulated the cleavage of bonds in CNCs by •OH (•OH might favour the cleavage of bonds in CNCs than Si-O-Si cleavage) and produced smaller molecules which were less effective for pores generation, resulting in significant decrease in surface area.

Table 4.3 Textural properties of Silicalite-1 synthesised when 100% TPAOH was present.

| Sample | Surface Area ($m^2/g$) | | Pore Volume ($cm^3/g$) | |
|---|---|---|---|---|
| | $S_{meso}$ | $S_{total}$ | $V_{meso}$ | $V_{total}$ |
| 100%S1-0M-0 | 169 | 401 | 0.42 | 0.54 |
| 100%S1-0.02M-0.65 | 103 | 303 | 0.26 | 0.36 |

The pore distributions for the aforementioned samples are depicted in Figure S3, and the micropore distributions using the DFT model demonstrated that the micropores of these Silicalite-1 zeolites were predominantly centred at around 0.6 nm. The results were consistent with the sample 100%S1-0M-0, indicating that the addition of •OH and CNCs had insignificant effects on pore distributions.

### 4.3.2 75% TPAOH

To investigate whether the co-presence of •OH and CNCs was able to promote Silicalite-1 synthesis with less organic templates, the usage of TPAOH was reduced to 75%. Figure 4.8 (a) shows the XRD patterns of the resultant Silicalite-1 zeolites synthesised with •OH and different amounts of CNCs in the presence of 75% TPAOH, and the characteristic peaks of MFI-type structure were observed in all samples. When only •OH or CNCs (0.65 wt%) was added in the synthesis solution, the yield increased insignificantly (81% for CNCs alone and 82% for •OH alone, while 78% for the absence of both CNCs and •OH) and the relative crystallinity was slightly reduced (73% for CNCs alone and 74% for •OH alone, while 81% for the absence of both •OH and CNCs).

The reduced crystallinity may be attributed to the accelerated cleavage of Si-O-Si bonds and reformation crystallisation process via •OH, which led to some rapid

polymerisation of the silicon source to form amorphous when TPAOH was insufficient, resulting in decreased crystallinity. When only CNCs were present with 75% TPAOH, the crystallinity decreased because CNCs were less effective working as the template compared to TPAOH.

Interestingly, when both CNCs and •OH were present in the synthesis solution, the yield and crystallinity of the obtained Silicalite-1 were generally increased (as shown in Figure 4.8 (b), demonstrating the promoting effect of the presence of both •OH and CNCs on silicalite-1 synthesis. When both •OH and CNCs were present, some •OH species stimulated the crystallisation process, while some •OH species reacted with CNCs. Consequently, the polymerization of silicon source was less likely to occur, resulting in higher yield of Silicalite-1 zeolites with high crystallinity.

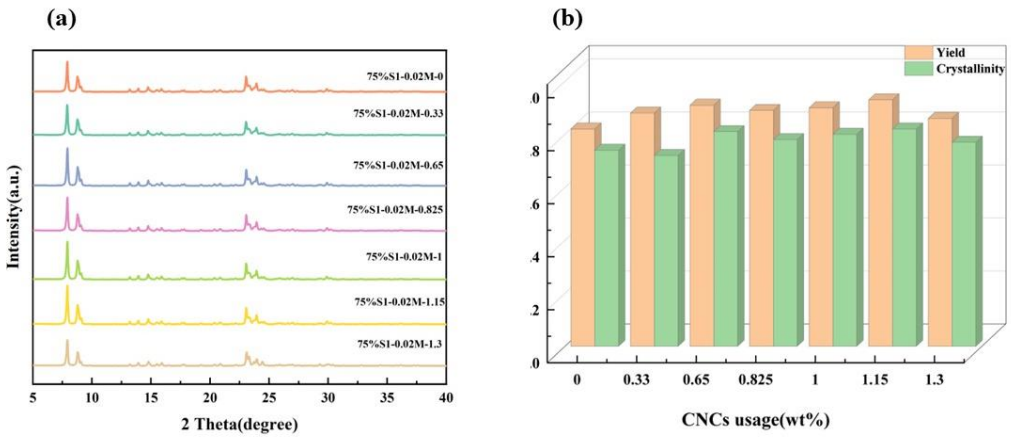


Figure 4.8 (a) XRD patterns and (b) yields and crystallinities of the solid products synthesised with the presence of •OH and CNCs when 75% TPAOH was present (The errors of the yields and crystallinities were 5.6% and 3.5%).

The $N_2$ adsorption-desorption isotherms and micropore size distribution of these samples are depicted in Figure 4.9. All these samples presented the type IV isotherm with an H4-type hysteresis loop occurring at a relative pressure around 0.2 and H2-type hysteresis loop occurring at a relative pressure around 0.9. The presence of a significant

uptake observed in adsorption, combined with the occurrence of hysteresis at relative pressure around 0.9, suggested the presence of mesopores. The DFT model was employed to analyse the micropore distribution, revealing that the micropores of these Silicalite-1 zeolites were predominantly centred at around 0.6 nm.

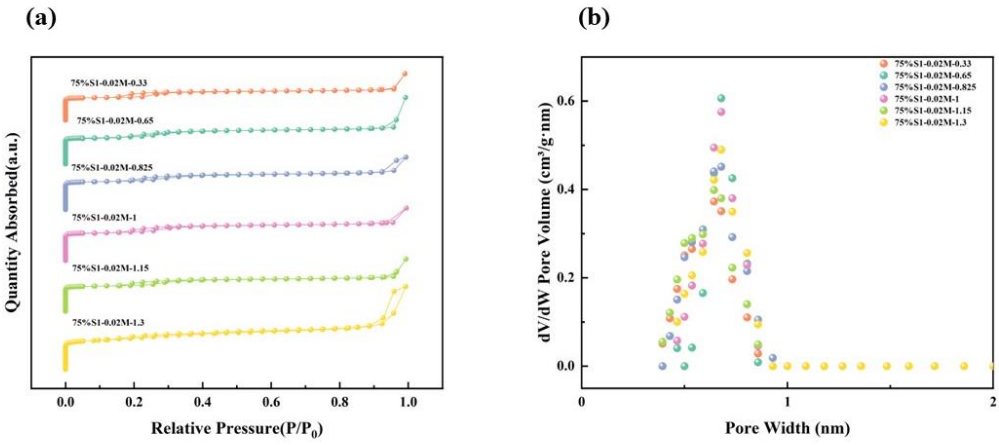


Figure 4.9 (a) $N_2$ adsorption-desorption isotherms and (b) micropore size distributions of the solid products synthesised with the presence of •OH and CNCs when 75%TPAOH was present.

More textural properties of the obtained Silicalite-1 zeolites are listed in Table 4.4. The addition of CNCs alone had an insignificant effect on specific surface areas (447 $m^2/g$ *vs.* 463 $m^2/g$) and pore volumes (0.57 $cm^3/g$ *vs.* 0.58 $cm^3/g$) compared to the case in the absence of •OH and CNCs. However, the presence of •OH alone led to a decrease in both specific surface area and pore volume. Furthermore, in the presence of both CNCs and •OH, similar reductions in specific surfaces area and pore volumes were observed compared to the case where neither •OH nor CNCs were present.

Table 4.4 Textural properties of Silicalite-1 synthesised with the presence of •OH and CNCs when 75%TPAOH was present.

| Sample | Surface Area ($m^2/g$) | | Pore Volume ($cm^3/g$) | |
|---|---|---|---|---|
| | $S_{total}$ | $S_{micro}$ | $V_{total}$ | $V_{micro}$ |
| 75%S1-0M-0 | 463 | 302 | 0.58 | 0.17 |
| 75%S1-0.02M-0 | 347 | 121 | 0.27 | 0.06 |
| 75%S1-0.02M-0.33 | 292 | 122 | 0.26 | 0.07 |
| 75%S1-0.02M-0.65 | 325 | 146 | 0.36 | 0.09 |
| 75%S1-0.02M-0.825 | 334 | 181 | 0.34 | 0.10 |
| 75%S1-0.02M-1 | 333 | 241 | 0.29 | 0.12 |
| 75%S1-0.02M-1.15 | 307 | 181 | 0.29 | 0.10 |
| 75%S1-0.02M-1.3 | 359 | 184 | 0.45 | 0.10 |

This can be speculated as follows: When 75% TPAOH was present in the synthesis solution, 1) the presence of •OH alone stimulated the cleavage and reformation of Si-O-Si bonds, which may have caused some rapid polymerisation of silicon source to form amorphous, leading to the decrease of specific surface area; 2) the presence of both •OH and CNCs stimulated the cleavage of bonds in CNCs by •OH and produced smaller molecules that were less effective for pore generation, resulting in a significant decrease in specific surface area.

### 4.3.3 50% TPAOH

It has been demonstrated that Silicalite-1 was successfully synthesised with 75% TPAOH usage. The presence of •OH alone stimulated the cleavage and reformation of Si-O-Si bonds while possibly causing the rapid polymerisation of silicon source, resulting in high Silicalite-1 production with high crystallinity. However, the specific surface area of the obtained Silicalite-1 was reduced to some extent. As CNCs can be used as a zeolites synthesis templates and hinder the rapid polymerisation of silicon source caused by •OH, further reduced organic template usage to 50% was applied for Silicalite-1 synthesis. Additionally, the effect of CNCs usage at different •OH contents

(via using different amounts of SPS) on Silicalite-1 synthesis was investigated to promote the synergic effect of CNCs and •OH on zeolites synthesis with reduced organic template.

#### 4.3.3.1 No SPS

When TPAOH was sufficient (100% and 75%), the presence of CNCs alone could increase in yield and slight enhancement in surface areas of Silicalite-1. We further reduced the amount of TPAOH to 50% and added different amounts of CNCs separately to explore their effects on the synthesis of Silicalite-1.

Figure 4.10 (a) shows the XRD patterns of the resultant Silicalite-1 zeolites synthesised with different amounts of CNCs in the absence of •OH, and the characteristic peaks of MFI-type structure were observed in all these samples. The yield and crystallinity of these Silicalite-1 zeolites were generally increased, as presented in Figure 4.10 (b). When TPAOH was intensively insufficient in the synthesis system, CNCs acted as another template and provided more nucleation sites for the synthesis, leading to increased yield [26]. However, with increased CNCs usage to above 1.15 wt% (namely 1.3 wt%), the Silicalite-1 yield began to decrease, which was due to the aggregation of CNCs. When 50% TPAOH was used, the CNCs usage of 1.15 wt% led to highest Silicalite-1 yield (53%), which was more than four times of the yield when no CNCs were present (11%) and higher than the yield of Silicalite-1 synthesised with 100%TPAOH (44%).

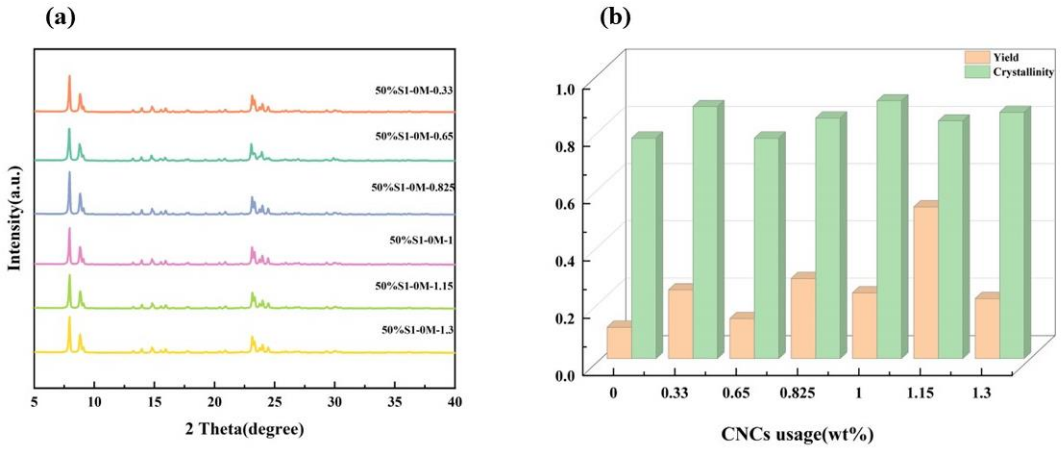


Figure 4.10 (a) XRD patterns and (b) yields and crystallinities of the solid products synthesised with the presence of CNCs when no •OH was present (The errors of the yields and crystallinities were 5.6% and 3.5%).

The $N_2$ adsorption-desorption isotherms and micropore size distribution of these samples are depicted in Figure 4.11. All these samples presented the type IV isotherm with an H2-type hysteresis loop occurring at a relative pressure around 0.9, indicating the presence of mesopores. The micropore distributions using the DFT model demonstrated that the predominant size of micropores was around 0.6 nm, which was consistent with the sample 50%S1-0M-0, indicating that the addition of CNCs had insignificant on pore size distributions.

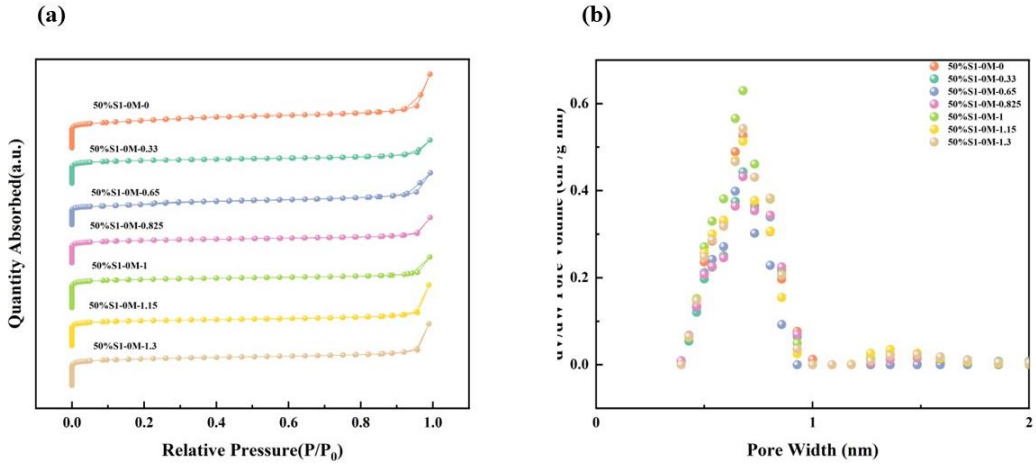


Figure 4.11 (a) $N_2$ adsorption-desorption isotherms and (b) micropore size distributions of the

solid products synthesised with the presence of CNCs when no •OH was present.

More textural properties of the obtained Silicalite-1 zeolites are presented in Table 4.5. The presence of CNCs with 50% TPAOH led to a reduction in specific surface areas and pore volumes compared to the sample 50%S1-0M-0(specific surface area of 475 $m^2/g$ and pore volume of 0.61 $cm^3/g$). However, with increased CNCs usage, specific surface areas and pore volumes generally increased. This observation can be attributed to the presence of CNCs not only providing more nucleation sites but also acting as a template for Silicalite-1 synthesis. Therefore, the gradual increase in the CNCs usage enabled a greater utilisation of CNCs as templates, enhancing specific surface areas and pore volumes. The highest specific surface area (404 $m^2/g$) was achieved when the CNCs usage was 0.825 wt%.

Table 4.5 Textural properties of Silicalite-1 synthesised under 50%TPAOH with the presence of CNCs.

| Sample | Surface Area ($m^2/g$) | | Pore Volume ($cm^3/g$) | |
|---|---|---|---|---|
| | $S_{total}$ | $S_{micro}$ | $V_{total}$ | $V_{micro}$ |
| 50% S1-0M-0 | 475 | 234 | 0.61 | 0.13 |
| 50% S1-0M-0.33 | 375 | 278 | 0.36 | 0.21 |
| 50% S1-0M-0.65 | 401 | 294 | 0.40 | 0.16 |
| 50% S1-0M-0.825 | 371 | 268 | 0.38 | 0.15 |
| 50% S1-0M-1 | 395 | 302 | 0.34 | 0.16 |
| 50% S1-0M-1.15 | 404 | 310 | 0.50 | 0.17 |
| 50% S1-0M-1.3 | 437 | 319 | 0.51 | 0.17 |

#### 4.3.3.2 0.01 M SPS

The addition of 0.01 M SPS led to higher yield (40% *vs.* 11%) and higher relative crystallinity (94% *vs.* 77%) compared to the case when CNCs and •OH were absent. This could be attributed to the presence of •OH, which stimulated the cleavage of Si-O-Si bonds and promoted the process of crystallisation, resulting in the increased yield of Silicalite-1. Figure 4.12 (a) shows the XRD patterns of the resultant Silicalite-1

zeolites synthesised with 0.01 M SPS usage, and the diffraction peaks were consistent with the characteristic peaks of MFI-type structure. Figure 4.12 (b) illustrates the variations in yield and crystallinity of Silicalite-1 zeolites synthesised with different amount of CNCs. When CNCs were added in the presence of •OH, the yield and crystallinity increased first and then generally decreased compared to the case when •OH alone was present. The addition of 0.33 wt% CNCs with 0.01 M SPS obtained the highest yield of Silicalite-1 with high relative crystallinity (58% and 90%). When •OH and CNCs were present in the synthesis system simultaneously with insufficient TPAOH usage, a portion of •OH facilitated the crystallisation process, while another portion reacted with CNCs to generate additional nucleation sites. This intergradation accelerated the crystallisation process, thus increasing the yield of Silicalite-1. However, as •OH was more effective for bonds cleavage in CNCs than breaking Si-O-Si bonds, when the CNCs usage was high (>0.33 wt% in this study), more •OH was used to break the hydrogen bonds in CNCs, making less •OH available for Si-O-Si bonds breakage and reform, resulting in decreased yields.

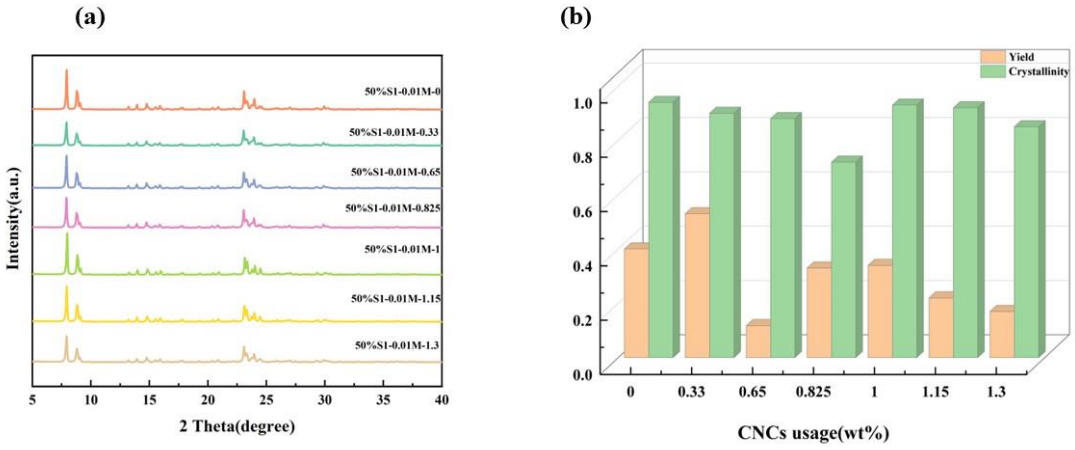


Figure 4.12 (a) XRD patterns and (b) yield and relative crystallinity of the solid products synthesised with the presence of 0.01 M SPS and CNCs when 50% TPAOH was present. (The errors of yield and relative crystallinity were 5.6% and 3.5%).

The $N_2$ adsorption-desorption isotherms and micropore pore size distributions of these

samples are depicted in Figure 4.13. All these samples presented the type IV isotherm with H2-type hysteresis loop occurring at a relative pressure around 0.9, which was related to the existence of mesopores. Notably, when the amount of CNCs were less than 1 wt%, H4-type hysteresis loop was observed at a relative pressure around 0.15, which can be attributed to the transition of $N_2$ from fluid-like phase to crystalline-like phase. And all the samples showed that the predominant size of micropores was around 0.6 nm, which was comparable to the pore size of typical Silicalite-1 zeolites (~0.55 nm).

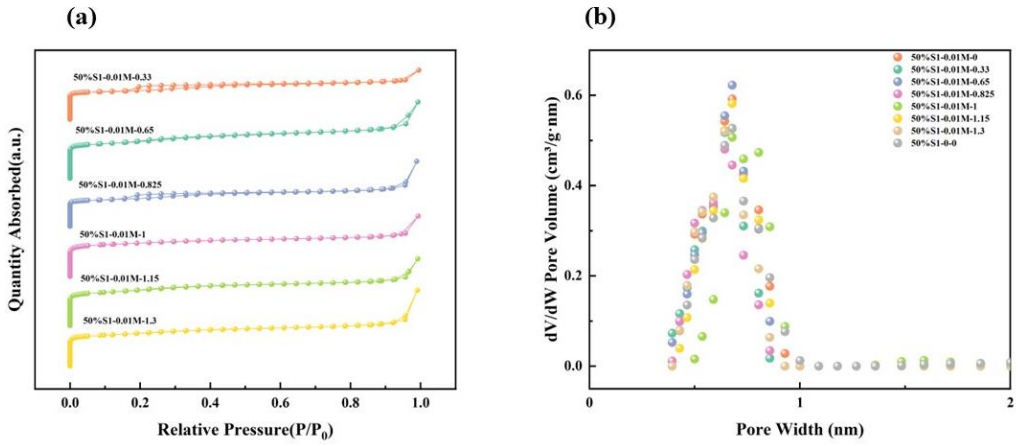


Figure 4.13 (a) $N_2$ adsorption-desorption isotherms and (b) micropore size distributions of the solid products synthesised with the presence of 0.01 M SPS and CNCs when 50% TPAOH was present.

The textural properties of the aforementioned samples are summarized in Table 4.6. The presence of •OH and CNCs resulted in decreases in both specific surface areas and pore volumes compared to the case in the absence of •OH and CNCs. However, with increasing usage of CNCs, a general increase in specific surface areas and pore volumes was observed. The presence of both •OH and CNCs stimulated the cleavage of bonds in CNCs by •OH and produced smaller molecules that were less effective for pore generation, resulting in a significant decrease in specific surface area. Notably, specific surface area and pore volume increased with increasing usage of CNCs. This can be

explained as the increased usage of CNCs led to the aggregation of CNCs, which protected some CNCs from decomposition to small molecules. And the preserved CNCs structure was able to be used as an effective template for pore generation.

Table 4.6 Textural properties of Silicalite-1 synthesised with the presence of 0.01 M SPS and CNCs when 50% TPAOH was present.

| Sample | Surface Area ($m^2/g$) | | Pore Volume ($cm^3/g$) | |
|---|---|---|---|---|
| | $S_{total}$ | $S_{micro}$ | $V_{total}$ | $V_{micro}$ |
| 50%S1-0M-0 | 475 | 234 | 0.61 | 0.13 |
| 50%S1-0.01M-0 | 446 | 311 | 0.32 | 0.17 |
| 50%S1-0.01M-0.33 | 355 | 241 | 0.29 | 0.12 |
| 50%S1-0.01M-0.65 | 460 | 250 | 0.45 | 0.13 |
| 50%S1-0.01M-0.825 | 350 | 203 | 0.39 | 0.11 |
| 50%S1-0.01M-1 | 378 | 245 | 0.37 | 0.13 |
| 50%S1-0.01M-1.15 | 437 | 238 | 0.40 | 0.13 |
| 50%S1-0.01M-1.3 | 400 | 235 | 0.45 | 0.13 |

#### 4.3.3.3 0.02 M SPS

Figure 4.14 (a) shows the XRD patterns of the resultant Silicalite-1 zeolites with 0.02 M SPS usage and the characteristic peaks of MFI-type structure were observed in all samples. Compared to the 0.01 M SPS case, increasing the •OH content in the synthesis solution without CNCs led to a decrease in yield (40% *vs.* 23%) and relative crystallinity (94% *vs.* 87%), as presented in Figure 4.14 (b). The use of 0.02 M SPS generated too much •OH in the synthesis solution (when 50% TPAOH was present), which caused the condensation of silicon source to form amorphous at the bottom of the reactor (see Figure S4). Consequently, this led to a lower yield. With increasing CNCs usage, a higher yield was observed as some •OH reacted with CNCs to generate additional nucleation sites and reduced the •OH content in the synthesis solution. When the CNCs concentration was higher than 0.825 wt%, the aggregation of CNCs became

intensive, which made less nucleation sites available for the synthesis and reduced the yield of Silicalite-1.

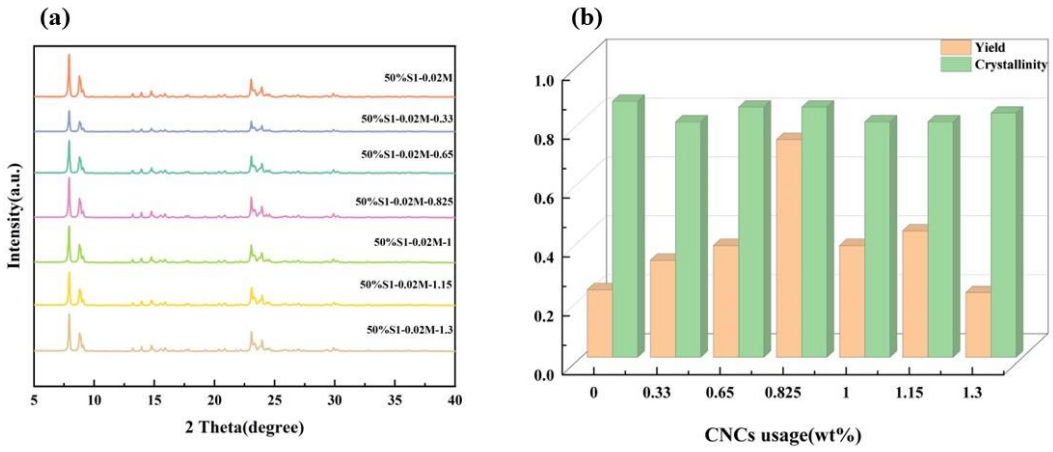


Figure 4.14 (a) XRD patterns and (b) yields and crystallinities of the solid products synthesised with the presence of 0.02 M SPS and CNCs when 50% TPAOH was present (The errors of the yields and crystallinities were 5.6% and 3.5%).

The $N_2$ adsorption-desorption isotherms and micropore size distribution of these samples are depicted in Figure 4.15. All these samples presented the type IV isotherms with H2-type hysteresis loops occurring at relative pressure around 0.9, along with the presence of H4-type hysteresis loops at relative pressure around 0.2. The micropore distributions using DFT model demonstrated that the predominant size of micropores was around 0.6 nm.

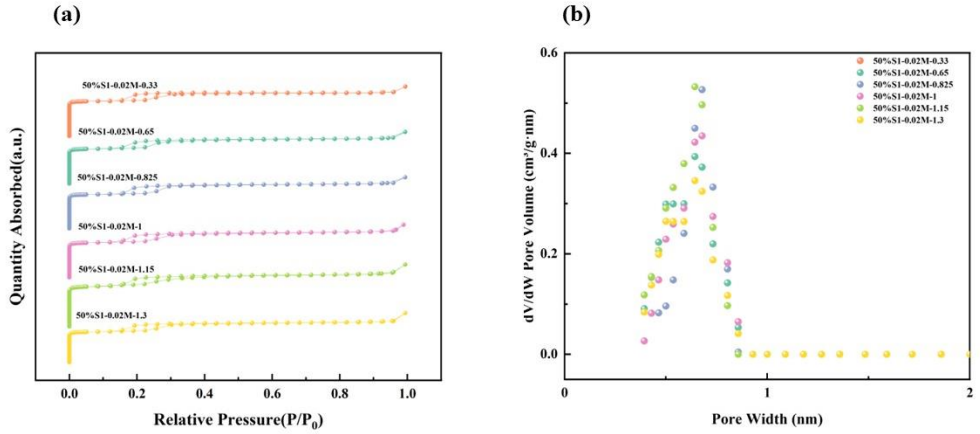


Figure 4.15 (a) $N_2$ adsorption-desorption isotherms and (b) micropore size distributions of the solid products synthesised with the presence of 0.02 M SPS and CNCs when 50% TPAOH was present.

The textural properties of the aforementioned samples were summarized in Table 4.7. The addition of 0.02 M SPS significantly reduced the specific surface areas (343 $cm^2/g$ *vs.* 446 $m^2/g$) and pore volumes (0.26 $cm^3/g$ *vs.* 0.32 $cm^3/g$) compared to the case when 0.01 M SPS was used. However, when CNCs were added to the synthesis solution, both specific surface areas and pore volumes increased first and then decreased. The highest specific surface area and pore volume were achieved when the CNCs usage was 1.15 wt%. Sever aggregation of CNCs may occur when the usage exceeded 1.15 wt%, leading to the less effective utilisation of CNCs as a template for pore generation and resulting in a significant decrease in specific surface area and pore volume.

Table 4.7 Textural properties of Silicalite-1 synthesised with the presence of 0.02 M SPS and CNCs when 50% TPAOH was present.

| Sample | Surface Area ($m^2/g$) | | Pore Volume ($cm^3/g$) | |
|---|---|---|---|---|
| | $S_{total}$ | $S_{micro}$ | $V_{total}$ | $V_{micro}$ |
| 50%S1-0M-0 | 475 | 234 | 0.61 | 0.13 |
| 50%S1-0.02M-0 | 343 | 231 | 0.26 | 0.12 |
| 50%S1-0.02M-0.33 | 317 | 219 | 0.20 | 0.11 |
| 50%S1-0.02M-0.65 | 333 | 135 | 0.21 | 0.07 |
| 50%S1-0.02M-0.825 | 321 | 141 | 0.21 | 0.07 |
| 50%S1-0.02M-1 | 318 | 215 | 0.21 | 0.10 |
| 50%S1-0.02M-1.15 | 366 | 194 | 0.25 | 0.10 |
| 50%S1-0.02M-1.3 | 276 | 188 | 0.20 | 0.09 |

Figure 4.16 shows the SEM images of the resultant Silicalite-1 zeolites with 50% TPAOH. All these samples were spherical crystals and loosely aggregated. The average crystal size of 50%S1-0M-0 was approximately 146 nm (Figure 4.16 (a)), whereas the average crystal size of 50%S1-0.02M-0.825 was around 324 nm. And the average crystal sizes of 50%S1-0.02M-0 and 50%S1-0.02M-0.825 were about 351 and 405 nm, respectively. Increased crystal size can indicate a higher crystallisation rate when identical synthesis durations are applied. Both •OH and CNCs were approved to be able to accelerate the crystallisation of Silicalite-1, and the synergic effect of •OH and CNCs promoted the crystallisation most significantly.

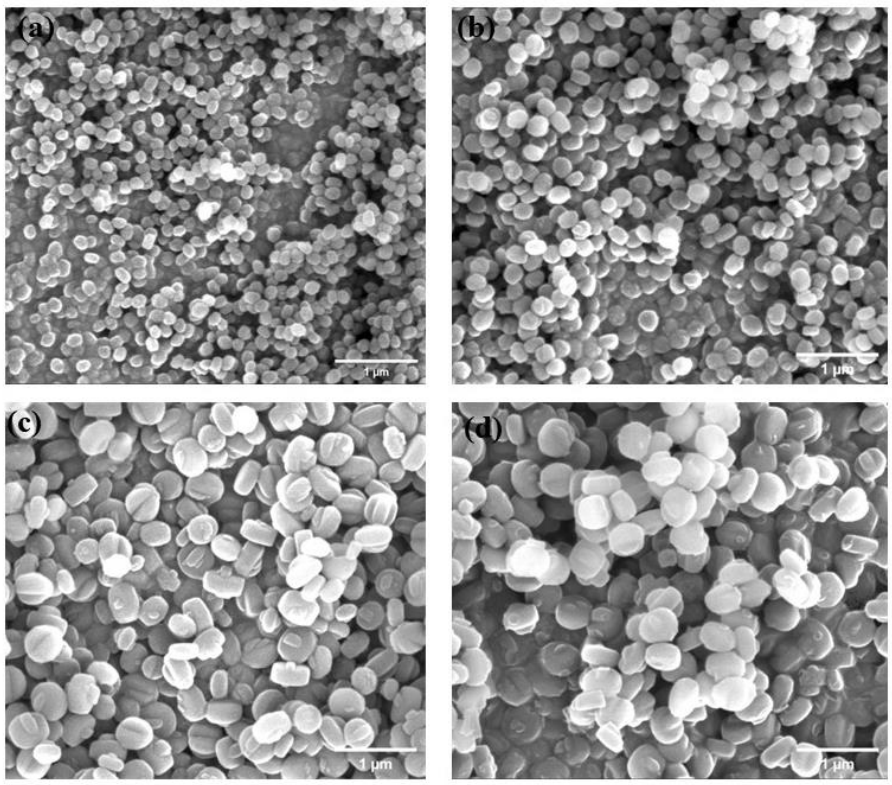


Figure 4.16 SEM images of (a) 50%S1-0M-0;(b) 50%S1-0M-0.825;(c) 50%S1-0.02M-0;(d) 50%S1-0.02M-0.825.

Figure 4.17 shows the TEM images of the resultant Silicalite-1 zeolites. Some mesopores were observed in 50%S1-0M-0 while fewer mesopores were observed when either •OH or CNCs were present.

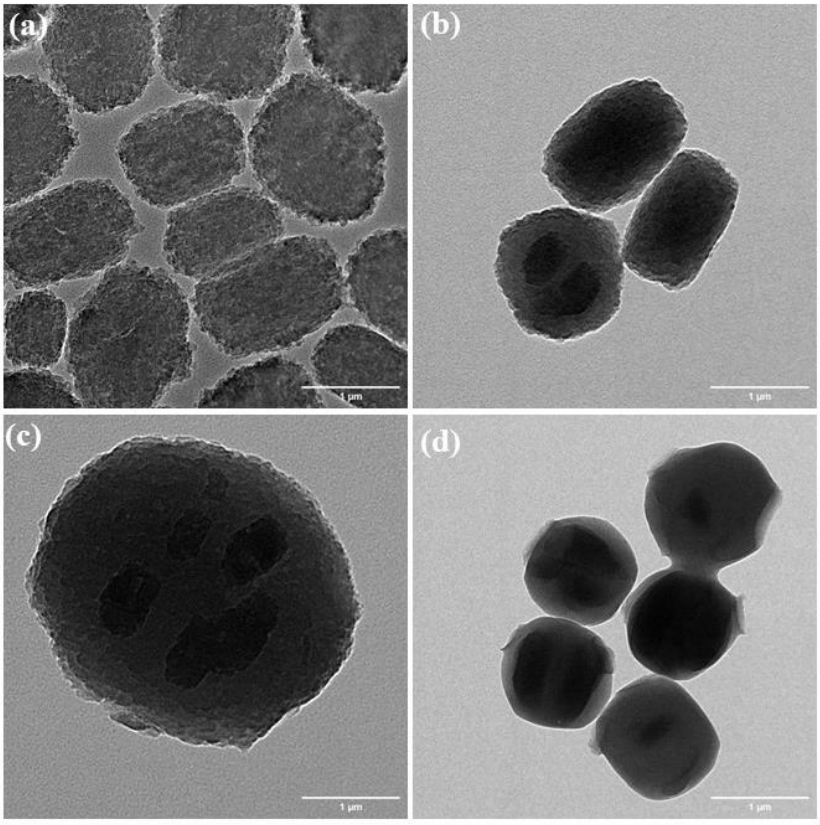


Figure 4.17 TEM images of (a) 50%S1-0M-0;(b) 50%S1-0M-0.825;(c) 50%S1-0.02M-0;(d) 50%S1-0.02M-0.825.

In conclusion, both •OH and CNCs accelerated the crystallisation of Silicalite-1. When there was an insufficient organic template (TPAOH) in the synthesis solution, the presence of •OH accelerated Si-O-Si bond break and reform, leading to increase the yield and crystallinity. The presence of CNCs provided more nucleation sites and acted as another template for Silicalite-1 synthesis, increasing the yield as well. The presence of •OH and CNCs had a synergistic effect on Silicalite-1 synthesis, further promoting Silicalite-1 production. The optimal yield (74%) and crystallinity (84%) were achieved when 0.02 M SPS and 0.825 wt% CNCs were added in the synthesis solution with 50% TPAOH usage.

# 5. Mechanism study for Silicalite-1 synthesis

To analyse the mechanism of Silicalite-1 synthesis with the presence of CNCs and •OH, FT-IR analyses of the synthesis gels with different crystallisation time were carried out. Figure 5.1 (a) and (b) show IR spectra from 1800 to 400 $cm^{-1}$ and 4000 to 1800 $cm^{-1}$, which can identify zeolite framework vibrations and surface hydroxyl groups, as summarized below:

(i) A peak at 565 $cm^{-1}$ was observed in all the spectra, which was attributed to the five-ring units within the structures of Silicalite-1[122,123]. The intensities of the peaks at around 560 $cm^{-1}$ increased slightly with prolonged synthesis time from 1h to 16h during the crystallisation. Significant increase in intensity was observed when extending the crystallisation time to 24h, which was related to the crystalline perfection. The blue-shift of the peak at 565 $cm^{-1}$ over time further confirmed the crystalline perfection, as well as indicated the growth of crystal size [124].

(ii) All the spectra showed the peaks at 1220, 1055 and 1105 $cm^{-1}$, corresponding to the external and internal asymmetric of Si–O–Si bonds. Furthermore, the peaks at 790 and 450 $cm^{-1}$ were attributed to the external symmetric stretching of Si–O–Si bonds as well as the Si–O–Si bending vibration [122,125,126]. The intensities of peaks at 1220 and 1105 $cm^{-1}$ increased with synthesis durations, which was attributed to the formation of Si–O–Si bonds by condensation. Additionally, a peak at 970 $cm^{-1}$ was observed in all spectra, which was linked to the stretching vibration of Si–OH groups [127-129]. Normally, a peak at 1055 $cm^{-1}$ can be observed in the spectrum of CNCs, which links to the β-1,4-glycosidic bonds [130]. However, the Si–O–Si stretching bands of zeolites are in the range of 1100~1000 $cm^{-1}$, which may overlap with the β-1,4-glycosidic bonds, thus the structure changes of CNCs might not be able to observe properly.

(iii) All the spectra showed a broad band centred on 3440 $cm^{-1}$, which was assigned to –OH group asymmetric stretching, indicated the presence of water or hydroxyl functional groups residual in these samples [131]. In addition, a band at 1640 $cm^{-1}$ was attributed to the interlayer stretching and bending vibration modes of molecular water.

(iv) All the spectra showed peaks at 2975, 2940 and 2887 $cm^{-1}$, corresponding to the asymmetric stretching vibrations of $–CH_3$, $–CH_2$ and –CH groups respectively. Bands at 1388 and 1475 $cm^{-1}$ were assigned to the bending vibrations of $–CH_3$ and $–CH_2$, respectively [132,133].

For comparison, IR spectra of the silica gels for Silicalite-1 synthesis without the presence of •OH and CNCs were measured at different crystallisation durations, as presented in Figure S5 (a) and (b). The comparable IR analysis results indicated the main reaction routs for Silicalite-1 synthesis in the presence and absence of •OH and CNCs were identical. However, due to the overlap between Si–O–Si stretching bands of zeolites and the characteristic bands assigned to hydroxyl groups in CNCs, it was challenging to conclude the role of CNCs for Silicalite-1 synthesis in the presence of •OH solely based on the IR analysis.

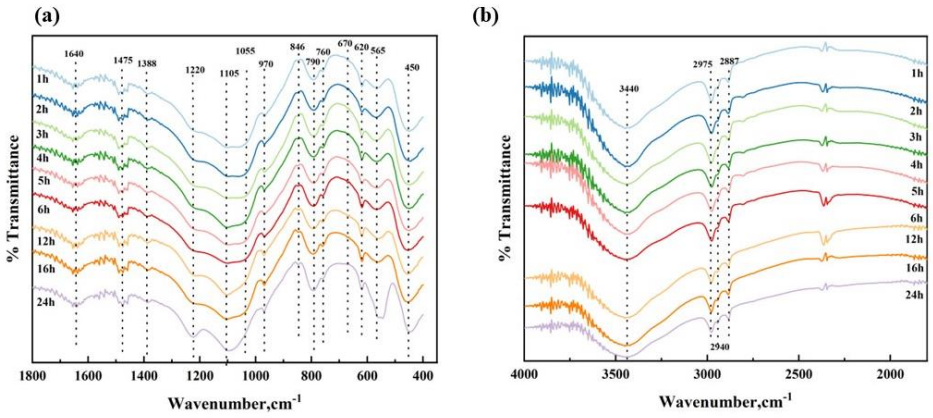


Figure 5.1 FT-IR spectra for synthesised products with different crystallisation time.

To gain a better understanding of the behaviours of CNCs in Silicalite-1 synthesis, TGA analyses were carried out to observe the decomposition of CNCs during synthesis, as presented in Figure 5.2. For comparison, the decompositions of the CNCs (as shown in Figure S6) and the synthesis gel for conventional Silicalite-1 preparation (namely without the addition of •OH and CNCs) were also analysed (as shown in Figure S8). TGA results and the corresponding differential thermogravimetric analyses showed that the decomposition of CNCs occur at temperatures of approximately 200–300℃ and 350-400℃, respectively.

Several mass loss stages were observed for these samples, and the initial mass losses of these samples below 100℃ were due to the evaporation of physically adsorbed water molecules in the samples during heating [125,134]. TGA results for the conventional Silicalite-1 synthesis gel (without the addition of CNCs and •OH) showed the decomposition temperatures approximately 100-200℃ and 550℃, respectively. In the synthesis gel in the presence of •OH and CNCs, there was mass loss observed at between 100 and 350°C, which was attributed to the decomposition of CNCs [125]. It was noticeable that a peak for decomposition at 250°C was observed after crystallisation for 6h and subsequently shifted towards lower temperatures with increased crystallisation durations. After crystallisation for 20h, a new peak was observed at around 100°C, indicating the decomposition of CNCs into smaller molecules. The remarkable mass loss at 550°C was linked to the decomposition of TPAOH.

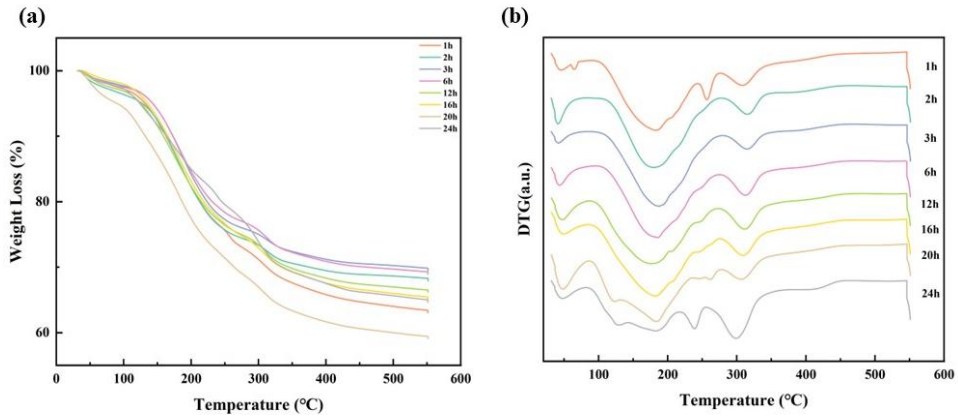


Figure 5.2 (a) TG and (b) DTG curves of Silicalite-1 gels with different crystallisation time.

The synthesised route for Silicalite-1 with the presence of CNCs and •OH is summarized in Figure 5.3 based on the aforementioned results. Some hydroxyl groups of CNCs dissociated under alkaline conditions and formed negatively charged ions, which attracted the $TPA^+$ ions and promoted some Silicalite-1 nucleuses growth near the dissociated CNCs, acting as another type of template for Silicalite-1 synthesis. However, if the CNCs were decomposed into smaller molecules, the efficiency of pore formation was reduced.

The presence of •OH can replace some $OH^-$ to accelerate the cleavage and reformation of Si-O-Si bonds to accelerate the crystallisation [24], and the presence of $OH^-$ in the aluminosilicate gel has been demonstrated to effectively disrupt hydrogen bonds in cellulose.[120] In this study, the •OH was likely not only promoted crystallisation but also facilitated the disruption of hydrogen bonds of CNCs, which produced more nucleation sites. The synergistic effect of CNCs and •OH improved the utilisation of $TPA^+$, promoting Silicalite-1 synthesis when insufficient TPAOH was present.

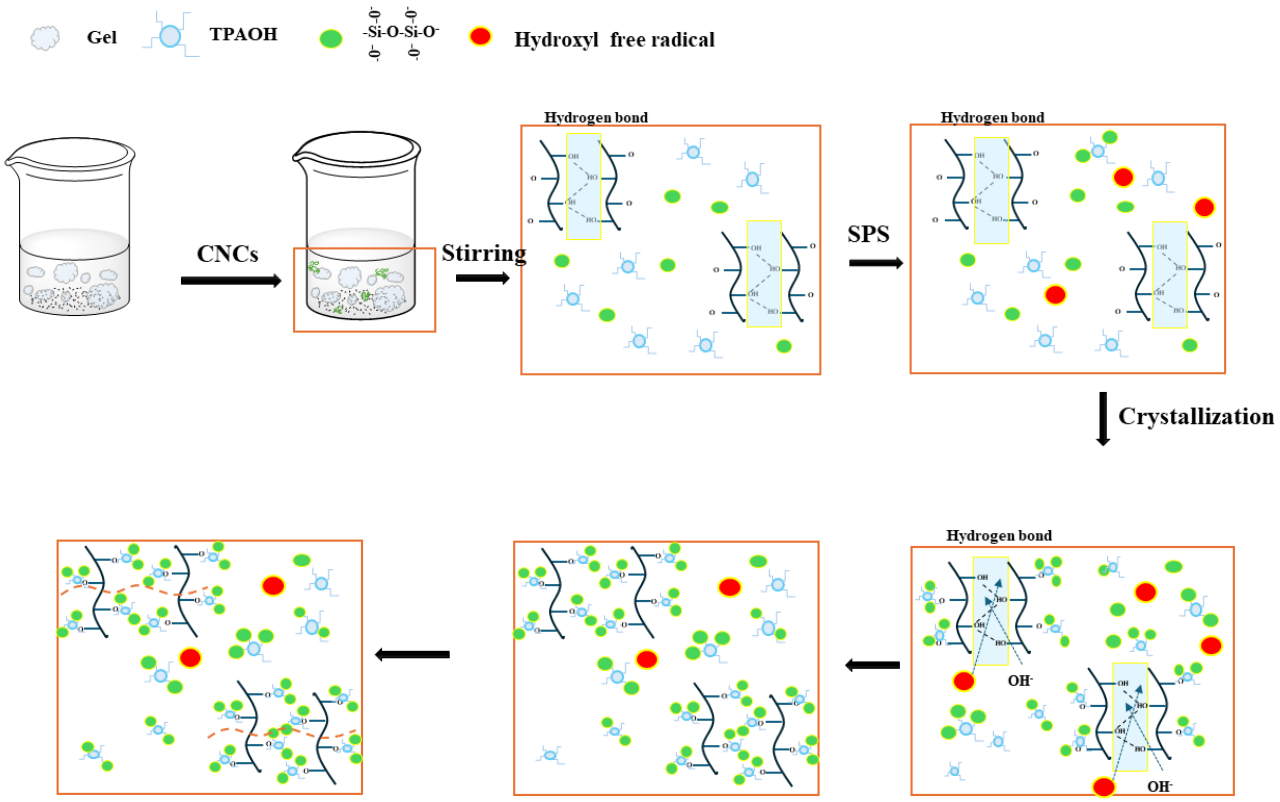


Figure 5.3 Synthesis route for Silicalite-1 with the presence of CNCs and •OH.

# 6. $CO_2$ hydrogenation to $CH_4$ over Ni/Silicalite-1 catalysts

When the TPAOH concentration for zeolites synthesis was minimized to 50%, the presence of 0.02 M SPS and 0.825 wt% CNCs leaded to the highest yield (74%) of silicalite-1 with high relative crystallinity (85%), which demonstrated the successful synthesis of silicalite-1 under mild conditions using •OH and CNCs, which significantly reduced the organic template usage. The prepared silicalite-1 was employed as a catalyst support for Ni/silicalite-1 catalyst (referred as Ni/50%S1-0.02M-0.825) and tested in $CO_2$ hydrogenation for $CH_4$ production, and the catalytic performance was compared with the one synthesised conventionally with 100% TPAOH (referred as Ni/100%S1-0M-0).

## 6.1 Structural and morphological properties

Insignificant difference was observed for Ni/50%S1-0.02M-0.825 and Ni/100%S1-0M-0, as illustrated in Figure 6.1. Characteristic peaks for MFI structure were observed at 8.1°, 8.9°, 23.1°, 24°, and 24.5° and the crystal planes of NiO (111), (200), (220), and (311) were observed at 37.3°, 43.3°, 63.0°, and 75.4° [96]. Figure S8 presented the XRD patterns of the catalysts after reduction in $H_2$. Following reduction, a prominent diffraction peak corresponding to metallic Ni was clearly discernible in the spectra. Notably, peaks observed at 2θ angles of 45˚, 52.3˚, and 77.4˚ confirmed the purity of the nickel nanoparticles [135].

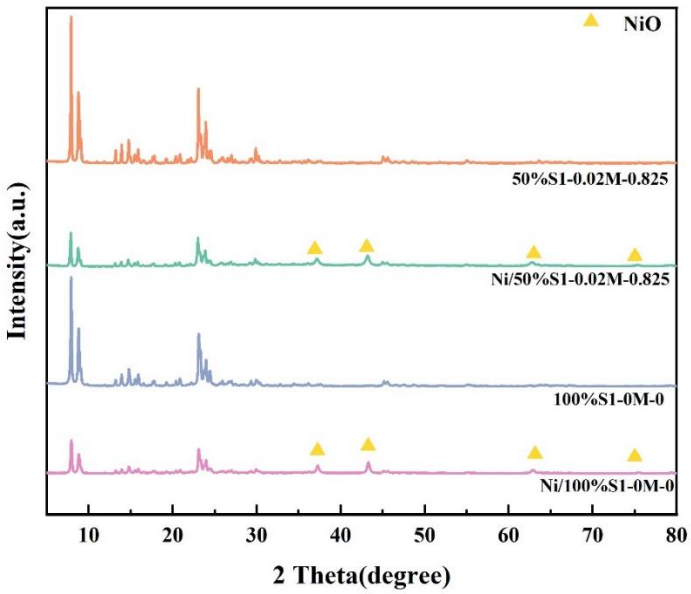


Figure 6.1 XRD patterns of the Silicalite-1 supports and prepared catalysts.

The $N_2$ adsorption-desorption isotherms of Silicalite-1 zeolites before and after Ni loading were presented in Figure 6.2 (a) and (b), and their textural properties are summarized in Table 6.1. The two prepared Ni/silicalite-1 maintained the micropore structures of Silicalite-1 zeolites after impregnation while the specific surface areas were reduced after impregnation, which implied the successful loading of Ni.

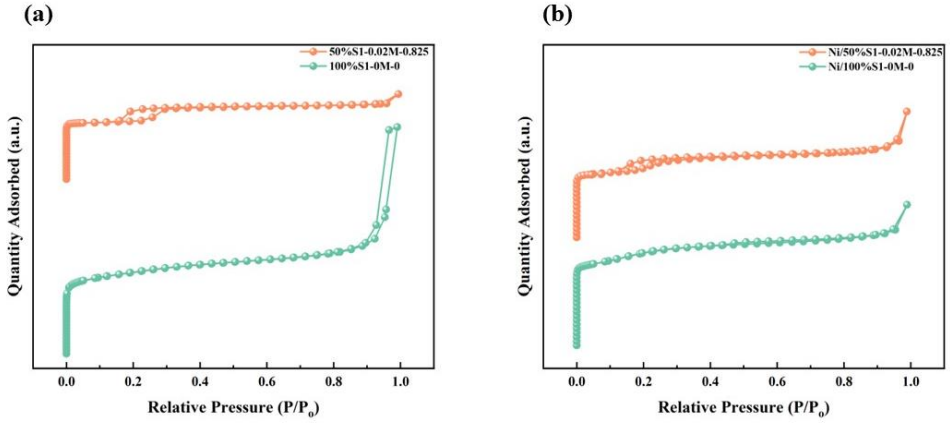


Figure 6.2 $N_2$ adsorption–desorption isotherms of (a) Silicalite-1supports and (b) as-prepared catalysts.

Table 6.1 Textural properties of Silicalite-1 supports and Ni/Silicalite-1 catalysts.

| Sample | Surface Area ($m^2/g$) | |
|---|---|---|
| | $S_{total}$ | $S_{micro}$ |
| 50%S1-0.02M-0.825 | 321 | 141 |
| 100%S1-0M-0 | 401 | 232 |
| Ni/50%S1-0.02M-0.825 | 297 | 88 |
| Ni/100%S1-0M-0 | 345 | 177 |

The Ni loading of the two catalysts was investigated by SEM-EDS and ICP analysis. The SEM-EDS results (presented in Figure S9 and S10) showed that the Ni contents were 12.7 wt% for Ni/50%S1-0.02M-0.825 and 10.36 wt% for Ni/100%S1-0M-0. The ICP results indicated that the Ni content was 13.9 wt% for Ni/0%S1-0.02M-0.825 and 13.70 wt% for Ni/100%S1-0M-0, which was close to the theoretical loading (15.0 wt%).

## 6.2 Catalytic performance

The catalytic performances of Ni/silicalite-1 catalysts were investigated for $CO_2$ methanation at 400°C for 5h, and the $CO_2$ conversion and $CH_4$ selectivity were recorded every hour and presented in Figure 6.3. It was found that the $CO_2$ conversion for both catalysts were comparable (80% for Ni/50%S1-0.02M-0.825 and 82% for Ni/100%S1-0M-0), while the $CH_4$ selectivity for Ni/50%S1-0.02M-0.825 was lower compared to Ni/100%S1-0M-0 (50% *vs.* 65%). The lower $CH_4$ selectivity was ascribed to the lower specific surface area of the silicalite-1 prepared in the presence of •OH and CNCs with 50% TPAOH. Further study was required to optimize the synergy between •OH and CNCs in zeolites synthesis, not only to achieve high yield and crystallinity, but to obtain comparable pore structure compared to conventional synthesised zeolites.

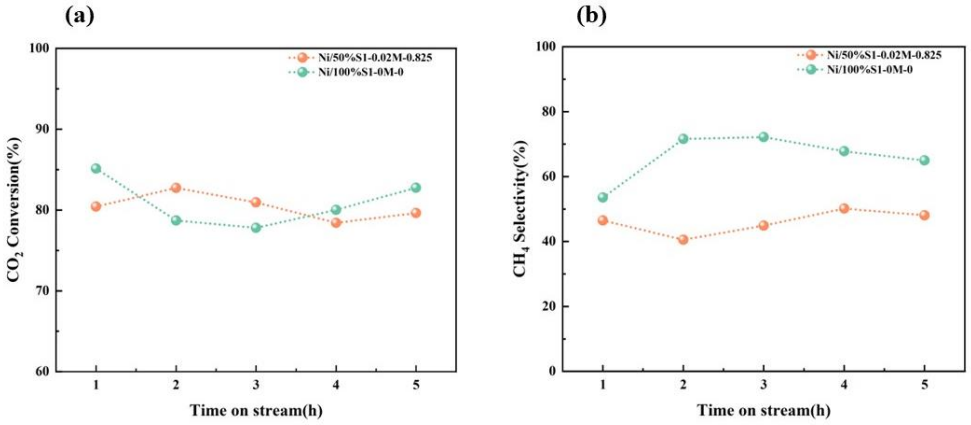


Figure 6.3 Catalytic tests over the catalyst for $CO_2$ conversion and $CH_4$ selectivity.

# 7. Conclusion and future work

The unique advantages of zeolites, such as their uniform pore structure, large specific surface areas, and exceptional hydrothermal stability, have made them extensively utilised in diverse fields including the traditional chemical industry and environmental treatment. However, the synthesis of zeolites typically involves the utilisation of an excessive amount of expensive and corrosive organic alkylammonium ions as templates. In this study, efforts have been made to minimize the usage of TPAOH as the template for Silicalite-1 synthesis by using •OH and CNCs. A series of physicochemical characterisations were conducted to study the yield, crystalline structure, morphology and pore structure of the resulting zeolites, following by testing their performance in $CO_2$ hydrogenation.

Findings can be concluded as follows: (1) The yield of Silicalite-1 was significantly reduced when insufficient TPAOH was present in the synthesis solution; 2) the presence of •OH could increase the yield of Silicalite-1 but the specific surface area of the product was low; 3) the presence of •OH and CNCs could increase the yield of Silicalite-1 with higher specific surface area compared to the •OH alone case. Namely, the synergic effect of •OH and CNCs could promote the synthesis of Silicalite-1 zeolites. The optimal result was obtained when the TPAOH usage was reduced to 50%, with the addition of 0.02 M SPS and 0.825 wt% CNCs, the yield of Silicalite-1 increased to 74% with high relative crystallinity of 85%, being higher than the yield of conventionally synthesised Silicalite-1 with 100% TPAOH usage (the yield was 44% and the relative crystallinity was 72%). Mechanism study demonstrated that the synthesis routes of Silicalite-1 zeolites in the absence and presence of •OH and CNCs were identical, which consisted of the cleavage of Si-O-Si bonds and their re-bonding surrounding the template. However, the decomposition of CNCs to small molecules was observed during the synthesis when •OH and CNCs were present.

Silicalite-1 zeolites synthesised with 50% TPAOH usage and 100% TPAOH usage were used as supports for preparing the Ni/Silicalite-1 catalyst for $CO_2$ methanation. Comparable $CO_2$ conversion (~80%) were observed, whilst the selectivity to $CH_4$ achieved by Ni/50%S1-0.02M-0.825 was lower than that by Ni/100%S1-0M-0 (i.e., 50% *vs.* 65%), which might be due to the lower surface area (297 $m^2/g$ *vs*. 345$m^2/g$).

Although the developed strategy with the synergic effect of •OH and CNCs demonstrated the promising potential for improving zeolites synthesis, further improvements can be done for future development, for example:

(1) Although the presence of •OH and CNCs enhanced the yield of Silicalite-1 with high crystallinity, lower specific surface areas and pore volumes were observed. Therefore, future research should be focused on further optimisation of synthesis conditions, such as aging time and crystallisation temperature.

(2) The synthesis mechanism for Silicalite-1 in the presence of •OH and CNCs is still unclear. In-situ FT-IR and in-situ XRD techniques will be used to gain more clues on the roles of •OH and CNCs in zeolites synthesis.

# References


[1] Thommes, M., Kaneko, K., Neimark, A. V., Olivier, J. P., Rodriguez-Reinoso, F., Rouquerol, J., & Sing, K. S. (2015). Physisorption of gases, with special reference to the evaluation of surface area and pore size distribution (IUPAC Technical Report). *Pure and applied chemistry*, *87*(9-10), 1051-1069.

[2] Xu, R., Pang, W., Yu, J., Huo, Q., & Chen, J. (2009). *Chemistry of zeolites and related porous materials: synthesis and structure*. John Wiley & Sons.

[3] Davis, M. E. (2002). Ordered porous materials for emerging applications. *Nature*, *417*(6891), 813-821.

[4] Liu, X., Song, N., Qian, D., Gu, S., Pu, J., Huang, L., Liu, J., & Qian, K. (2021). Porous inorganic materials for bioanalysis and diagnostic applications. *ACS biomaterials science & engineering*, *8*(10), 4092-4109.

[5] Nova, I., & Tronconi, E. (2014). *Urea-SCR technology for deNOx after treatment of diesel exhausts* (Vol. 5). Springer.

[6] Loewenstein, W. (1954). The distribution of aluminum in the tetrahedra of silicates and aluminates. *American Mineralogist: Journal of Earth and Planetary Materials*, *39*(1-2), 92-96.

[7] Baerlocher, C., McCusker, L. B., & Olson, D. H. (2007). *Atlas of zeolite framework types*. Elsevier.

[8] *Database of Zeolite Structures,http://www.iza-structure.org/databases/ (accessed February 2024)*.

[9] Askari, S., Miar Alipour, S., Halladj, R., & Davood Abadi Farahani, M. H. (2013). Effects of ultrasound on the synthesis of zeolites: a review. *Journal of Porous Materials*, *20*, 285-302.

[10] Zhang, K., & Ostraat, M. L. (2016). Innovations in hierarchical zeolite synthesis. *Catalysis Today*, *264*, 3-15.

[11] Bai, R., Song, Y., Li, Y., & Yu, J. (2019). Creating hierarchical pores in zeolite catalysts. *Trends in Chemistry*, *1*(6), 601-611.

[12] Vogt, E. T., & Weckhuysen, B. M. (2015). Fluid catalytic cracking: recent developments on the grand old lady of zeolite catalysis. *Chemical Society Reviews*, *44*(20), 7342-7370.

[13] Bai, P., Etim, U. J., Yan, Z., Mintova, S., Zhang, Z., Zhong, Z., & Gao, X. (2018). Fluid catalytic cracking technology: current status and recent discoveries on catalyst contamination. *Catalysis Reviews*.

[14] Pacheco, J. J., & Davis, M. E. (2014). Synthesis of terephthalic acid via Diels-Alder reactions with ethylene and oxidized variants of 5-hydroxymethylfurfural. *Proceedings of the National Academy of Sciences*, *111*(23), 8363-8367.

[15] Xu, H., & Wu, P. (2022). New progress in zeolite synthesis and catalysis. *Natl Sci Rev*, *9*(9), nwac045.

[16] Wang, N., Sun, Q., Bai, R., Li, X., Guo, G., & Yu, J. (2016). In situ confinement of ultrasmall Pd clusters within nanosized silicalite-1 zeolite for highly efficient catalysis of hydrogen generation. *Journal of the American Chemical Society*, *138*(24), 7484-7487.

[17] Li, Y., Li, L., & Yu, J. (2017). Applications of zeolites in sustainable chemistry. *Chem*, *3*(6), 928-949.

[18] Fu, G., Dib, E., Lang, Q., Zhao, H., Wang, S., Ding, R., Yang, X., & Valtchev, V. (2022). Acidic

medium synthesis of zeolites–an avenue to control the structure-directing power of organic templates. *Dalton Transactions*, *51*(30), 11499-11506.

[19] Lehman, S. E., & Larsen, S. C. (2014). Zeolite and mesoporous silica nanomaterials: greener syntheses, environmental applications and biological toxicity. *Environmental Science: Nano*, *1*(3), 200-213.

[20] Meng, X., & Xiao, F.-S. (2014). Green routes for synthesis of zeolites. *Chemical reviews*, *114*(2), 1521-1543.

[21] Wu, Q., Meng, X., Gao, X., & Xiao, F.-S. (2018). Solvent-free synthesis of zeolites: mechanism and utility. *Accounts of chemical research*, *51*(6), 1396-1403.

[22] Centi, G., & Perathoner, S. (2003). Catalysis and sustainable (green) chemistry. *Catalysis Today*, *77*(4), 287-297.

[23] Cheng, P., Feng, G., Sun, C., Xu, W., Su, J.-H., Yan, W., & Yu, J. (2018). An efficient synthetic route to accelerate zeolite synthesis via radicals. *Inorganic Chemistry Frontiers*, *5*(9), 2106-2110.

[24] Guodong Feng, P. C., 1* Wenfu Yan,1 Mercedes Boronat,2 Xu Li,1 Ji-Hu Su,3 Jianyu Wang,1 Yi Li,1 Avelino Corma,2 Ruren Xu,1 Jihong Yu1†. (2016 ). Accelerated crystallization of zeolites via hydroxyl free radicals. *Science*

[25] Zhang, B., Li, X., Wu, Q., Zhang, C., Yu, Y., Lan, M., Wei, X., Ying, Z., Liu, T., Liang, G., & Zhao, F. (2016). Synthesis of Ni/mesoporous ZSM-5 for direct catalytic conversion of cellulose to hexitols: modulating the pore structure and acidic sites via a nanocrystalline cellulose template. *Green Chemistry*, *18*(11), 3315-3323.

[26] Abdulridha, S., Jiang, J., Xu, S., Zhou, Z., Liang, H., Mao, B., Zhou, Y., Garforth, A. A., Jiao, Y., & Fan, X. (2020). Cellulose nanocrystals (CNCs) as hard templates for preparing mesoporous zeolite Y assemblies with high catalytic activity. *Green Chemistry*, *22*(15), 5115-5122.

[27] Gomes, E. S., Lutzweiler, G., Losch, P., Silva, A. V., Bernardon, C., Parkhomenko, K., Pereira, M. M., & Louis, B. (2017). Strategy to design zeolite catalysts in the presence of biomass. *Microporous and Mesoporous Materials*, *254*, 28-36.

[28] Gomes, E. S., Aranda, D. A. G., Pereira, M. M., & Louis, B. (2018). ZSM-5 synthesis by the assistance of biomass and biomass-derivate compounds. *Microporous and Mesoporous Materials*, *263*, 251-256.

[29] McBain, J. W. (1932). The sorption of gases and vapours by solids. *(No Title)*.

[30] Zhang, Q., Gao, S., & Yu, J. (2022). Metal sites in zeolites: Synthesis, characterization, and catalysis. *Chemical reviews*, *123*(9), 6039-6106.

[31] Derbe, T., Temesgen, S., Bitew, M., & Fedel, M. (2021). A Short Review on Synthesis, Characterization, and Applications of Zeolites. *Advances in Materials Science and Engineering*, *2021*, 1-17.

[32] Chunfeng, W., Jiansheng, L., Xia, S., Lianjun, W., & Xiuyun, S. (2009). Evaluation of zeolites synthesized from fly ash as potential adsorbents for wastewater containing heavy metals. *Journal of environmental sciences*, *21*(1), 127-136.

[33] Johnson, E., & Arshad, S. E. (2014). Hydrothermally synthesized zeolites based on kaolinite: A review. *Applied Clay Science*, *97*, 215-221.

[34] Khaleque, A., Alam, M. M., Hoque, M., Mondal, S., Haider, J. B., Xu, B., Johir, M., Karmakar, A. K., Zhou, J., & Ahmed, M. B. (2020). Zeolite synthesis from low-cost materials and

environmental applications: A review. *Environmental Advances*, *2*, 100019.

[35] Bibby, D., & Dale, M. (1985). Synthesis of silica-sodalite from non-aqueous systems. *Nature*, *317*(6033), 157-158.

[36] Qisheng, H., Shouhua, F., & Ruren, X. (1988). First syntheses of pentasil-type silica zeolites from non-aqueous systems. *Journal of the Chemical Society, Chemical Communications*(22), 1486-1487.

[37] Pan, T., Wu, Z., & Yip, A. C. (2019). Advances in the green synthesis of microporous and hierarchical zeolites: a short review. *Catalysts*, *9*(3), 274.

[38] Reddy, A. V. B., Moniruzzaman, M., Madhavi, V., & Jaafar, J. (2020). Recent improvements in the extraction, cleanup and quantification of bioactive flavonoids. *Studies in natural products chemistry*, *66*, 197-223.

[39] Cooper, E. R., Andrews, C. D., Wheatley, P. S., Webb, P. B., Wormald, P., & Morris, R. E. (2004). Ionic liquids and eutectic mixtures as solvent and template in synthesis of zeolite analogues. *Nature*, *430*(7003), 1012-1016.

[40] Li, Y., & Yang, W. (2008). Microwave synthesis of zeolite membranes: A review. *Journal of Membrane Science*, *316*(1-2), 3-17.

[41] Madhusoodana, C., Das, R., Kameshima, Y., & Okada, K. (2006). Microwave-assisted hydrothermal synthesis of zeolite films on ceramic supports. *Journal of Materials Science*, *41*, 1481-1487.

[42] Le, T., Wang, Q., Pan, B., Ravindra, A., Ju, S., & Peng, J. (2019). Process regulation of microwave intensified synthesis of Y-type zeolite. *Microporous and Mesoporous Materials*, *284*, 476-485.

[43] Xu, X., Yang, W., Liu, J., & Lin, L. (2000). Synthesis of a high-permeance NaA zeolite membrane by microwave heating. *Advanced Materials*, *12*(3), 195-198.

[44] Matsukata, M., Nishiyama, N., & Ueyama, K. (1993). Synthesis of zeolites under vapor atmosphere: Effect of synthetic conditions on zeolite structure. *Microporous Materials*, *1*(3), 219-222.

[45] Xu, W., Dong, J., Li, J., Li, J., & Wu, F. (1990). A novel method for the preparation of zeolite ZSM-5. *Journal of the Chemical Society, Chemical Communications*(10), 755-756.

[46] Ren, L., Wu, Q., Yang, C., Zhu, L., Li, C., Zhang, P., Zhang, H., Meng, X., & Xiao, F.-S. (2012). Solvent-free synthesis of zeolites from solid raw materials. *Journal of the American Chemical Society*, *134*(37), 15173-15176.

[47] Jin, Y., Sun, Q., Qi, G., Yang, C., Xu, J., Chen, F., Meng, X., Deng, F., & Xiao, F. S. (2013). Solvent-free synthesis of silicoaluminophosphate zeolites. *Angewandte Chemie International Edition*, *52*(35), 9172-9175.

[48] Lee, H., Zones, S. I., & Davis, M. E. (2003). A combustion-free methodology for synthesizing zeolites and zeolite-like materials. *Nature*, *425*(6956), 385-388.

[49] Li, X.-Y., Jiang, Y., Liu, X.-Q., Shi, L.-Y., Zhang, D.-Y., & Sun, L.-B. (2017). Direct synthesis of zeolites from a natural clay, attapulgite. *ACS Sustainable Chemistry & Engineering*, *5*(7), 6124-6130.

[50] Missengue, R. N., Losch, P., Musyoka, N. M., Louis, B., Pale, P., & Petrik, L. F. (2018). Conversion of South African coal fly ash into high-purity ZSM-5 zeolite without additional source of silica or alumina and its application as a methanol-to-olefins catalyst. *Catalysts*, *8*(4), 124.

[51] Chen, K., Ng, K. H., Cheng, C. K., Cheng, Y. W., Chong, C. C., Vo, D. N., Witoon, T., & Ismail, M.

H. (2022). Biomass-derived carbon-based and silica-based materials for catalytic and adsorptive applications- An update since 2010. *Chemosphere*, *287*(Pt 2), 132222.

[52] Klemm, D., Heublein, B., Fink, H. P., & Bohn, A. (2005). Cellulose: fascinating biopolymer and sustainable raw material. *Angewandte Chemie International Edition*, *44*(22), 3358-3393.

[53] González-Rivera, J., Galindo-Esquivel, I. R., Onor, M., Bramanti, E., Longo, I., & Ferrari, C. (2014). Heterogeneous catalytic reaction of microcrystalline cellulose in hydrothermal microwave-assisted decomposition: effect of modified zeolite Beta. *Green Chemistry*, *16*(3), 1417-1425.

[54] de Souza Lima, M. M., & Borsali, R. (2004). Rodlike cellulose microcrystals: structure, properties, and applications. *Macromolecular rapid communications*, *25*(7), 771-787.

[55] Acharya, S., Liyanage, S., Parajuli, P., Rumi, S. S., Shamshina, J. L., & Abidi, N. (2021). Utilization of cellulose to its full potential: A review on cellulose dissolution, regeneration, and applications. *Polymers*, *13*(24), 4344.

[56] Tao, H., Li, C., Ren, J., Wang, Y., & Lu, G. (2011). Synthesis of mesoporous zeolite single crystals with cheap porogens. *Journal of Solid State Chemistry*, *184*(7), 1820-1827.

[57] Yu, H., Li, F., He, W., Song, C., Zhang, Y., Li, Z., & Lin, H. (2020). Synthesis of micro–mesoporous ZSM-5 zeolite with microcrystalline cellulose as co-template and catalytic cracking of polyolefin plastics. *RSC Advances*, *10*(37), 22126-22136.

[58] Nie, P., Liu, X., Zhang, P., Yuan, X., Li, X., Lin, S., Yin, Z., & Wang, Z. (2021). Quaternary ammonium cellulose promoted synthesis of hollow nano-sized ZSM-5 zeolite as stable catalyst for benzene alkylation with ethanol. *Journal of Materials Science*, *56*, 8461-8478.

[59] Awala, H., Gilson, J.-P., Retoux, R., Boullay, P., Goupil, J.-M., Valtchev, V., & Mintova, S. (2015). Template-free nanosized faujasite-type zeolites. *Nature materials*, *14*(4), 447-451.

[60] Xie, B., Song, J., Ren, L., Ji, Y., Li, J., & Xiao, F.-S. (2008). Organotemplate-free and fast route for synthesizing beta zeolite. *Chemistry of materials*, *20*(14), 4533-4535.

[61] Liu, Y., Wang, X., Li, J., Zhang, Q., Niu, Z., Wang, S., Gao, Y., Gao, M., Bai, R., & Zhou, Y. (2023). Constructing Intrapenetrated Hierarchical Zeolites with Highly Complete Framework via Protozeolite Seeding. *Angewandte Chemie*, e202312131.

[62] Gligorovski, S., Strekowski, R., Barbati, S., & Vione, D. (2015). Environmental implications of hydroxyl radicals (• OH). *Chemical reviews*, *115*(24), 13051-13092.

[63] Gogate, P. R. (2008). Treatment of wastewater streams containing phenolic compounds using hybrid techniques based on cavitation: A review of the current status and the way forward. *Ultrasonics Sonochemistry*, *15*(1), 1-15.

[64] Ma, H., Wang, M., Yang, R., Wang, W., Zhao, J., Shen, Z., & Yao, S. (2007). Radiation degradation of Congo Red in aqueous solution. *Chemosphere*, *68*(6), 1098-1104.

[65] Ikehata, K., Jodeiri Naghashkar, N., & Gamal El-Din, M. (2006). Degradation of aqueous pharmaceuticals by ozonation and advanced oxidation processes: a review. *Ozone: Science and Engineering*, *28*(6), 353-414.

[66] Shankar, M., Nélieu, S., Kerhoas, L., & Einhorn, J. (2008). Natural sunlight NO3-/NO2--induced photo-degradation of phenylurea herbicides in water. *Chemosphere*, *71*(8), 1461-1468.

[67] Brillas, E., Sirés, I., & Oturan, M. A. (2009). Electro-Fenton process and related electrochemical technologies based on Fenton's reaction chemistry. *Chemical reviews*, *109*(12), 6570-6631.

[68] Pennington, D. E., & Haim, A. (1968). Stoichiometry and mechanism of the chromium (II)-peroxydisulfate reaction. *Journal of the American Chemical Society*, *90*(14), 3700-3704.

[69] Chen, X., Qiu, M., Li, S., Yang, C., Shi, L., Zhou, S., Yu, G., Ge, L., Yu, X., Liu, Z., Sun, N., Zhang, K., Wang, H., Wang, M., Zhong, L., & Sun, Y. (2020). Gamma-Ray Irradiation to Accelerate Crystallization of Mesoporous Zeolites. *Angew Chem Int Ed Engl*, *59*(28), 11325-11329.

[70] Cheng, P., Song, M., Zhang, H., Xuan, Y., & Wu, C. (2019). Accelerated synthesis of zeolites via radicalized seeds. *Journal of Materials Science*, *54*(6), 4573-4578.

[71] Han, Z., Zhang, F., & Zhao, X. (2019). Green energy-efficient synthesis of Fe-ZSM-5 zeolite and its application for hydroxylation of phenol. *Microporous and Mesoporous Materials*, *290*, 109679.

[72] Wang, J., Liu, P., Boronat, M., Ferri, P., Xu, Z., Liu, P., Shen, B., Wang, Z., & Yu, J. (2020). Organic-Free Synthesis of Zeolite Y with High Si/Al Ratios: Combined Strategy of In Situ Hydroxyl Radical Assistance and Post-Synthesis Treatment. *Angew Chem Int Ed Engl*, *59*(39), 17225-17228.

[73] Khalil, M. T., Wu, X., Liu, S., Liu, Y., Ashraf, S., Shen, R., Zhou, L., Yuan, H., Jiang, J., & Li, B. Catalytic CO2 Conversion to Methanol: Opportunities and Challenges. *Available at SSRN 4681512*.

[74] Jiang, X., Nie, X., Guo, X., Song, C., & Chen, J. G. (2020). Recent advances in carbon dioxide hydrogenation to methanol via heterogeneous catalysis. *Chemical reviews*, *120*(15), 7984-8034.

[75] Ra, E. C., Kim, K. Y., Kim, E. H., Lee, H., An, K., & Lee, J. S. (2020). Recycling carbon dioxide through catalytic hydrogenation: recent key developments and perspectives. *ACS Catalysis*, *10*(19), 11318-11345.

[76] Graça, I., González, L., Bacariza, M., Fernandes, A., Henriques, C., Lopes, J., & Ribeiro, M. (2014). CO2 hydrogenation into CH4 on NiHNaUSY zeolites. *Applied Catalysis B: Environmental*, *147*, 101-110.

[77] Ye, R.-P., Ding, J., Gong, W., Argyle, M. D., Zhong, Q., Wang, Y., Russell, C. K., Xu, Z., Russell, A. G., & Li, Q. (2019). CO2 hydrogenation to high-value products via heterogeneous catalysis. *Nature communications*, *10*(1), 5698.

[78] Bonura, G., Frusteri, F., Cannilla, C., Ferrante, G. D., Aloise, A., Catizzone, E., Migliori, M., & Giordano, G. (2016). Catalytic features of CuZnZr–zeolite hybrid systems for the direct CO2-to-DME hydrogenation reaction. *Catalysis Today*, *277*, 48-54.

[79] Bansode, A., & Urakawa, A. (2014). Towards full one-pass conversion of carbon dioxide to methanol and methanol-derived products. *Journal of Catalysis*, *309*, 66-70.

[80] Singh, R., Tripathi, K., Pant, K. K., & Parikh, J. K. (2022). Unravelling synergetic interaction over tandem Cu-ZnO-ZrO2/hierarchical ZSM5 catalyst for CO2 hydrogenation to methanol and DME. *Fuel*, *318*, 123641.

[81] Gao, P., Li, S., Bu, X., Dang, S., Liu, Z., Wang, H., Zhong, L., Qiu, M., Yang, C., & Cai, J. (2017). Direct conversion of CO2 into liquid fuels with high selectivity over a bifunctional catalyst. *Nature chemistry*, *9*(10), 1019-1024.

[82] Ni, Y., Chen, Z., Fu, Y., Liu, Y., Zhu, W., & Liu, Z. (2018). Selective conversion of CO2 and H2 into aromatics. *Nature communications*, *9*(1), 3457.

[83] Azhari, N. J., Nurdini, N., Mardiana, S., Ilmi, T., Fajar, A. T., Makertihartha, I., & Kadja, G. T. (2022). Zeolite-based catalyst for direct conversion of CO2 to C2+ hydrocarbon: A review. *Journal of CO2 Utilization*, *59*, 101969.

[84] Izadbakhsh, A., Farhadi, F., Khorasheh, F., Sahebdelfar, S., Asadi, M., & Feng, Y. Z. (2009). Effect

of SAPO-34's composition on its physico-chemical properties and deactivation in MTO process. *Applied Catalysis A: General*, *364*(1-2), 48-56.

[85] Tong, M., Chizema, L. G., Chang, X., Hondo, E., Dai, L., Zeng, Y., Zeng, C., Ahmad, H., Yang, R., & Lu, P. (2021). Tandem catalysis over tailored ZnO-ZrO2/MnSAPO-34 composite catalyst for enhanced light olefins selectivity in CO2 hydrogenation. *Microporous and Mesoporous Materials*, *320*, 111105.

[86] Wei, J., Yao, R., Ge, Q., Xu, D., Fang, C., Zhang, J., Xu, H., & Sun, J. (2021). Precisely regulating Brønsted acid sites to promote the synthesis of light aromatics via CO2 hydrogenation. *Applied Catalysis B: Environmental*, *283*, 119648.

[87] Tian, P., Zhan, G., Tian, J., Tan, K. B., Guo, M., Han, Y., Fu, T., Huang, J., & Li, Q. (2022). Direct CO2 hydrogenation to light olefins over ZnZrOx mixed with hierarchically hollow SAPO-34 with rice husk as green silicon source and template. *Applied Catalysis B: Environmental*, *315*, 121572.

[88] Yan, P., Peng, H., Vogrin, J., Rabiee, H., & Zhu, Z. (2023). Selective CO2 Hydrogenation over Zeolite-Based Catalysts for Targeted High Value Product. *Journal of Materials Chemistry A*.

[89] Fan, W. K., & Tahir, M. (2021). Recent trends in developments of active metals and heterogenous materials for catalytic CO2 hydrogenation to renewable methane: A review. *Journal of Environmental Chemical Engineering*, *9*(4), 105460.

[90] Jangam, A., Das, S., Dewangan, N., Hongmanorom, P., Hui, W. M., & Kawi, S. (2020). Conversion of CO2 to C1 chemicals: catalyst design, kinetics and mechanism aspects of the reactions. *Catalysis Today*, *358*, 3-29.

[91] Fischer, F., Tropsch, H., & Dilthey, P. (1925). Reduction of carbon monoxide to methane in the presence of various metals. *Brennst. Chem*, *6*, 265-271.

[92] Vannice, M. (1976). The catalytic synthesis of hydrocarbons from carbon monoxide and hydrogen. *Catalysis Reviews—Science and Engineering*, *14*(1), 153-191.

[93] Mills, G. A., & Steffgen, F. W. (1974). Catalytic methanation. *Catalysis Reviews*, *8*(1), 159-210.

[94] Bacariza, M. C., Graça, I., Lopes, J. M., & Henriques, C. (2019). Tuning zeolite properties towards CO2 methanation: An overview. *ChemCatChem*, *11*(10), 2388-2400.

[95] Lan, L., Wang, A., & Wang, Y. (2019). CO2 hydrogenation to lower hydrocarbons over ZSM-5-supported catalysts in a dielectric-barrier discharge plasma reactor. *Catalysis Communications*, *130*, 105761.

[96] Cui, Y., Chen, B., Xu, L., Chen, M., Wu, C.-e., Qiu, J., Cheng, G., Wang, N., Xu, J., & Hu, X. (2023). CO2 methanation over the Ni-based catalysts supported on the hollow ZSM-5 zeolites: Effects of the hollow structure and alkaline treatment. *Fuel*, *334*, 126783.

[97] da Costa-Serra, J. F., Cerdá-Moreno, C., & Chica, A. (2020). Zeolite-supported Ni catalysts for CO2 methanation: effect of zeolite structure and Si/Al ratio. *Applied Sciences*, *10*(15), 5131.

[98] Guo, X., Traitangwong, A., Hu, M., Zuo, C., Meeyoo, V., Peng, Z., & Li, C. (2018). Carbon dioxide methanation over nickel-based catalysts supported on various mesoporous material. *Energy & fuels*, *32*(3), 3681-3689.

[99] Scirè, S., Crisafulli, C., Maggiore, R., Minicò, S., & Galvagno, S. (1998). Influence of the support on CO 2 methanation over Ru catalysts: an FT-IR study. *Catalysis Letters*, *51*, 41-45.

[100] Delmelle, R., Duarte, R. B., Franken, T., Burnat, D., Holzer, L., Borgschulte, A., & Heel, A. (2016). Development of improved nickel catalysts for sorption enhanced CO2 methanation.

*international journal of hydrogen energy*, *41*(44), 20185-20191.

[101] Borgschulte, A., Gallandat, N., Probst, B., Suter, R., Callini, E., Ferri, D., Arroyo, Y., Erni, R., Geerlings, H., & Züttel, A. (2013). Sorption enhanced CO 2 methanation. *Physical Chemistry Chemical Physics*, *15*(24), 9620-9625.

[102] Walspurger, S., Elzinga, G. D., Dijkstra, J. W., Sarić, M., & Haije, W. G. (2014). Sorption enhanced methanation for substitute natural gas production: Experimental results and thermodynamic considerations. *Chemical Engineering Journal*, *242*, 379-386.

[103] da Silva, D. C., Letichevsky, S., Borges, L. E., & Appel, L. G. (2012). The Ni/ZrO2 catalyst and the methanation of CO and CO2. *international journal of hydrogen energy*, *37*(11), 8923-8928.

[104] Tada, S., Shimizu, T., Kameyama, H., Haneda, T., & Kikuchi, R. (2012). Ni/CeO2 catalysts with high CO2 methanation activity and high CH4 selectivity at low temperatures. *international journal of hydrogen energy*, *37*(7), 5527-5531.

[105] Ashok, J., Ang, M., & Kawi, S. (2017). Enhanced activity of CO2 methanation over Ni/CeO2-ZrO2 catalysts: Influence of preparation methods. *Catalysis Today*, *281*, 304-311.

[106] Danaci, S., Protasova, L., Lefevere, J., Bedel, L., Guilet, R., & Marty, P. (2016). Efficient CO2 methanation over Ni/Al2O3 coated structured catalysts. *Catalysis Today*, *273*, 234-243.

[107] Lim, J. Y., McGregor, J., Sederman, A., & Dennis, J. (2016). Kinetic studies of CO2 methanation over a Ni/γ-Al2O3 catalyst using a batch reactor. *Chemical Engineering Science*, *141*, 28-45.

[108] Lin, J., Ma, C., Wang, Q., Xu, Y., Ma, G., Wang, J., Wang, H., Dong, C., Zhang, C., & Ding, M. (2019). Enhanced low-temperature performance of CO2 methanation over mesoporous Ni/Al2O3-ZrO2 catalysts. *Applied Catalysis B: Environmental*, *243*, 262-272.

[109] Park, J.-N., & McFarland, E. W. (2009). A highly dispersed Pd–Mg/SiO2 catalyst active for methanation of CO2. *Journal of Catalysis*, *266*(1), 92-97.

[110] Sholeha, N. A., Jannah, L., Rohma, H. N., Widiastuti, N., Prasetyoko, D., Jalil, A. A., & Bahruji, H. (2020). Synthesis of zeolite NaY from dealuminated metakaolin as Ni support for CO2 hydrogenation to methane. *Clays and Clay Minerals*, *68*(5), 513-523.

[111] Westermann, A., Azambre, B., Bacariza, M., Graça, I., Ribeiro, M., Lopes, J., & Henriques, C. (2015). Insight into CO2 methanation mechanism over NiUSY zeolites: An operando IR study. *Applied Catalysis B: Environmental*, *174*, 120-125.

[112] Wang, X., Zhu, L., Liu, Y., & Wang, S. (2018). CO2 methanation on the catalyst of Ni/MCM-41 promoted with CeO2. *Science of the total environment*, *625*, 686-695.

[113] Duan, D., Zhang, Y., Li, J., Huang, L., Xu, Z., Zhang, Y., Sun, W., Wang, Q., & Ruan, R. (2023). Synthesis of nanocrystalline cellulose induced hierarchical porous ZSM-5 for catalytic conversion of low-density polyethylene. *Fuel*, *331*, 125757.

[114] Khatamian, M., & Irani, M. (2009). Preparation and characterization of nanosized ZSM-5 zeolite using kaolin and investigation of kaolin content, crystallization time and temperature changes on the size and crystallinity of products. *Journal of the Iranian Chemical Society*, *6*, 187-194.

[115] Zhou, Q., Dong, P., Liu, L., & Cheng, B. (2005). Study on the sedimentation self-assembly of colloidal SiO2 particles under gravitational field. *Colloids and Surfaces A: Physicochemical and Engineering Aspects*, *253*(1-3), 169-174.

[116] Dose, M. E., Zhang, K., Thompson, J. A., Leisen, J., Chance, R. R., Koros, W. J., McCool, B. A.,

& Lively, R. P. (2014). Effect of crystal size on framework defects and water uptake in fluoride mediated silicalite-1. *Chemistry of materials*, *26*(15), 4368-4376.

[117] Groen, J. C., & Pérez-Ramírez, J. (2004). Critical appraisal of mesopore characterization by adsorption analysis. *Applied Catalysis A: General*, *268*(1-2), 121-125.

[118] Li, W.-C., Lu, A.-H., Palkovits, R., Schmidt, W., Spliethoff, B., & Schüth, F. (2005). Hierarchically structured monolithic silicalite-1 consisting of crystallized nanoparticles and its performance in the Beckmann rearrangement of cyclohexanone oxime. *Journal of the American Chemical Society*, *127*(36), 12595-12600.

[119] Hoang, P. H., & Dat, N. M. (2021). Study on using cellulose derivatives as pore directing agent for preparation of hierarchical ZSM-5 zeolite catalyst. *Advanced Powder Technology*, *32*(10), 3927-3933.

[120] Valtchev, V., Mintova, S., Vulchev, I., & Lazarova, V. (1994). Influence of reactive radicals in cellulose fibres on the formation of zeolite coatings. *Journal of the Chemical Society, Chemical Communications*(18), 2087-2088.

[121] Tingaut, P., Zimmermann, T., & Sèbe, G. (2012). Cellulose nanocrystals and microfibrillated cellulose as building blocks for the design of hierarchical functional materials. *Journal of Materials Chemistry*, *22*(38), 20105-20111.

[122] Yeong, Y. F., Abdullah, A. Z., Ahmad, A. L., & Bhatia, S. (2009). Synthesis, structure and acid characteristics of partially crystalline silicalite-1 based materials. *Microporous and Mesoporous Materials*, *123*(1-3), 129-139.

[123] Wang, Y., Tang, Y., Dong, A., Wang, X., Ren, N., & Gao, Z. (2002). Zeolitization of diatomite to prepare hierarchical porous zeolite materials through a vapor-phase transport process. *Journal of Materials Chemistry*, *12*(6), 1812-1818.

[124] Kirschhock, C. E., Ravishankar, R., Verspeurt, F., Grobet, P. J., Jacobs, P. A., & Martens, J. A. (1999). Identification of Precursor Species in the Formation of MFI Zeolite in the TPAOH— TEOS— H2O System. *The Journal of Physical Chemistry B*, *103*(24), 4965-4971.

[125] Sabarish, R., & Unnikrishnan, G. (2017). Synthesis, characterization and catalytic activity of hierarchical ZSM-5 templated by carboxymethyl cellulose. *Powder technology*, *320*, 412-419.

[126] Zhang, X., Wu, Y., He, S., & Yang, D. (2007). Structural characterization of sol–gel composites using TEOS/MEMO as precursors. *Surface and Coatings Technology*, *201*(12), 6051-6058.

[127] Hongmanorom, P., Ashok, J., Zhang, G., Bian, Z., Wai, M. H., Zeng, Y., Xi, S., Borgna, A., & Kawi, S. (2021). Enhanced performance and selectivity of CO2 methanation over phyllosilicate structure derived Ni-Mg/SBA-15 catalysts. *Applied Catalysis B: Environmental*, *282*, 119564.

[128] De, G., Karmakar, B., & Ganguli, D. (2000). Hydrolysis–condensation reactions of TEOS in the presence of acetic acid leading to the generation of glass-like silica microspheres in solution at room temperature. *Journal of Materials Chemistry*, *10*(10), 2289-2293.

[129] Hedlund, J., Noack, M., Kölsch, P., Creaser, D., Caro, J., & Sterte, J. (1999). ZSM-5 membranes synthesized without organic templates using a seeding technique. *Journal of Membrane Science*, *159*(1-2), 263-273.

[130] Wu, Y., Wang, L., Qing, Y., Yan, N., Tian, C., & Huang, Y. (2017). A green route to prepare fluorescent and absorbent nano-hybrid hydrogel for water detection. *Scientific reports*, *7*(1), 4380.

[131] Olejniczak, Z., Łęczka, M., Cholewa-Kowalska, K., Wojtach, K., Rokita, M., & Mozgawa, W. (2005). 29Si MAS NMR and FTIR study of inorganic–organic hybrid gels. *Journal of Molecular Structure*, *744*, 465-471.

[132] Sanaeepur, H., Kargari, A., & Nasernejad, B. (2014). Aminosilane-functionalization of a nanoporous Y-type zeolite for application in a cellulose acetate based mixed matrix membrane for CO 2 separation. *RSC Advances*, *4*(109), 63966-63976.

[133] Fu, E., Zhang, S., Luan, Y., Zhang, Y., Saghir, S., & Xiao, Z. (2022). Novel superabsorbent polymer composites based on α-cellulose and modified zeolite: Synthesis, characterization, water absorbency and water retention capacity. *Cellulose*, *29*(3), 1727-1737.

[134] Etminani-Isfahani, N., Mohammadbagheri, Z., & Rahmati, A. (2020). 4-(6-Aminohexyl) amino-4-oxo-2-butenoic acid as a novel hydrophilic monomer for synthesis of cellulose-based superabsorbents with high water absorption capacity. *Carbohydrate polymers*, *250*, 116959.

[135] Taghizadeh, F. (2016). The study of structural and magnetic properties of NiO nanoparticles. *Optics and Photonics Journal*, *6*(8), 164-169.

# Appendix

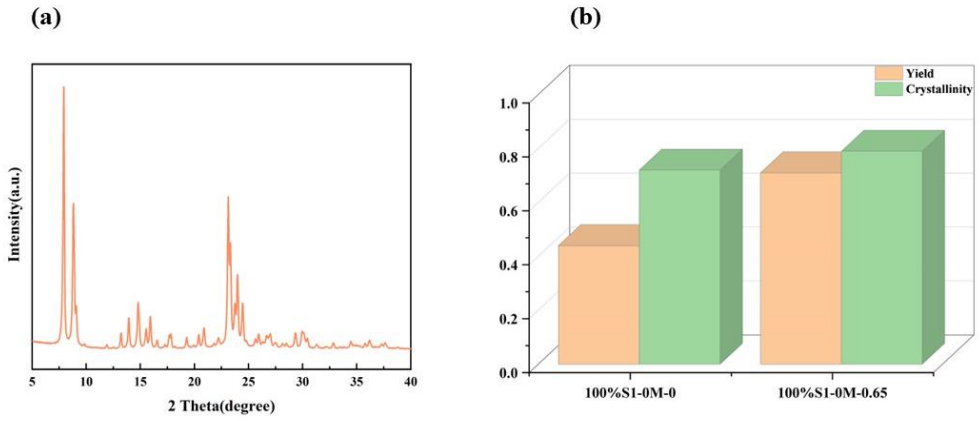


Figure S1(a) XRD patterns and (b) yields and crystallinities of the solid products synthesised when 100% TPAOH was present (The errors of the yields and crystallinities were 5.6% and 3.5%).

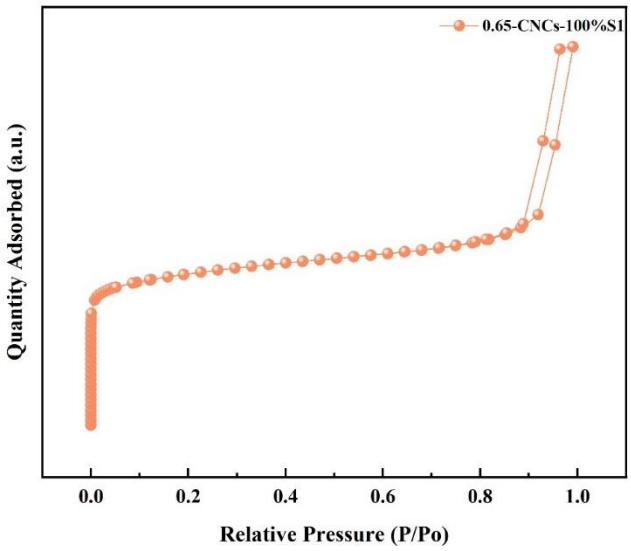


Figure S2 $N_2$ adsorption-desorption isotherms of the solid products synthesised with CNCs when 100% TPAOH was present.

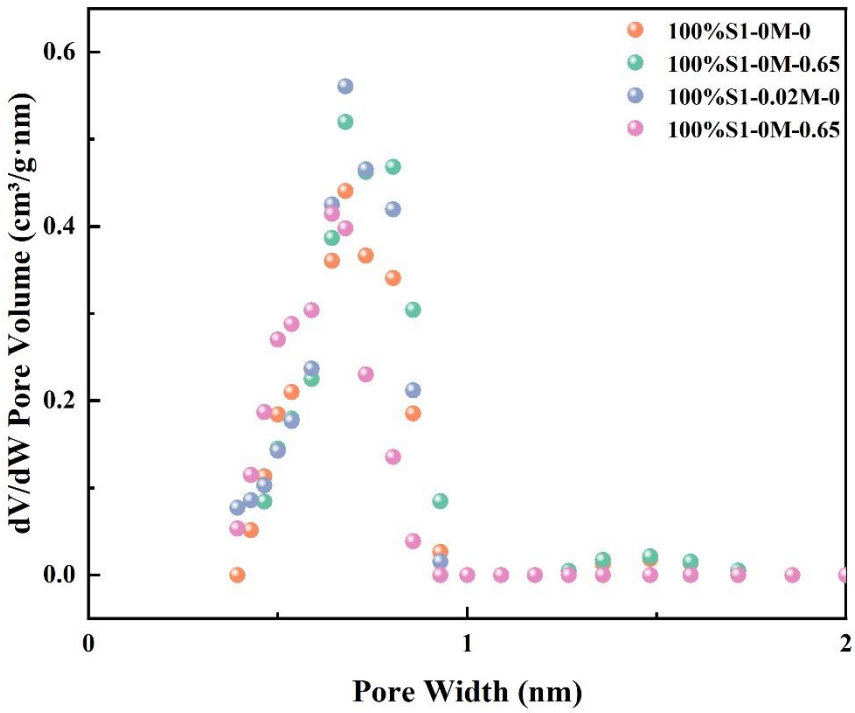


Figure S3 Micropore size distributions of the solid products when 100% TPAOH present.

Figure S4 The gels at the bottom of reactor after crystallisation (Two samples were synthesised in the presence of 0.02M SPS, and the sample above the dashed line utilized 1.3wt% CNCs, whereas the sample below the dashed line utilized 1wt% CNCs).

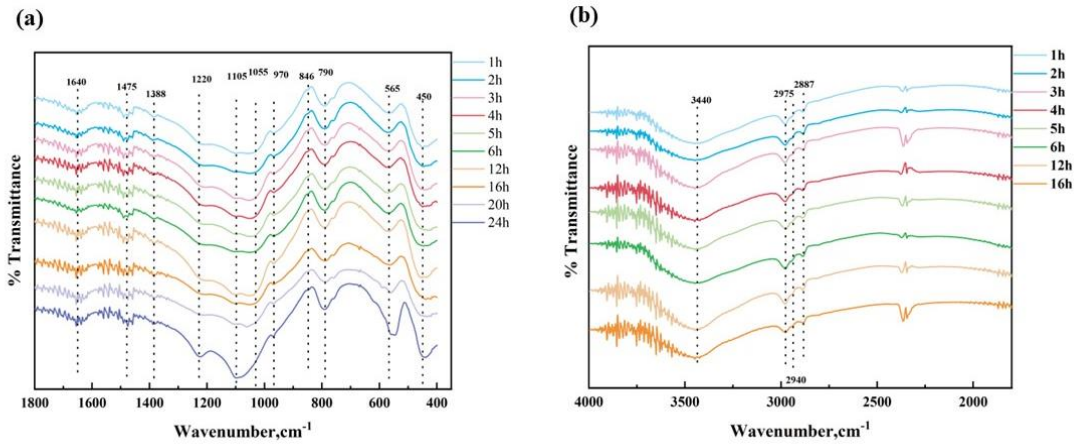


Figure S5 FT-IR spectrum for 50%S1-0M-0 with different crystallisation time.

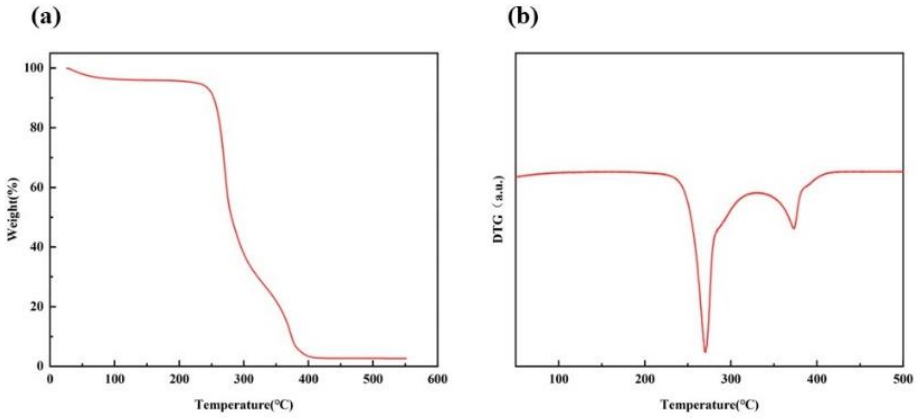


Figure S6 (a) TG and (b) DTG curve of CNCs.

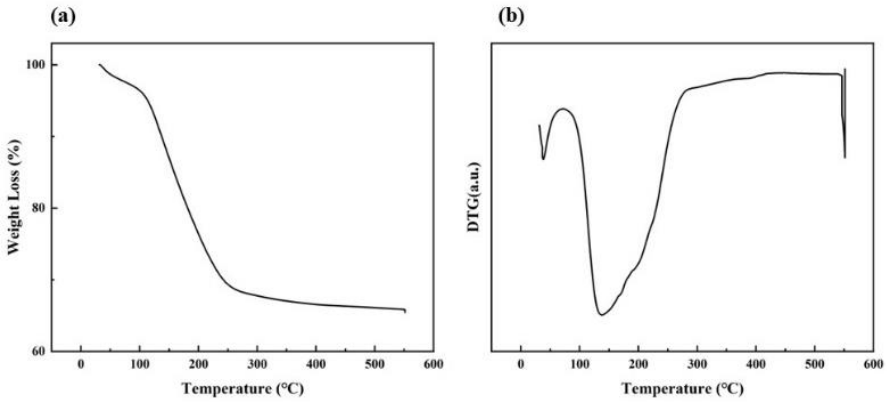


Figure S7 (a) TG and (b) DTG curve of 50%S1-0M-0.

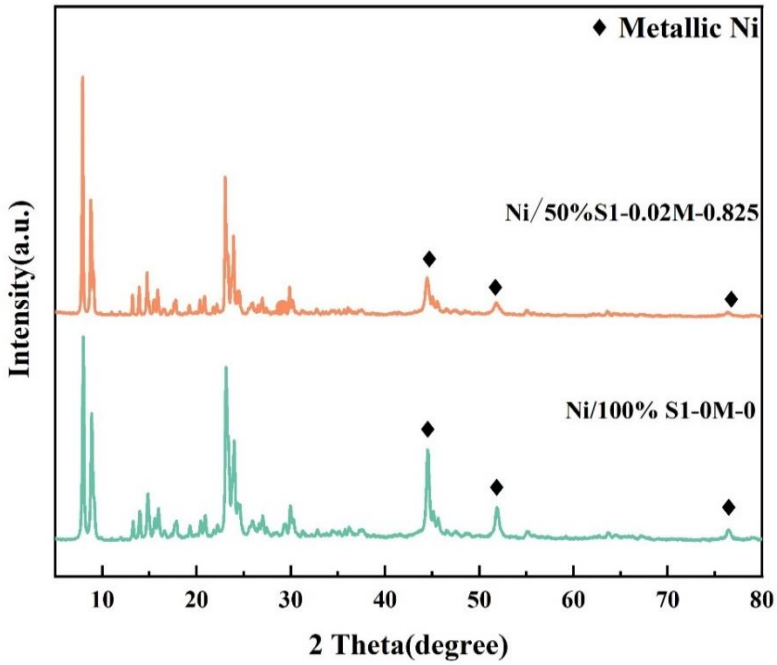


Figure S8 XRD patterns of Ni/Silicalite-1 catalysts after reaction at 400℃.

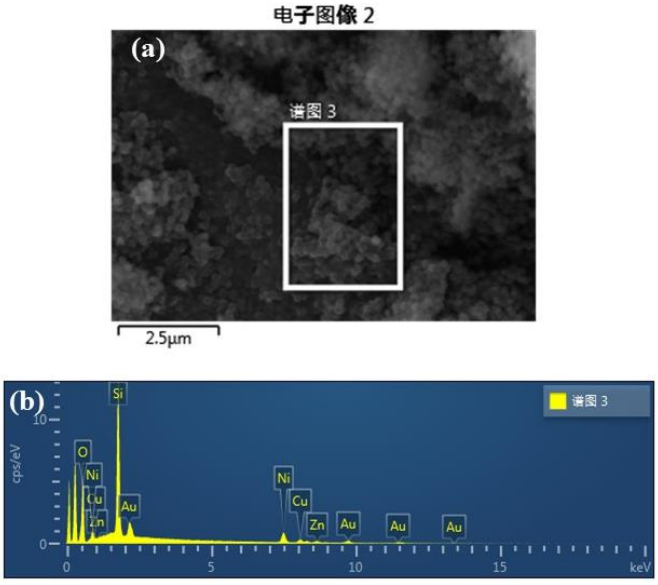


Figure S10 (a) SEM image and (b)elemental mapping of Ni/50%S1-0.02M-0.825.

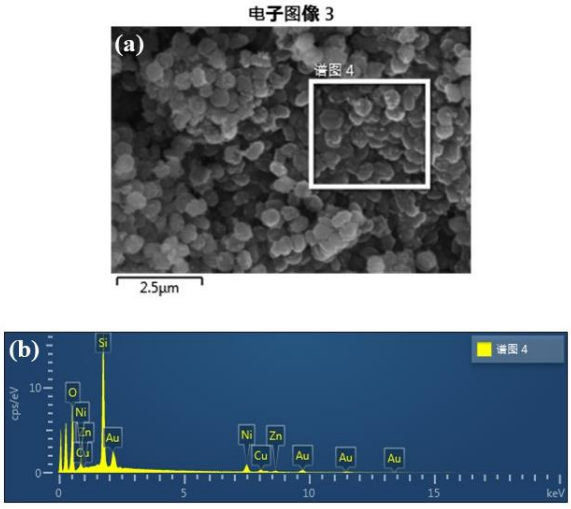


Figure S11 (a) SEM image and (b)elemental mapping of Ni/100%S1-0M-0.

Table S1 Textural properties of Silicalite-1 synthesised when 100% TPAOH was present.

| Sample | Surface Area ($m^2/g$) | | Pore Volume ($cm^3/g$) | |
|---|---|---|---|---|
| | $S_{total}$ | $S_{micro}$ | $V_{total}$ | $V_{micro}$ |
| 100%S1 | 401 | 232 | 0.54 | 0.12 |
| 100% S1-0.02 | 422 | 249 | 0.53 | 0.14 |
| 0.65-CNCs-100%S1 | 456 | 303 | 0.57 | 0.17 |
| 0.65-CNCs-100%S1-0.02 | 303 | 200 | 0.36 | 0.10 |

Table S2 The yield of solid products. (- means no solid products but all gel in the reactor)

| sample | Yield |
|---|---|
| 50%S1-0.03 | 0.48 |
| 0.33-CNCs-50%S1-0.03 | 0.0059 |
| 0.65-CNCs-50%S1-0.03 | - |
| 0.825-CNCs-50%S1-0.03 | - |
| 1-CNCs-50%S1-0.03 | - |
| 1.15-CNCs-50%S1-0.03 | - |
| 1.3-CNCs-50%S1-0.03 | - |